

OPTICAL SPECTROSCOPY OF INDIVIDUAL  
SINGLE-WALLED CARBON NANOTUBES  
IN AN ELECTRIC GATE STRUCTURE:  
TUNING THE PHOTOLUMINESCENCE  
WITH ELECTRIC FIELDS

Dissertation der Fakultät für Physik  
der Ludwig-Maximilians-Universität München



vorgelegt von

**Jan Tibor Glückert**

München, Januar 2014

**Erstgutachter:** Prof. Alexander Högele

**Zweitgutachter:** Prof. Achim Hartschuh

**Datum der Verteidigung:** 27. Januar 2014

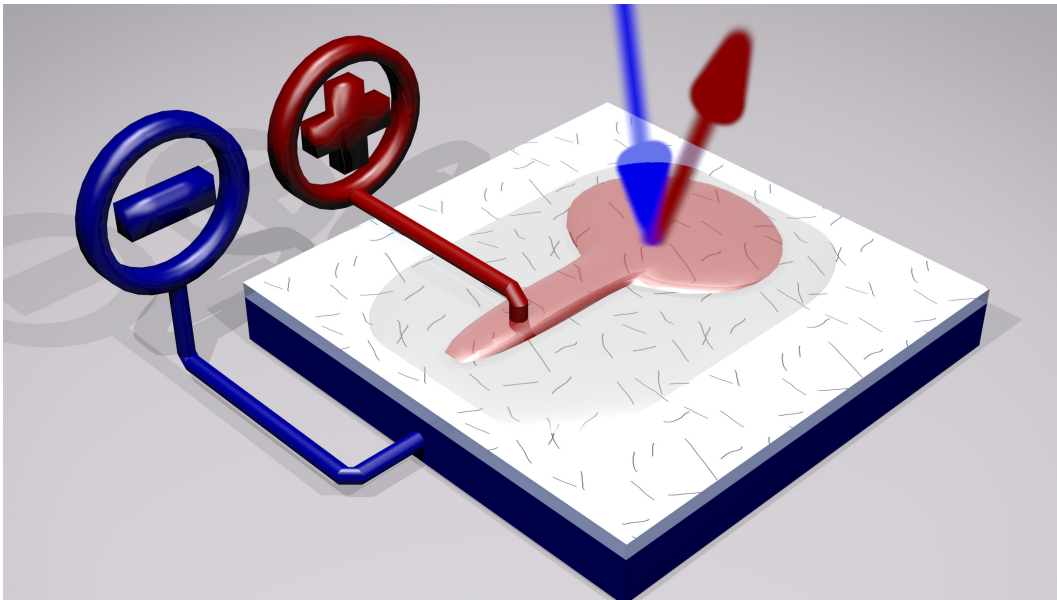


Figure 0.1.: A metal-oxide-semiconductor capacitor for spectroscopy of individual carbon nanotubes



# Zusammenfassung

Halbleitende, einwandige Kohlenstoffnanoröhren (CNTs) weisen abhängig von ihrer Chiralität eine Bandstruktur aufgrund ihres eindimensionalen Gitters auf. Durch Rekombination von Exzitonen emittieren CNTs Photolumineszenzlicht, das je nach Röhrendurchmesser im nahen bis mittleren Infrarotbereich liegt. Vor deren Rekombination diffundieren Exzitonen entlang der Röhre. Dadurch sondieren sie nach Gitterplätzen, welche ein Umklappen ihres Spins verursachen, Exzitonen nicht-strahlend rekombinieren, oder, bei genügend tiefen Temperaturen, Exzitonen in null-dimensionalen Quantenpunkten lokalisieren. Daher zielt die (zeitaufgelöste) Spektroskopie einzelner CNTs nicht nur auf die intrinsische Dynamik von Exzitonen, wie deren Diffusion und Lebenszeit, sondern eben auch auf Störungen der näheren Umgebung oder im Gitter selbst. So können extrinsische und intrinsische Störungen zur Unterdrückung von Photolumineszenzsignalen, zum Aufhellen dunkler Exzitonenzustände oder zur Erzeugung von geladenen Exzitonenzuständen führen.

Im Rahmen dieser Arbeit wurden zur Untersuchung von Exzitonen in CNTs zwei Ansätze verfolgt: Zum einen wurde die CNT Umgebung durch ein statisches elektrisches Feld variiert, zum anderen wurden CNTs von ihrer Umgebung isoliert. Zur Spektroskopie einzelner CNTs fanden verschiedene Techniken der optischen Spektroskopie Anwendung, wie zum Beispiel Anregungsspektroskopie, (zeitlich aufgelöste) Photolumineszenz-Spektroskopie und Photonen-Korrelationsspektroskopie.

Diese Arbeit zeigt die zentrale Rolle von Exzitonenlokalisierung in CNTs bei tiefen Temperaturen auf. So zeigten bei tiefen Temperaturen die Photolumineszenz von CNTs auf dielektrischen Substraten asymmetrische Linienformen und bei steigenden Temperaturen systematische Energieverschiebungen zum Blauen. Zudem war die Photolumineszenz spektraler Diffusion unterworfen, die - wie auch schon von Halbleiter-Quantenpunkten bekannt - durch einzelne Ladungsfluktuatoren im nahen dielektrischen Medium hervorgerufen wurde. Zusätzliche Hinweise auf die Lokalisation von Exzitonen lieferte die nicht-klassische Einzel-Photonen-Emission von kalten CNTs.

Das Hauptaugenmerk lag jedoch auf der Untersuchung einzelner CNTs in statischen elektrischen Feldern. Mittels einer Metall-Oxid-Halbleiter Struktur wurde zunächst die transversale Polarisation von Exzitonen vermessen. Abhängig vom angelegten senkrechten Feld zeigte die Energie der Photolumineszenz eine quadratische Dispersion. Eine Unterklasse von CNTs zeichnet sich jedoch durch mehrere Linien im Emissionsspektrum aus. Aufgrund von der charakteristischen Abstände dieser Linien wurden sie eindeutig dunklen Exzitonenzuständen, genauer Triplet- und "k-momentum"-Zuständen, zugeordnet. Ein weiterer charakteristischer Energieabstand ergab sich in Spektren, die das Aufhellen einer zusätzlichen Linie in Abhängigkeit vom elektrischen Feld zeigten. Diese Linien konnten eindeutig geladenen Exzitonen (Trionen) zugeordnet werden, und entstammen der Dotierung einzelner CNTs mittels Ladungen aus Oxidzuständen des nahen Dielektrikums. Solche Oxidladungen spielten vermutlich auch bei der Veränderung der Anregungsspektren einzelner CNTs eine wichtige Rolle. Da diese Veränderung abhängig vom angelegten Feld war, liegt es nahe, dass sie durch eine Variation des Lokalisationspotentials für Exzitonen verursacht wurde.

Abschließend, dem Einfluss externer Variationen aus dem dielektrischen Medium stehen die einzigartigen optischen Eigenschaften von freihängenden CNTs entgegen. Diese freihängenden Röhren wiesen isoliert lokalisierte Exzitonen und in Konsequenz

sehr schmale Linienbreiten, nahezu intrinsische Lebenszeiten und eine merklich erhöhte Fluoreszenzausbeute auf. Außerdem, zeigten sie selbst auf kürzesten Zeitskalen weder spektrale Diffusion noch Periodizitäten der Intensität.

# Abstract

Semiconducting single-walled carbon nanotubes (CNTs) exhibit a chirality depended band structure of a one-dimensional lattice. Due to the radiative recombination of excitons CNTs emit photoluminescence in the near and mid infrared ranges depending on the tube diameter. Excitons are subject to diffusion along the tube before radiative recombination. Thereby they probe sites that give rise to spin-flips or non-radiative decay, or, at cryogenic temperatures, they localize in zero-dimensional quantum dots at the minima of the local energy potential landscape. Thus, the optical spectroscopy of individual CNTs probes not only the intrinsic exciton dynamics, like diffusion and intrinsic life-time, but also disorder of the CNT lattice and its environment. Intrinsic and extrinsic inhomogeneities and impurities may give rise to photoluminescence quenching, brightening of dark exciton states or generation of charged exciton complexes.

In the framework of this thesis the physics of excitons in CNTs was investigated in two ways: On the one hand their environment was varied with an static electric field, on the other hand the CNTs were isolated from their environment. A comprehensive set of optical spectroscopy techniques was used to study individual CNTs at low temperatures. This included photoluminescence excitation, (time-resolved) photoluminescence, and photon correlation spectroscopy.

This work identified exciton localization as predominant feature of individual CNTs at cryogenic temperatures. CNTs on substrate exhibited asymmetric line shapes at low temperature and temperature dependent shifts on the PL energy. Moreover for constant temperature, PL energies were subject to spectral diffusion, which arose - in analogy to compound semiconductor quantum dots - from interaction with a few close charge fluctuators in the dielectric environment. In addition, evidence for exciton localization was provided by the non-classical photon emission statistics of cryogenic CNTs.

The main focus of this thesis was the study of individual CNTs in a static electric field. A metal-oxide-semiconductor device was used to probe for the transverse polarizability of excitons. In consequence, the PL energy of CNTs exhibited red-shifts as a quadratic function of the perpendicular electric field. However, a subclass of CNTs was characterized by satellite peaks in the emission profile. By their energy splitting they were assigned to PL emission from dark exciton states, e.g. triplet and k-momentum excitons, and resulted presumably from impurity induced symmetry breaking. As a function of the electric field, CNTs with a broken symmetry featured linear shifts of the PL energy of bright and triplet excitons. A third energy scale in the exciton fine structure was manifested by CNTs that exhibited the emergence of a satellite peak as a function of the electric field. These satellites were assigned to the PL of trions generated by doping of individual CNTs with charges from close oxide states. Presumably such close charge states played also an important role in the variation of the excitation spectra of individual CNTs, which was observed as a function of the applied electric field. This variation could be mediated by switching of charge states, which varied the localization potential of excitons.

Finally, the extrinsic effects of the surrounding dielectric medium were contrasted by the remarkable optical properties of as-grown suspended CNTs. Freely suspended CNTs featured isolated localized excitons with narrow linewidths, intrinsic exciton lifetime and a significantly increased quantum yield. Moreover, they lack signatures of spectral diffusion or intermittency even on the shortest timescales.



# Contents

<b>1. Introduction</b>	<b>3</b>
<b>2. Theoretical considerations</b>	<b>7</b>
2.1. Geometric properties . . . . .	7
2.1.1. From graphene to carbon nanotubes . . . . .	7
2.1.2. Symmetry considerations . . . . .	11
2.2. Electronic states in carbon nanotubes . . . . .	13
2.2.1. Electronic properties . . . . .	13
2.2.2. Density of states . . . . .	15
2.2.3. First approach to optical selection rules . . . . .	16
2.3. Excitons . . . . .	18
2.3.1. Screening of Coulomb interaction . . . . .	18
2.3.2. Binding energy . . . . .	18
2.3.3. Symmetry of exciton states . . . . .	21
2.3.4. Selection rules for optical transitions . . . . .	23
2.3.5. Photoluminescence . . . . .	24
2.3.6. Exciton fine structure . . . . .	25
<b>3. Photoluminescence of individual carbon nanotubes</b>	<b>29</b>
3.1. Laser setup and confocal microscope . . . . .	30
3.1.1. Confocal microscope . . . . .	30
3.1.2. Laser power stabilization . . . . .	32
3.2. Sample preparation and characteristics . . . . .	35
3.2.1. Metallic grid . . . . .	36
3.2.2. CoMoCat material . . . . .	36
3.3. Spatially resolving imaging techniques . . . . .	36
3.4. Signatures of individual CoMoCat CNTs . . . . .	39
3.5. Exciton localization at low temperatures . . . . .	41

<b>4. Tuning the photoluminescence with electric fields</b>	<b>47</b>
4.1. Electric field structure . . . . .	48
4.1.1. Growth and characterization of thin films . . . . .	48
4.1.2. Ohmic contacts . . . . .	50
4.2. Capacitance-voltage characterization . . . . .	52
4.2.1. Ideal MOS capacitor . . . . .	52
4.2.2. Measuring the capacitance . . . . .	56
4.2.3. Total charge state density $Q_{\text{tot}}$ . . . . .	57
4.3. Jitter analysis . . . . .	59
4.3.1. Energy jumps . . . . .	60
4.3.2. Intermittency and blinking . . . . .	62
4.4. Classification of CNTs . . . . .	64
4.4.1. Multiple peak emission spectra . . . . .	64
4.4.2. Emission spectra of type A and type B CNTs . . . . .	67
4.5. Electric field sweeps . . . . .	67
4.5.1. Transverse polarizability of excitons . . . . .	68
4.5.2. Permanent dipole moments . . . . .	70
4.6. Emission from trion states . . . . .	74
4.7. Tuning the localization potentials of excitons . . . . .	78
4.7.1. Photoluminescence excitation spectroscopy . . . . .	78
4.7.2. Tuning excitation resonances with the gate voltage . . . . .	81
<b>5. Photon emission statistics</b>	<b>85</b>
5.1. Theoretical introduction . . . . .	86
5.1.1. Second-order correlation function . . . . .	86
5.1.2. Blinking and intermittency . . . . .	88
5.1.3. Single photon emitters . . . . .	90
5.1.4. Photon emission statistics of blinking carbon nanotubes . . . . .	92
5.2. Hanbury-Brown and Twiss interferometer . . . . .	94
5.2.1. Basic considerations . . . . .	94
5.2.2. Hanbury-Brown and Twiss interferometer setup . . . . .	97
5.2.3. Reducing the cross talk . . . . .	99
5.3. Freely suspended carbon nanotubes . . . . .	101
5.3.1. As-grown suspended CNTs . . . . .	102
5.3.2. Methods . . . . .	104
5.3.3. Spectral properties . . . . .	104
5.3.4. Photoluminescence lifetime . . . . .	106

5.3.5. Photon emission statistics . . . . .	107
<b>Summary and perspectives</b>	<b>113</b>
<b>Appendix</b>	<b>119</b>
<b>A. Notation and physical constants</b>	<b>119</b>
A.1. Physical and material constants . . . . .	119
A.2. Symbols and abbreviations . . . . .	120
<b>B. Exchange and trion binding energy</b>	<b>123</b>
<b>C. Protocol for fabrication of layers with individualized carbon nanotubes</b>	<b>125</b>
<b>D. Model for excitation of localized excitons</b>	<b>127</b>
<b>Bibliography</b>	<b>135</b>
<b>List of Publications</b>	<b>157</b>
<b>Danksagung</b>	<b>159</b>



# 1. Introduction

Since carbon nanotubes were observed by Sumio Iijima in 1991<sup>1</sup> [2], investigations and applications of single- and multi-walled nanotubes have triggered great progress in physics [3], chemistry [4], mechanical [5] and electrical engineering [6] as well as biology [7], pharmacy [8] and medicine [9]. Today, carbon nanotubes have become one of the most intensively studied materials in the field of nanotechnology [10]. Formed from a single mono-layer of a hexagonal carbon lattice (graphene) into seamless tubes, carbon nanotubes consist of an almost perfectly-defined lattice down to the atomic scale. Held together by strong covalent carbon-carbon bonds, they exhibit extraordinary mechanical properties [11]. In fact, carbon nanotubes feature the highest reported values of tensile strength [12] and stiffness [13] and thus are now employed routinely for reinforcement of metal composites [14], polymer matrices and ceramics [15]. In 2013 the world-wide production capacity for nanotubes reached a level of 5000 tons per year and is prospected to double within the next 30 months [16].

Carbon nanotubes are either metallic or semiconducting<sup>2</sup>, which depends on the orientation of the hexagonal lattice along the tube [17,18]. The band-gap of semiconducting single-walled carbon nanotubes (CNTs) varies inversely proportional to the diameter with values ranging from a few meV up to 2 eV [19]. Further, CNTs feature an enormous aspect ratio: The diameter of the thinnest CNTs were observed with only 3 Å [20] whereas the length exceeded the limits of the nano-scale with nearly foot-long CNTs reported recently [21]. Thus, CNTs are considered a paradigm system for the study of one-dimensional physics [22], which includes exotic effects of spin-charge separation or Wigner crystals characteristic for one-dimensional Luttinger liquids [23].

CNTs exhibit absorption [24] and emission [25] in the near-infrared and both absorption and photoluminescence (PL) spectroscopy were extensively used to determine the optoelectronic properties of individual CNTs [24–27]. Because of their

---

<sup>1</sup>In 1952 V. Radushkevich and V. M. Lukyanovich [1] reported on their observation of carbon tubes with a diameter of 50 nm. However, their work remained unnoticed for long time until Iijima triggered further investigation of carbon nanotubes.

<sup>2</sup>In the following we consider only semiconducting single-walled carbon nanotubes, which will be abbreviated as CNTs.

## 1. Introduction

excellent optical properties CNTs are proposed for a variety of application in optoelectronics including solar cells [28] as well as efficient photo detectors and emitters [29] that can be tailored specifically to a wavelength by the choice of the tube diameter.

Due to their low-dimensionality CNTs feature generally a reduced screening of the Coulomb interaction [30–33]. The screening affects the entire energy hierarchy giving rise to enormous exciton binding energies, as large as 800-1000 meV for small diameter CNTs in vacuum [34–36]. Thus, the optics of CNTs are dominated by excitons even at room temperature [27,36,37]. There are four exciton ground states, of which only one is optically bright [38]. The lowest energetic exciton state is dipole forbidden by symmetry and termed as the dark exciton. In finite magnetic fields along the CNT axis however, emission from the dark exciton state was observed [39–41]. Further, there is the doubly degenerate k-momentum exciton state. Although radiative recombination from this state is momentum forbidden, it can be brightened given sufficient exciton-phonon coupling [42,43]. Single impurities and ad-atoms were identified to increase spin-orbit coupling and to brighten dark triplet exciton states [44–46]. Furthermore charged exciton states (trions) were observed [47–51].

This thesis considers the spectroscopy of individual CNTs, mainly at cryogenic temperature. As theoretical introduction, *chapter 2* focuses on the different exciton states in CNTs [52]. Beginning with their geometry, we discuss direct and indirect lattices with special regard to symmetry [53]. These geometric considerations are further used to identify the electronic band structure of CNTs and provide numbers for the diameter-dependent band-gap [54]. Based on symmetry considerations, the four states of the exciton singlet manifold and their optical activity are discussed [38]. We include also exciton triplet states [55] and trions [56,57] and present for all small-diameter CNTs an overview on the exciton fine structure and the respective energy-splitting to the bright exciton [34].

*Chapter 3* presents the lay-out and specifications of the experimental setup, namely a confocal microscope operated at cryogenic temperature and a tunable laser source with an actively stabilized power output - a basic requirement for photoluminescence excitation spectroscopy. Further, methods for preparation and efficient characterization of individualized CNTs are addressed. This includes complementary imaging techniques, viz. atomic force microscopy, scanning electron microscopy and micro-luminescence spectroscopy. We present PL spectra from individual CNTs consisting of a single emission line [27,37,58] that is assigned to the bright exciton emission. By variation of the temperature from cryogenic ( $T=4.2$  K) to room temperature, we

identify systematic variation of the PL emission of individual CNTs. Asymmetric line shape [59,60] and temperature induced blue shifts on the PL energy [61–63] are both indicative for the localization of excitons at cryogenic temperature. Exciton localization may arise from singular impurities [62]. PL signals are highly sensitive to variations in the CNT structure as well as the immediate surrounding. Except for two-dimensional atomic layers such as graphene, CNTs exhibit the highest possible surface-to-volume ratio. Since the shell is but a single monolayer, all atoms reside on the tube surface. In pristine CNTs excitons are expected to exhibit an intrinsic lifetime of  $\sim 10$  ns [64,65]. Thus, long exciton diffusion lengths have been observed, which, at room temperature, exceed 200 nm [66] and range up to 610 nm [67] - far beyond the exciton Bohr radius [68]. During diffusion an exciton passes more than ten thousands lattice sites thereby sampling extrinsic and intrinsic inhomogeneities, which give rise to non-radiative recombination channels [69] and exciton dephasing [70]. Hence, the PL intensity of CNTs is sensitive to single disordered sites, be they due to the substrate [71], chemically adsorped atoms or molecules at the tube surface [72,73] or mono-vacancy lattice defects [74]. This quantum-dot-like behavior is apparent in the conductance of single CNTs that is dominated by Coulomb blockade [75]. Further, PL emission from highly localized bright spots along a CNT was also observed in near-field microscopy [58,61]. And finally, also the non-classical photon emission statistics of individual CNTs was associated with the localization of excitons [76,77].

In addition to one peak spectra, *chapter 4* considers also CNTs that feature satellite peaks in their PL spectra. These additional spectral features are assigned to symmetry breaking, which admixes bright and dark exciton states and brightens triplet [78,79] and k-momentum excitons [80]. A third energy scale is manifested by CNTs that exhibit the emergence of a satellite peak as a function of an externally applied electric field. This energy scale agrees with theoretical [55,81] and experimental [47,49,50] reports for the trion emission energy. Exciton charging is presumably generated by doping of CNTs from the surrounding dielectric medium. Furthermore, the transverse polarization of excitons [82] was studied as a function of an electric field perpendicular to the CNT axis. For CNTs with a preserved symmetry the PL showed a quadratic energy dispersion. However, CNTs with a broken symmetry showed linear shifts on the PL energy. Finally, this chapter considers the PL intensity from the bright exciton as a function of the laser detuning. In addition to the higher energetic electronic  $E_{22}$  manifold, the importance of phonon-sidebands is reported for the efficient generation of excitons at cryogenic temperature [83–87].

## 1. Introduction

We use photoluminescence excitation spectroscopy [88] to reveal the excitation spectra of individual CNTs. Within our studies the excitation spectra are varied by means of the externally applied electric field.

*Chapter 5* begins with a brief theoretical discussion of the second-order correlation function and further presents the setup and specifications of a Hanbury-Brown and Twiss interferometer employed for time-resolving spectroscopy. In addition to spectral resolving PL spectroscopy, photon counting spectroscopy is applied in comparative studies of CNTs supported by a dielectric substrate and as-grown suspended CNTs. We record PL lifetime traces and photon emission statistics for both species. All investigated CNTs exhibit non-classical photon emission [76, 77]. However, signatures of photon-bunching [89], which arise from fast intermittency [77], are only present for CNTs interacting with their dielectric surrounding. Due to isolation from any dielectrics as-grown suspended CNTs feature ultra-narrow PL linewidth, nearly intrinsic exciton lifetime, and a significantly increased quantum yield.

The thesis concludes with a final summary giving an overview on our findings. As an outlook it proposes for further experimental investigation, which could benefit from the remarkable optical properties of as-grown suspended CNTs presented here.

## 2. Theoretical considerations

The following theoretical introduction gives a brief overview of the physical properties of pristine single-walled carbon nanotubes<sup>1</sup>. Starting with a mono-layer of graphene, carbon nanotubes are discussed with regard to their geometric characteristics that determine all other physical properties. For a deeper understanding it is fruitful to consider the symmetry of pristine carbon nanotubes, which allows to predict the impact of symmetry breaking due to external perturbations or single lattice defects. A main focus lies on the optical properties that can be understood in terms of creation of bound electron-hole pairs (excitons) and their decay.

### 2.1. Geometric properties

#### 2.1.1. From graphene to carbon nanotubes

##### Direct lattice

Graphene is formed as mono-atomic (two-dimensional) hexagonal lattice by  $sp^2$ -hybridized carbon atoms each bonding with three neighboring atoms [90]. A section of this honeycomb lattice is illustrated in Fig. 2.1(a). The unit cell consists of two atoms, which define two intersecting sublattices. The lattice vectors  $\vec{a}_1$  and  $\vec{a}_2$  are commonly defined by

$$\vec{a}_1 = \begin{pmatrix} \frac{3}{2} \\ \frac{\sqrt{3}}{2} \end{pmatrix} \cdot a_{cc} \quad \text{and} \quad \vec{a}_2 = \begin{pmatrix} \frac{3}{2} \\ -\frac{\sqrt{3}}{2} \end{pmatrix} \cdot a_{cc} \quad (2.1)$$

where  $a_{cc} = 0.142$  nm gives the bond length between two carbon atoms.

For illustrative creation of a carbon nanotube a graphene ribbon rolls up to form a seedless cylinder. The resulting tubes differ in their diameter  $d_t$  and in the orientation of the honeycomb lattice with respect to the cylinder axis. Both, the orientation and the diameter, are determined by the chiral vector  $\vec{C}_h$ , which connects two crystallographic equivalent lattice sites. These sites come to lie on each other when a

---

<sup>1</sup>We emphasize that this thesis considers only single-walled carbon nanotubes.

## 2. Theoretical considerations

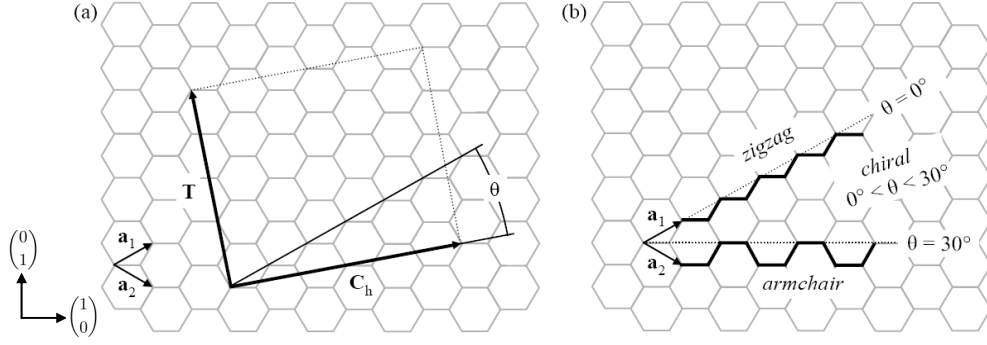


Figure 2.1.: **Construction of a carbon nanotube from a layer of graphene:** The grey honeycomb lattice and the basis vectors  $\vec{a}_1$  and  $\vec{a}_2$  are depicted. (a) The construction of a tube with the chiral index (4,2) results in the translation vector  $\vec{T}$  and the chiral vector  $\vec{C}_h$ , that includes the chiral angle  $\theta$  with  $\vec{a}_1$ . (b)  $\theta$  defines three classes of carbon nanotubes: zig-zag ( $\theta = 0^\circ$ ), armchair ( $\theta = 30^\circ$ ) and chiral ( $0^\circ < \theta < 30^\circ$ ). (Adapted from Ref. [91])

graphene ribbon is rolled up to a nanotube.  $\vec{C}_h$  can be expressed as the sum of integer multiples of  $\vec{a}_1$  and  $\vec{a}_2$

$$\vec{C}_h = n \cdot \vec{a}_1 + m \cdot \vec{a}_2 \quad \text{with } n, m \in \mathbb{N}. \quad (2.2)$$

Hence, the integers  $n$  and  $m$  are sufficient to describe explicitly the nanotube structure. Commonly, they are used in the form  $(n, m)$  termed as chiral index or chirality of a carbon nanotube. Due to the symmetry of graphene, a tube with the chiral index  $(x, y)$  is identical to a second with  $(y, x)$ . Therefore, it is a common convention that  $n \geq m$  without loss of generality.

An infinitely long carbon nanotube is invariant under translation of integer multiples of the unit translation vector  $\vec{T}$  along the tube axis. Hence,  $\vec{T}$  is always perpendicular to  $\vec{C}_h$ :

$$\vec{C}_h \cdot \vec{T} = 0. \quad (2.3)$$

To determine the unit translation vector - the shortest of all vectors perpendicular to  $\vec{C}_h$  - we express  $\vec{T}$  in the basis of  $\vec{a}_1$  and  $\vec{a}_2$ . Further, we use the condition that  $t_1$  and  $t_2$  (of the shortest vector) do not have a common divisor other than 1:

$$\vec{T} = t_1 \vec{a}_1 + t_2 \vec{a}_2 = \frac{2m + n}{d_R} \vec{a}_1 + \frac{2n + m}{d_R} \vec{a}_2. \quad (2.4)$$

Here,  $d_R$  is defined as the greatest common divisor of  $2n + m$  and  $2m + n$ . Knowing

$\vec{C}_h$  and  $\vec{T}$ , we can deduce the number of hexagons per unit cell  $N$ . The area of the nanotube unit cell is given by  $|\vec{C}_h \times \vec{T}|$ , whereas the area of the graphene unit cell by  $|\vec{a}_1 \times \vec{a}_2|$ . Thus, we can write

$$N = \frac{|\vec{C}_h \times \vec{T}|}{|\vec{a}_1 \times \vec{a}_2|} = \frac{2(n^2 + nm + m^2)}{d_R} . \quad (2.5)$$

As two carbon atoms form the basis of the graphene unit cell, the number of carbon atoms per nanotube unit cell equals  $2N$ .

The chiral angle  $\theta$  is enclosed between  $\vec{C}_h$  and  $\vec{a}_1$ . It is connected to the chiral index  $(n, m)$  by<sup>2</sup>

$$\theta = \arctan \left( \frac{\sqrt{3}m}{2n + m} \right) \quad (2.6)$$

and is limited to  $0^\circ \leq \theta \leq 30^\circ$  since  $n \geq m$ . As some carbon nanotubes exhibit additional symmetries it is helpful to distinguish between three major classes. Firstly, *zig-zag* nanotubes are characterized by  $\theta = 0^\circ$  or the chiral index  $(n, 0)$ , secondly, *armchair* nanotubes by  $\theta = 30^\circ$  or  $(n, n)$ . We will show below that both have additional symmetry planes [92] and are achiral. Those CNTs without these symmetry planes form the third class: *chiral* nanotubes with  $0^\circ < \theta < 30^\circ$  and accordingly  $(n, m)$  with  $0 < m < n$ . Fig. 2.1 depicts  $\vec{C}_h$ ,  $\vec{T}$ , and  $\theta$  for the construction of a chiral carbon nanotube with chiral index  $(4, 2)$ . Furthermore, it shows the circumferential bonding path for armchair and zig-zag nanotubes, respectively. Their respective path shape is eponym for these classes. Since the tube circumference is given by the length of  $\vec{C}_h$ , its diameter  $d_t$  can be expressed in terms of the chiral index  $(n, m)$  by

$$d_t = \frac{|\vec{C}_h|}{\pi} = \frac{\sqrt{3}}{\pi} a_{cc} \sqrt{m^2 + mn + n^2} . \quad (2.7)$$

### Reciprocal space

The reciprocal lattice of graphene is also hexagonal. It is spanned by the reciprocal lattice vectors  $\vec{b}_1$  and  $\vec{b}_2$ :

$$\vec{b}_1 = \begin{pmatrix} \frac{1}{\sqrt{3}} \\ 1 \end{pmatrix} \cdot \frac{2\pi}{a_{cc}} \quad \text{and} \quad \vec{b}_2 = \begin{pmatrix} \frac{1}{\sqrt{3}} \\ -1 \end{pmatrix} \cdot \frac{2\pi}{a_{cc}} . \quad (2.8)$$

---

<sup>2</sup>since  $\cos \theta = \frac{\vec{C}_h \cdot \vec{a}_1}{|\vec{C}_h| |\vec{a}_1|}$

## 2. Theoretical considerations

For a carbon nanotube it is useful to express all reciprocal vectors in the basis of the following two vectors:  $\vec{K}_1$  that accounts for the vector component along the nanotube axis and  $\vec{K}_2$  that accounts for the circumferential component only. That is to say,  $\vec{K}_1$  ( $\vec{K}_2$ ) is the reciprocal vector of  $\vec{T}$  ( $\vec{C}_h$ ). Therefore we can write

$$\begin{aligned} \vec{C}_h \cdot \vec{K}_1 &= 2\pi & \vec{T} \cdot \vec{K}_2 &= 2\pi \\ \vec{T} \cdot \vec{K}_1 &= 0 & \vec{C}_h \cdot \vec{K}_2 &= 0 . \end{aligned} \quad (2.9)$$

Using Eqs. (2.2), (2.4), and (2.8), the basis vectors of the reciprocal lattice can be expressed as a function of the chiral index  $(n, m)$  by

$$\begin{aligned} \vec{K}_1 &= \frac{2n + m}{Nd_R} \vec{b}_1 - \frac{2m + n}{Nd_R} \vec{b}_2 \\ \vec{K}_2 &= \frac{m}{N} \vec{b}_1 - \frac{n}{N} \vec{b}_2 \end{aligned} \quad (2.10)$$

where  $N$  is the number of hexagons per unit cell given in Eq. (2.5). When a graphene ribbon is rolled up to a nanotube, any reciprocal wave vector  $\vec{k}$  is composed of a component along the tube axis  $k_{\parallel}$  and a circumferential component  $k_{\perp}$ :

$$\vec{k} = k_{\perp} \vec{K}_1 + k_{\parallel} \vec{K}_2 . \quad (2.11)$$

Within the first Brillouin zone the parallel component  $k_{\parallel}$  can take any quasi-continuous value<sup>3</sup> within  $[-\frac{\pi}{|\vec{T}|}, \frac{\pi}{|\vec{T}|}]$ , whereas the circumferential component  $k_{\perp}$  must fulfill an additional boundary condition. Due to destructive interference, all wave functions that do not exhibit a phase shift of  $2\pi$  (or multiples of  $2\pi$ ) around the nanotube circumference vanish. Hence,  $k_{\perp}$  is constrained to the values

$$k_{\perp} = \mu \frac{2\pi}{|\vec{C}_h|} \quad (2.12)$$

where  $\mu$  is an integer. Since a minimum of four carbon atoms is needed to define the wavelength and every unit cell consists of  $2N$  atoms,  $\mu$  is limited to integer values<sup>4</sup> within  $[-\frac{N}{2}, \frac{N}{2}]$ . In the following, the axial component  $k_{\parallel}$  is simply denoted by  $k$  and the circumferential component by its quantum number  $\mu$ .

Fig. 2.2 illustrates the allowed states (as cutting lines due to zone folding, see Chap. 2.3) for a representative of each major group. Due to limited space, only the

<sup>3</sup>Here, an infinitely long carbon nanotube is assumed.

<sup>4</sup>In fact, the state  $-\frac{N}{2}$  is equivalent to  $\frac{N}{2}$ . Since this state should not be counted twice, either  $-\frac{N}{2}$  or  $\frac{N}{2}$  must be excluded.

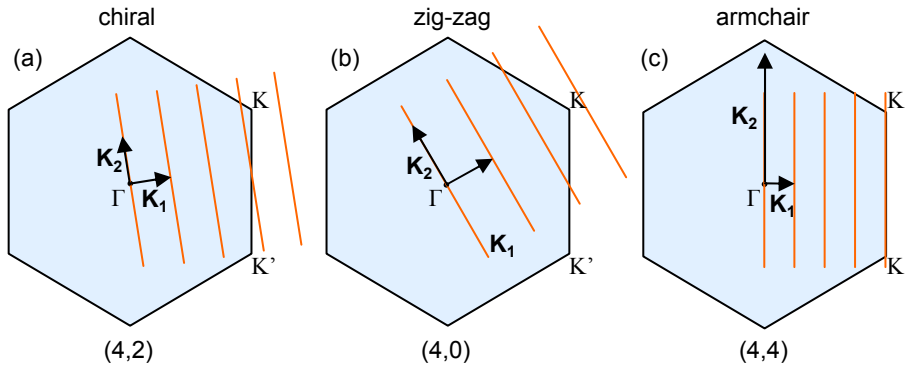


Figure 2.2.: **Reciprocal lattice of three different carbon nanotubes:** First Brillouin zone of graphene and basis vectors  $\vec{K}_1$  and  $\vec{K}_2$  of a carbon nanotube (not to scale). The allowed states (*cutting lines*) are depicted as orange solid lines for a chiral (a), zig-zag (b) and armchair nanotube (c).

first Brillouin zone of graphene is depicted. Of course, a substantial analysis would require the entire first Brillouin zone of the nanotube that consists of  $N$  hexagons. Nevertheless, the illustration exemplifies the main argument. While the allowed states can intersect with the  $K$  or  $K'$  point in some chiral and zig-zag nanotubes, this is always the case for armchair nanotubes. According considerations will play an important role in the analysis of the electronic properties of carbon nanotubes discussed in Chap. 2.2.

### 2.1.2. Symmetry considerations

The symmetry of a system determines many of its physical properties. For example in an atom (molecule), the symmetry of the atomic (molecular) orbitals defines the allowed optical transitions. Likewise, the optical activity of (organic) molecules requires the lack of any axis of improper rotation [93]. Thus, examining a system with regard to its symmetry facilitates calculations and may even enable for computation-free predictions.

As shown in the previous paragraphs, carbon nanotubes exhibit an one-dimensional lattice that is composed of a periodical sequence of unit cells along the translation vector  $\vec{T}$ . The line groups contain all symmetries of such a system. These were originally reported for all carbon nanotubes by Damnjanovic et al. [92]. It will be briefly summarized here since the notation will be used in the following analysis of exciton states and selection-rules for optical transitions. An instructive review

## 2. Theoretical considerations

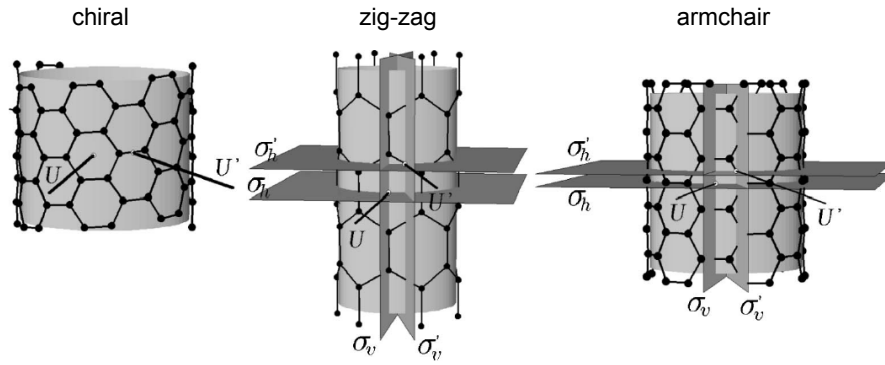


Figure 2.3.: **Symmetry for chiral, zig-zag and armchair carbon nanotubes:** All carbon nanotubes are symmetric under rotations around  $U$  and  $U'$ , which are generally denoted by  $C'_2$  and  $C''_2$ , respectively. Achiral tubes (zig-zag and armchair) show symmetry mirror planes both horizontally ( $\sigma_h, \sigma'_h$ ) and vertically ( $\sigma_v, \sigma'_v$ ). Not depicted: All tubes are additionally symmetric under screw operations around the tube axis. Achiral tubes are further symmetric under rotations around the tube axis. (Adapted from Ref. [92])

on the symmetry-related properties of carbon nanotubes was published by Barros et al. [53].

Damnjanovic et al. started out with a mono-layer of graphene and investigated the preservation of its translation symmetry upon a carbon nanotube. Graphene is symmetric under rotations of  $180^\circ$  around every lattice site or the midpoint of every bonding. As illustrated in Fig. 2.3, these symmetries are preserved in all carbon nanotubes with the  $C'_2$  ( $U$ ) and  $C''_2$  ( $U'$ ) axis, respectively. Pure translation symmetries of graphene turn into pure rotation or screw symmetries in carbon nanotubes. One can make simple and illustrative predictions by considering a tube with chiral index  $(n, m)$ . If its chiral vector  $\vec{C}_h$  can be divided into parts - that is the greatest common divisor of  $n$  and  $m$  (here denoted as  $d_n$ ) is greater than 1 -, the tube is symmetric under rotations by  $\frac{2\pi}{d_n}$  around its axis. The associated line group is termed as  $C_{d_n}^s$  (with  $s = 0, 1, \dots, d_n - 1$ ). Whereas chiral tubes never feature any mirror planes, achiral tubes are additionally symmetric to mirror and glide<sup>5</sup> planes, which are depicted in Fig. 2.3.

Mathematically these symmetries are summarized in line groups. Every line group  $\mathbf{L}$  is a product of a point group  $\mathbf{P}$  and an infinite cyclic group  $\mathbf{T}$  of generalized translations. For determination of the electronic properties it is sufficient to consider the point group only. Thus, translational symmetries  $\mathbf{T}$  will be neglected in the follow-

<sup>5</sup>That is a combination of mirroring at a plane and a successive translation.

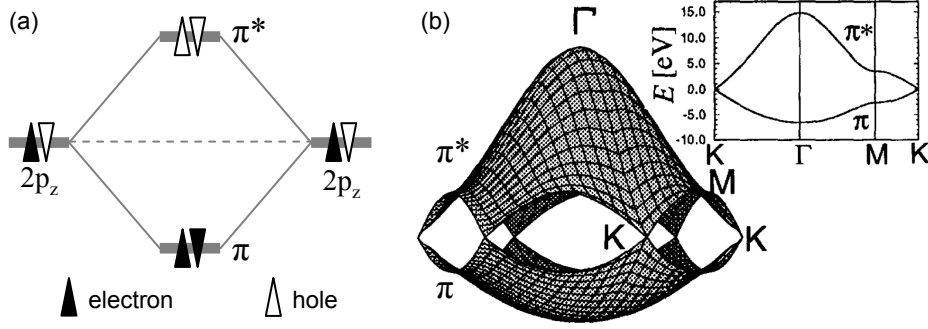


Figure 2.4.: **Electronic properties of graphene** (a) Two  $p_z$  orbitals form one bonding ( $\pi$ ) and one anti-bonding ( $\pi^*$ ) state. (b) Valence band ( $\pi$ ) and conduction band ( $\pi^*$ ) in the first Brillouin zone. (Adapted from Ref. [90])

ing. The point group of a chiral nanotube is  $\mathbf{D}_{d_n}$  whereas achiral nanotubes exhibit higher symmetry  $\mathbf{D}_{nh}$ . We will further use the line group notation to represent irreducibly an electronic state:

$${}_k\mathbf{X}_\mu^\Pi. \quad (2.13)$$

Here,  $\mu$  denotes the circumferential quantum number,  $\Pi$  the parity under  $C_2$  rotations and  $k$  the wave vector along the tube.  $\mathbf{X}$  can take the values  $\mathbf{A}$ ,  $\mathbf{B}$  or  $\mathbf{E}$ . The first two denote non-degenerate representations that are either even ( $\mathbf{A}$ ) or odd ( $\mathbf{B}$ ) under vertical reflection.  $\mathbf{E}$  is the doubly degenerate representation. The complete character tables for the  $\mathbf{D}_n$  point group and thus for chiral nanotubes can be found in Ref. [53].

## 2.2. Electronic states in carbon nanotubes

### 2.2.1. Electronic properties

By analogy with the geometric properties of carbon nanotubes, which we have deduced from those of graphene earlier in this chapter, we will deduce their electronic properties on the basis of the graphene band structure. Instead of allowing all possible states, we just consider the periodic boundary conditions given by Eq. (2.12) and the resulting constraints on possible wave vectors. This *zone-folding* gives an illustrative and rough estimation of the electronic properties of a carbon nanotube - even though it neglects all effects that arise from the tube curvature.

We begin with a single carbon atom that has four valence electrons distributed

## 2. Theoretical considerations

among the  $2s$ ,  $2p_x$ ,  $2p_y$  and  $2p_z$  orbital [93]. The first three of them are hybridized to the in-plane  $sp^2$  states that form  $\sigma$  bonds each with one of the three neighboring carbon atoms. Each pair of these three bonds include an angle of  $120^\circ$ , which takes shape in the previously discussed hexagonal lattice of graphene. Perpendicular to this plane, the  $2p_z$  orbitals form weaker  $\pi$  bonds, which are illustrated in Fig. 2.4(a). Due to this orthogonality, discussions of electrons in  $\pi$  and  $\sigma$  bonds can be separated. Since the  $\sigma$  electrons are strongly bound, they can be neglected for the derivation of the optical and electronic properties. Reich et al. reported a common approach including a nearest neighbor tight-binding approximation with special regard to carbon nanotubes [94]. The dispersion of the bonding  $\pi$  and the anti-bonding  $\pi^*$  orbitals forms the valence band ( $v$ ) and the conduction band ( $c$ ), respectively. The electronic energy dispersion for graphene is approximated by<sup>6</sup>

$$E_{v(c)}(\vec{k}) = \frac{\varepsilon_{2p} \begin{smallmatrix} + \\ - \end{smallmatrix} \gamma_0 w(\vec{k})}{1 \begin{smallmatrix} + \\ - \end{smallmatrix} s w(\vec{k})} \quad (2.14)$$

with

$$w(\vec{k}) = \sqrt{1 + 4 \cos\left(\frac{3k_x a_{cc}}{2}\right) \cos\left(\frac{\sqrt{3}k_y a_{cc}}{2}\right) + 4 \cos^2\left(\frac{\sqrt{3}k_y a_{cc}}{2}\right)}. \quad (2.15)$$

Limiting the interaction only between nearest neighbors, the parameters are  $\varepsilon_{2p} = 0$ ,  $s = 0.129$  and the nearest-neighbor interaction  $\gamma_0 = -3.033$  eV [90]. Both dispersion relations are illustrated in Fig. 2.4(b). The fully occupied valence band ( $\pi$ ) and the empty conduction band ( $\pi^*$ ) are separated by an energy gap and intersect only at the  $K$  and  $K'$  points located at the zone boundary. Since the density of states at these points is zero, graphene is a semi-metal. At the  $K$  ( $K'$ ) points the bands form a Dirac cone with a linear dispersion for electron and holes. As the second derivative of the dispersion relation vanishes, electrons and holes feature an accordingly vanishing effective mass close to the  $K$  and  $K'$  points. This is the main reason for the unique electronic properties of graphene.

With regards to carbon nanotubes, we now use the aforementioned zone-folding approach and limit the wave vectors to those that fulfill the circumferential periodic boundary condition. Using Eq. (2.12),  $E_{v(c)}(\vec{k})$  is now limited in the circumferential

---

<sup>6</sup> $\varepsilon_{2p}$ ,  $\gamma_0$  and  $s$  are used as fitting parameters though they represent the orbital energy of the  $2p_z$  orbital, the transfer integral and the overlap integral with the nearest neighbor, respectively [90].

direction to a few possible values  $\mu$ . Therefore, we can write

$$E_{v(c)}(\mu, k) = E_{v(c)}\left(k \frac{\vec{K}_1}{|\vec{K}_1|} + \mu \vec{K}_2\right) \quad \text{with} \quad -\frac{\pi}{|\vec{T}|} < k < \frac{\pi}{|\vec{T}|} \quad \text{and} \quad \mu = -\frac{N}{2}, \dots, \frac{N}{2} . \quad (2.16)$$

Using the explicit expressions for  $\vec{K}_1$  and  $\vec{K}_2$  given in Eq. (2.10), we obtain

$$w(\vec{k}) \rightarrow w(\mu, k) = \left[ 1 + 4 \cos\left(\frac{\pi\mu(2n+m)}{2(n^2+nm+m^2)} + \frac{mTk}{2N}\right) \times \right. \\ \left. \cos\left(\frac{3\pi\mu m}{2(n^2+nm+m^2)} - \frac{(2n+m)Tk}{2N}\right) \right. \\ \left. + 4 \cos^2\left(\frac{\pi\mu(2n+m)}{2(n^2+nm+m^2)} + \frac{mTk}{2N}\right) \right]^{\frac{1}{2}} . \quad (2.17)$$

Since the conduction and valence band intersect only at the  $K$  ( $K'$ ) points in graphene, it is a purely geometric problem to distinguish between metallic and semiconducting carbon nanotubes. In metallic tubes the allowed states intersect with  $K$  or  $K'$ , whereas the allowed states include neither  $K$  nor  $K'$  in semiconducting nanotubes. It turns out [95] that  $(2n+m)$  is a crucial value, which allows to distinguish between three cases<sup>7</sup>:

$$\begin{aligned} \text{mod}(2n+m, 3) = 0 & \quad \text{metallic} \\ \text{mod}(2n+m, 3) = 1 & \quad \text{semiconducting S1} \\ \text{mod}(2n+m, 3) = 2 & \quad \text{semiconducting S2} . \end{aligned} \quad (2.18)$$

As mentioned above, the cutting lines for armchair tubes  $(n, n)$  always intersect at  $K$  and  $K'$  so these are always metallic. In contrast, the two tubes depicted in Fig. 2.2(a,b) are semiconducting S2 since their cutting lines do not intersect with  $K$  and  $K'$ . Some publications use  $\text{mod}(n-m, 3)$  to distinguish between semiconducting and metallic tubes. Although this notation is equivalent with regard to the here roughly considered electronic properties, distinguishing  $2n+m$  families is more significant with regard to many other physical properties (family patterns).

### 2.2.2. Density of states

The density of states  $n(E)$  (abbreviated by DOS) gives the number of electronic states either in the conduction or the valence band within an energy range from  $E$  to

<sup>7</sup> $\text{mod}(x,y)$  denotes the modulo operation:  $x$  modulo  $y$ .

## 2. Theoretical considerations

$E + \Delta E$  (for a small  $\Delta E$ ). Mintmire et al. had first reported on the universal DOS of carbon nanotubes [96]. Following their considerations for a doubly degenerated band, the DOS can be expressed as

$$n(E) = \frac{2}{N|\vec{K}_2|} \sum_i \int dk \delta(k - k_i) \left| \frac{\partial E}{\partial k} \right|^{-1}. \quad (2.19)$$

Here,  $k_i$  denotes the roots of the equation  $E - E(k_i) = 0$ , and the denominator  $N|\vec{K}_2|$  equals the length of the nanotube Brillouin zone. At any local extremum  $\frac{\partial E}{\partial k} = 0$  gives rise to a singularity in the DOS, which is termed as van-Hove singularity (vHs) [97]. Mintmire et al. focus on the region close to  $K$  and  $K'$  where the energy dispersion is linear. Thus, the partial differentiation is reduced by using the circumferential quantization and by introducing

$$E_\mu = \frac{|3\mu - n + m| a_{cc} |\gamma_0|}{2 d_t}. \quad (2.20)$$

So, the DOS can be written as [96]

$$n(E) = \frac{2\sqrt{3}a_{cc}}{\pi^2\gamma_0 d_t} \sum_{\mu=-\frac{N}{2}}^{\frac{N}{2}} \begin{cases} |E|/\sqrt{E^2 - E_\mu^2}, & \text{for } |E| > |E_\mu| \\ 0, & \text{for } |E| < |E_\mu| \end{cases}. \quad (2.21)$$

The DOS is divergent whenever  $|E| = |E_\mu|$ . Hence, the vHs can be numbered by the same quantum number  $\mu$  that originates from the circumferential boundary condition. Figs. 2.5(a) and (b) depict the DOS for a quasi-metallic and a semiconducting carbon nanotube, respectively. As noted before,  $\text{mod}(2n+m, 3) = \text{mod}(n-m, 3) = 0$  holds for (quasi-)metallic nanotubes. For such tubes the nominator in Eq. (2.20) equals  $|3\mu|$ . Since  $E_m$  equals zero for at least one  $\mu$ , the density of state does not vanish in the vicinity of  $E = 0$ . In contrast, semiconducting tubes exhibit a band gap. The size of this gap  $E_{11}$  scales with the inverse of the tube diameter  $d_t$  as depicted in the Kataura plot in Fig. 2.5(c). This plot illustrates also a common family pattern. That is to say, a nanotube belonging to S1 family has a bigger  $E_{11}$  (smaller  $E_{22}$ ) than a nanotube with similar diameter from the S2 family. In the following, only semiconducting carbon nanotubes are considered, which are abbreviated by CNT.

### 2.2.3. First approach to optical selection rules

We are still considering a one particle problem that will be later refined to a more elaborate discussion, which also includes excitonic effects. Already the knowledge

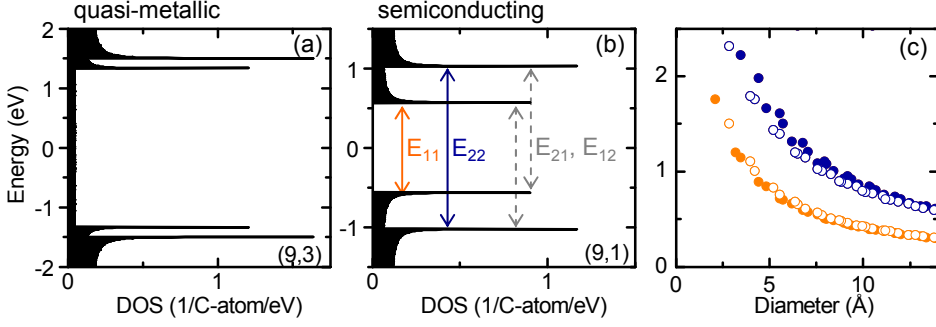


Figure 2.5.: **Density of states and Kataura plot:** (a) Density of states of a quasi-metallic nanotube (9,3) showing van-Hove singularities (vHs) but in contrast to graphene a non-vanishing density of states at zero energy. (b) Density of states of a semiconducting nanotube (9,1) exhibiting vHs with a band gap. The allowed optical transitions  $E_{11}$  and  $E_{22}$  have purely axial components ( $\Delta\mu = 0$ ) whereas  $E_{12}$  and  $E_{21}$  change the circumferential momentum by  $\Delta\mu = \pm 1$ . (c) *Kataura plot* showing  $E_{11}$  (orange) and  $E_{22}$  (blue circles) as a function of the tube diameter. The family pattern is illustrated by the open (S1) and filled (S2) circles. (All data depicted here were originally reported by Maruyama [98].)

of the DOS allows to identify selection rules for optical transitions. The absorption (emission) of a photon can be described by the transition of an electron from a valence to a conduction band. Since the DOS diverges at the vHs, transitions are highly effective whenever they interconnect two vHs. We will consider only transitions over the CNT band gap. Light polarized parallel to the CNT axis will not change the electrons circumferential momentum  $\mu$ . Thus, the selection rule for light emitted or absorbed parallel to the axis implies  $\Delta\mu = 0$  and the occurring transition energies are  $E_{11}$ ,  $E_{22}$  and so forth. The first two transitions are depicted as solid lines in Fig. 2.5(b).

The situation is different if we consider perpendicular polarized light. If we unfold the CNT back to a graphene layer, the polarization vector would transform into in-plane and out-of-plane polarizations. These polarizations are periodically modulated with  $\pi/d_t$  along  $\vec{K}_1$  [53] (whereas the polarization vector of light polarized parallel to the axis light would be still parallel to  $\vec{K}_2$ !). The allowed electron wave vectors along  $\vec{K}_1$  differ by  $\mu\vec{K}_1$ . Due to momentum conservation we can write  $\vec{k}_c = \vec{k}_v \pm \vec{K}_1$  where the photon momentum equals  $\vec{K}_1$ . Accordingly, the selection rule for light polarized perpendicular to the tube axis is given by  $\Delta\mu = \pm 1$ . The transitions  $E_{21}$  and  $E_{12}$  are indicated as dashed lines in Fig. 2.5(b). Interestingly for perpendicular polarized light, the effective photon momentum is not given by the photon wavelength  $\lambda$  but by the periodicity  $\pi/d_t$  of the in-plane and out-of-plane polarization modulation. Since

## 2. Theoretical considerations

$d_t \ll \lambda$ , these photons carry a much higher "pseudo momentum" than in free space. Nevertheless, the depolarization of light polarized perpendicular to the tube axis strongly suppresses the coupling to electronic states [99]. Therefore the transitions  $E_{12}$ ,  $E_{21}$  et cetera are orders of magnitude smaller in intensity [100] and will be neglected in the following.

### 2.3. Excitons

Up to now our considerations regarded single electrons only (one particle picture). We will now refine our considerations by including also many-body effects and the Coulomb interaction between electrons and holes.

#### 2.3.1. Screening of Coulomb interaction

The Coulomb interaction between two charge carriers in any bulk material is generally reduced as compared to free space. The electric field of both charge carriers polarizes lattice atoms and thus induces attenuating, opposing fields. For two distant charges the lattice can be regarded as a homogenous medium with the static dielectric constant  $\epsilon$ . The dielectric constant is well approximated by  $\epsilon_{\text{vac}} = 1.846$  for CNTs freely suspended in vacuum [34].

However, CNTs are of small diameter and hence the electric field lines between two charges are not confined to the tube itself. Rather, they leak into the medium around a CNT. Thus, the dielectric properties of the environment play a crucial role for Coulomb interactions between two charge carriers on a CNT. The Coulomb energies must be further rescaled to account for the environmental dielectric constant  $\epsilon_{\text{med}}$ . As shown by Perebeinos et al. [33] all Coulomb energies between two charges in a CNT scale as

$$\frac{E_{\text{med}}}{E_{\text{vac}}} = \left( \frac{\epsilon_{\text{med}}}{\epsilon_{\text{vac}}} \right)^{-1.40}, \quad (2.22)$$

which is valid for dielectric media with  $\epsilon_{\text{med}} = 2 - 15$ .

#### 2.3.2. Binding energy

The optical properties of semiconductors are determined by the formation of bound electron-hole states termed as excitons and become particularly apparent for photon energies below the semiconductor band gap  $E_g$ . If electrons and holes are weakly

bound (Mott-Wannier excitons), the electron-hole separation exceeds the lattice constant. Their binding energy can be considered in a hydrogen-like model [97] as

$$E_{\zeta} = E_g - \frac{m^* e^4}{2\hbar^2 \epsilon^2 \zeta^2} . \quad (2.23)$$

The Rydberg equation is rescaled by the reduced mass  $m^*$  to account for the semiconductor band structure and by  $\epsilon$  to account for the screening of the Coulomb potential. The positive integer  $\zeta$  denotes the energy level of the bound state.

However, this model is only a rough approximation because it neglects the low-dimensional structure and the curvature of CNTs. On the one hand, the low-dimensionality gives rise to enhanced Coulomb interaction, which results in Wannier-like excitons with strong binding energies  $E_B$  of a few hundred meV up to 1 eV [36]. On the other hand, the enhanced Coulomb interaction expands the single particle band gap termed as band gap renormalization (BGR). Whereas in a single particle picture the lowest energy of an excited electron is given by  $E_{11}$ , the lowest energy of an exciton reads as [101]

$$E_X = E_{11} + E_{BGR} - E_B . \quad (2.24)$$

An analytical expression for the exciton binding energy  $E_B$  has been reported by Capaz et al. [34] and is briefly presented here. The analytical approximation of  $E_B$  and the exciton Bohr radius  $\alpha_B$  reads as<sup>8</sup>

$$E_B = \frac{1}{d_t} \left( A + \frac{B}{d_t} + C\xi + D\xi^2 \right) \quad (2.25)$$

$$\alpha_B = d_t (E + F\xi + G\xi^2) .$$

The respective chirality is considered by using the chirality variable  $\xi$ . This accounts for the respective family  $\nu$  (compare S1 and S2 in Eq. 2.18) and is defined as [54]

$$\xi = (-1)^\nu \cos(3\theta) \quad \text{and} \quad \nu = \text{mod}(2n + m, 3) . \quad (2.26)$$

---

<sup>8</sup> All values are given for vacuum environment  $\epsilon = 1.846$ .

$A = 0.6724 \text{ eV nm}$	$B = -4.910 \cdot 10^{-2} \text{ eV nm}^2$
$C = 4.577 \cdot 10^{-2} \text{ eV nm}^2$	$D = -8.325 \cdot 10^{-3} \text{ eV nm}^3$
$E = 1.769$	$F = -2.490 \cdot 10^{-1} \text{ nm}$
$G = 9.130 \cdot 10^{-2} \text{ nm}^2$	

## 2. Theoretical considerations

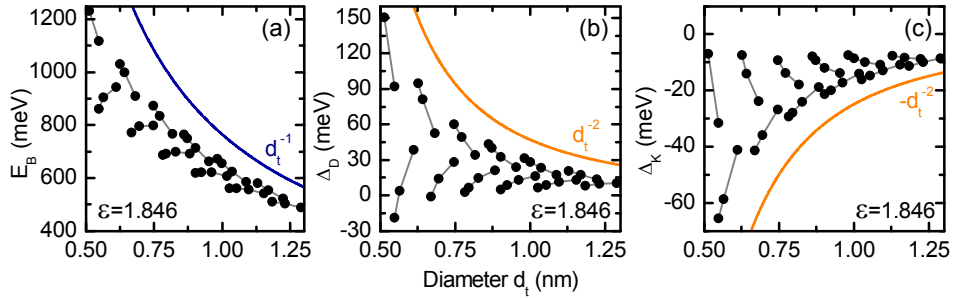


Figure 2.6.: **Theoretical values for binding energy and exciton energy splitting:** Binding energy  $E_B$  (a), bright-dark splitting  $\Delta_D$  (b), and splitting between bright and k-momentum exciton  $\Delta_K$  (c) as a function of the tube diameter  $d_t$ . In all panels family patterns are highlighted by grey solid lines that connect CNTs belonging to the same family. The blue (orange) solid lines are guide to the eyes following  $d_t^{-1}$  ( $\pm d_t^{-2}$ ). (Calculations analogous to [34])

Like for the band gap  $E_{11}$  given in Eq. (2.20), the leading term of  $E_B$  scales inversely with the tube diameter  $1/d_t$  as depicted for small diameter CNTs in Fig. 2.6(a). In addition,  $E_B$  shows distinct family patterns: Within a family with  $\nu = 1$  ( $\nu = 2$ ) CNTs with smaller diameter spread out to a higher (lower) binding energy. In Fig. 2.6(a) this is highlighted by the grey solid lines that interconnect CNTs belonging to the same family.

It turns out [102] that the effect of the binding energy  $E_B$  is only slightly overcompensated by  $E_{BGR}$ . Thus, the lowest exciton energy is only marginally higher than  $E_{11}$  depicted in the one-particle Kataura plot in Fig. 2.5(c). Nevertheless, the high exciton binding energy plays an important role. Its magnitude of up to 1 eV is enormous compared to the exciton binding energy in three-dimensional systems where typical exciton binding energies are of the order of a few meV. In consequence, excitonic effects are predominant in CNTs already at room temperature [37]. Further, the strong confinement of electron and hole to a small spatial region increases the exciton oscillator strength since this is proportional to the overlap of the electron and hole wave function [103].

When we turn back to the dielectric screening of CNTs in different dielectric media, we can identify that the exciton binding energy decreases when the dielectric constant of the environment is increased (see Eq. 2.22). However, for the PL energy this is overcompensated as also  $E_{BGR}$  is renormalized by Coulomb screening. In sum, the transition energy  $E_X$  was observed to decrease when the dielectric constant of the surrounding medium is increased [104–106]. Assuming an CNT embedded in a dielectric medium with  $\epsilon \rightarrow \infty$ , the Coulomb interaction between electron and hole

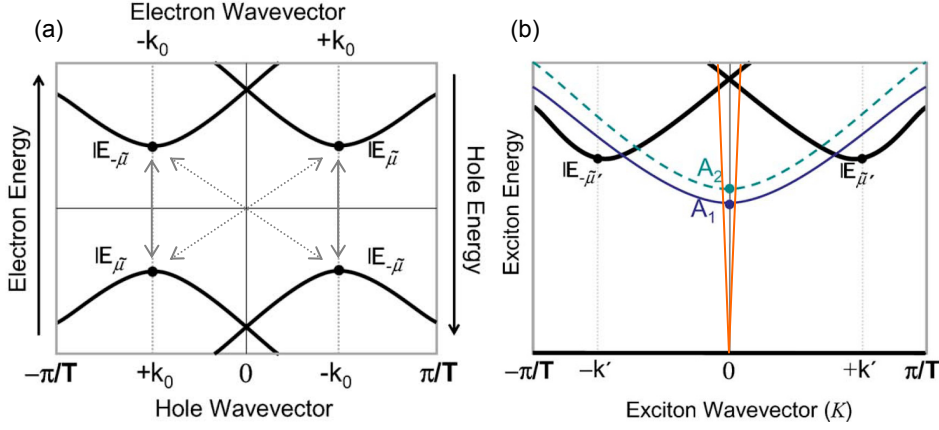


Figure 2.7.: **Electron (a) and exciton (b) states in chiral CNTs:** The states are denoted in the GWV notation. The respective line group notation is given in Tab. 2.1. Four exciton states are identified and their optical selection rules can be easily deduced: The orange solid lines illustrate the dispersion relation of a photon and are not included in the original publication. The anti-symmetric state  $A_2$  ( ${}_0\mathbf{A}_0^-$  in LG notation, bright exciton) does not carry momentum and can couple to light. The symmetric state  $A_1$  ( ${}_0\mathbf{A}_0^+$ , dark exciton) is parity forbidden. The doubly degenerate states  $\mathbb{E}_{\mu'}(k) + \mathbb{E}_{-\mu'}(-k)$  ( ${}_k\mathbf{E}_{\mu}$ ,  $k$ -momentum exciton) carry a finite momentum and are also dark. (Adapted from Ref. [38])

is completely suppressed, which is identical to the one particle picture. Thus, the PL energy equals the difference between the first vHs ( $E_X = E_{11}$ ) [107]. However, experiments showed that the PL energy redshift saturated when the dielectric medium reached  $\epsilon \sim 5$  [106] and did not exceed 49 meV even for  $\epsilon = 37$ .

### 2.3.3. Symmetry of exciton states

To evaluate the symmetry of exciton states we first turn back to the single particle picture one last time. Fig. 2.7 illustrates valence and conduction band in the first Brillouin zone of a CNT. The lowest energy electron (hole) states are located at  $k_0$  and  $-k_0$ , respectively. If we neglect the Coulomb interaction between the electron and the hole, we find four degenerate exciton states - each a combination of a hole at  $\pm k_0$  and an electron at  $\pm k_0$ .

A promising approach to include the Coulomb interaction was reported by Barros et al. [38, 53], which takes advantage of the CNT symmetry (Chap. 2.1.2). Since it identifies the exciton states and their optical activity, it will be briefly summarized here. We will further focus on electrons and holes in the respective lowest energy state ( $E_{11}$ ).

## 2. Theoretical considerations

Exciton	Symmetry		Degeneracy	Activity	$k'$	$\mu'$	$\Pi$
	GWV	LG					
dark, $X^D$	$A_1$	${}_0\mathbf{A}_0^+$	1	dark	0	0	+1
bright, X	$A_2$	${}_0\mathbf{A}_0^-$	1	bright	0	0	-1
k-momentum, $X^K$	$\mathbb{E}_\mu(k) + \mathbb{E}_{-\mu}(-k)$	${}_k\mathbf{E}_{\mu'}$	2	dark	$\pm k'$	$\pm \mu'$	0

Table 2.1.: **Exciton states in chiral carbon nanotubes** in the irreducible representation using group of wave vector (GWV) and line group (LG) notation, the wave vector  $k$ , the circumferential momentum  $\mu$  and their parity  $\Pi$  under rotation of  $180^\circ$  ( $C_2$  rotation). The parity for the k-momentum exciton is not well defined and therefore set to 0. (Adapted from Ref. [38])

The Coulomb force between the electron and the hole depends only on their separation. Applying a symmetry operation keeps therefore the Hamiltonian invariant. Barros et al. obtained solutions of the Hamiltonian (eigenfunctions and eigenenergies) by solving the Bethe-Salpeter equation. Like the Hamiltonian, the exciton eigenstates are also invariant under symmetry operations [38,53]. Each state can be written in its irreducible representation of the line group of the CNT, which we discussed in Chap. 2.1.2. Barros et al. [38,53] expressed the exciton wave function as a linear combination of the electron ( $e$ ) and the hole ( $h$ ) wave function in an envelope  $\mathcal{F}_{\zeta'}(r_e - r_h)$ . In addition, they employed an effective-mass and envelope-function approximation, which yields an exciton wave function

$$\psi^{\text{EMA}}(\vec{r}_e, \vec{r}_h) = \sum_{v,c} B_{vc} \phi_c(\vec{r}_e) \phi_v(\vec{r}_h) \mathcal{F}_{\zeta'}(r_e - r_h). \quad (2.27)$$

Here, the sum runs over all states in the valence ( $v$ ) and conduction ( $c$ ) band, respectively. Although Barros et al. considered the CNT symmetry in a "group of wave vector" (GWV) approach, we will remain with the line group (LG) representation. Tab. 2.1 shows both equivalent notations. The envelope function  $\mathcal{F}_{\zeta'}(r_e - r_h)$  locates the exciton at  $r_e - r_h$ . The index  $\zeta'$  represents the energy levels of the one-dimensional hydrogen atom [108]. We focus on the lowest energy level  $\zeta' = 0$ , so the envelope function is a Gaussian, which is totally symmetric under all symmetry operations. Thus, the irreducible representation of the envelope is given by  ${}_0\mathbf{A}_0^+$ .

To find the irreducible representations of the electron and hole states, we refer to Fig. 2.7(a), which shows the band edges for the valence and the conduction bands. These are doubly degenerate. The minimum energy of electron and hole occurs at the wave vectors  $k = \pm k_0$ . As shown above, their electronic state is represented by the axial momentum  $k$  and the band number  $\mu$ . Neglecting the zone center - so  $k \neq 0$

- their irreducible representation equals  $_{\pm k_0}\mathbf{E}_{\pm\mu}$  (see Chap. 2.1.2). Due to Coulomb interaction these states are mixed to  $(_{k_0}\mathbf{E}_{\mu} + _{-k_0}\mathbf{E}_{-\mu})$  and  $(_{-k_0}\mathbf{E}_{-\mu} + _{k_0}\mathbf{E}_{\mu})$ .

The irreducible representation of the exciton wave function  $\mathcal{D}(\psi^{\text{EMA}})$  is now derived from the direct product of  $\mathcal{D}(F_{\zeta'})$ ,  $\mathcal{D}(\phi_c)$  and  $\mathcal{D}(\phi_v)$ . It results in four excitonic states.

$$\begin{aligned} \mathcal{D}(\phi_c) \otimes \mathcal{D}(\phi_v) \otimes \mathcal{D}(F_{\zeta'}) &= (_{k_0}\mathbf{E}_{\mu} + _{-k_0}\mathbf{E}_{-\mu}) \otimes (_{-k_0}\mathbf{E}_{-\mu} + _{k_0}\mathbf{E}_{\mu}) \otimes {}_0\mathbf{A}_0^+ \\ &= {}_0\mathbf{A}_0^+ + {}_0\mathbf{A}_0^- + {}_{k'}\mathbf{E}_{\mu'} + _{-k'}\mathbf{E}_{-\mu'} \end{aligned} \quad (2.28)$$

The last step included a rescaling of  $\mu$  and  $k$  to  $\mu' = 2\mu$  and  $k' \approx 2k_0$ , respectively.

The two states  ${}_0\mathbf{A}_0^+$  and  ${}_0\mathbf{A}_0^-$  originate from the mixing of single particle states with opposite signs, which are depicted as solid lines in Fig. 2.7(a). Their energy minimum is located at  $k' = 0$  in the center of the Brillouin zone. These states exhibit either odd ( ${}_0\mathbf{A}_0^-$ ) or even parity ( ${}_0\mathbf{A}_0^+$ ). Due to their optical activity they are termed as the *bright* and *dark* exciton. The spectral emission lines are denoted as  $X$  (bright exciton state) and  $X^{\text{D}}$  (dark exciton state).

The doubly degenerate states  ${}_{k'}\mathbf{E}_{\mu'} + _{-k'}\mathbf{E}_{-\mu'}$  originate from the mixing of electron and hole states with the same sign, which are illustrated by the dashed lines in Fig. 2.7(a). Their respective energy minimum is located close to the zone boundary. As these excitons carry a finite momentum  $k'$ , they are denoted as *k-momentum* excitons and their spectral emission line as  $X^{\text{K}}$ .

### 2.3.4. Selection rules for optical transitions

Although the derivation of the four exciton states was a tricky task, their irreducible representation allows us to obtain the selection rules for optical absorption and emission. As mentioned above we consider only light polarized parallel to the tube axis. In addition to the dispersion relation of the four exciton states, Fig. 2.7(b) depicts the dispersion relation of a photon. Obviously, a single photon does not carry enough momentum to create a k-momentum exciton. Neither can a k-momentum exciton decay into a photon without creation of a phonon that would carry the momentum excess. Without providing for sufficient exciton-phonon coupling, the k-momentum exciton states are dark states.

In contrast, the states at the center of the Brillouin zone  ${}_0\mathbf{A}_0^+$  and  ${}_0\mathbf{A}_0^-$  do not carry any momentum. However, due to its even parity  ${}_0\mathbf{A}_0^+$  is dipole forbidden and can not be created or annihilated by a photon of odd parity. This parity forbidden state is therefore denoted as *dark* exciton or  $X^{\text{D}}$ . Finally, the state  ${}_0\mathbf{A}_0^-$  is of odd parity,

## 2. Theoretical considerations

it is therefore neither dipole forbidden nor forbidden by momentum conservation. This is the only bright exciton state and is denoted as the *bright* exciton or  $X$ .

For chiral CNTs all exciton states and their properties are summarized in Tab. 2.1 that was originally published by Barros et al. [38]. In addition to the line group notation (LG) it also includes the group of wave vector (GWV) notation, which is used in Fig. 2.7.

### 2.3.5. Photoluminescence

The emission of photons due to the recombination of an optically excited bound electron-hole-state (exciton) is termed photoluminescence (PL) [37]. The energy of the emitted photon  $E_{\text{PL}}$  is given by the exciton energy  $E_X$  in Eq. 2.24. Due to the laws of energy conservation, the energy of the excitation photon  $\frac{2\pi\hbar c}{\lambda_{\text{exc}}}$  must be at least  $E_X$  or higher. For a given excitation intensity the PL intensity shows resonances whenever the exciton creation is particularly efficient. This is the case for excitation via the second vHs  $E_{22}$  or a phonon sideband [83]. The excited exciton decays non-radiatively to an exciton ground state. Typical timescales for this inter-subband relaxation are  $\sim 40$  fs [109] and exceed the intrinsic life-time of excitons in CNTs (0.1-10 ns) by far [64]. As discussed above, many of the exciton ground states are dark and only the bright exciton state  $X$  ( ${}_0\mathbf{A}_0^-$ ) gives rise to PL emission. Hence, the PL spectrum of an individual CNT shows a single bright emission line at the characteristic energy  $E_{\text{PL}}$  [27].

The experimental observation of the PL was not achieved before CNTs were isolated by the use of a chemical surfactant [24]. Mediated by van-der-Waals forces, CNTs form bundles, in which excitons recombine mostly non-radiatively. The use of surfactants such as tensides or DNA [86] individualizes CNTs and suppresses non-radiative decay. Other non-radiative processes are mediated by defects or singularities in the CNT lattice. For instance the PL intensity of an individual CNT was found to quench in steps whenever a single ad-atom bonds chemically to a CNT lattice site [73]. In general, all processes, that give rise to non-radiative recombination of excitons, are termed Auger processes in the context of CNT optics. If Auger processes (rate  $\gamma_{\text{Auger}}$ ) occur as (or even more) frequent as (than) the exciton radiative decay rate  $\gamma_r$  [69], they shorten severely the exciton life-time  $\tau_0$ , which is given by

$$\tau_0 = \frac{1}{\gamma_{\text{Auger}} + \gamma_r} . \quad (2.29)$$

### 2.3.6. Exciton fine structure

In summary of the theoretical considerations, we now give a general survey of the exciton fine structure. Its experimental observation was in the main focus of spectroscopic investigations of CNTs in the past years [41–43, 45, 47, 49]. In addition to the four singlet exciton states there are further states including spin triplets or (three particle) charged excitons. At the end of this chapter, Fig. 2.8 summarizes the energy splitting between the bright exciton and other (dark) exciton states for many small diameter CNTs.

#### Dark excitons

The lowest energy state of the four singlet exciton states is the dark exciton  $X^D$  ( ${}_0\mathbf{A}_0^+$ ). Capaz et al. estimated the energy splitting  $\Delta_D$  between the bright and the dark exciton state [34]. Their analytical expression for  $\Delta_D$  reads as<sup>9</sup>

$$\Delta_D = \frac{A_D + B_D\xi + C_D d_t \xi^2}{d_t^2} . \quad (2.30)$$

The leading term of the dark-bright splitting scales as the inverse diameter squared  $\sim 1/d_t^2$ . We evaluated  $\Delta_D$  for all CNTs with small diameters and summarized them in Fig. 2.6. Distinct family patterns are highlighted by solid lines, which interconnect tubes belonging to the same family  $2n + m$ .

As discussed before in Chap. 2.3.4, the lowest singlet exciton state is dark because of its even parity. However, a magnetic field applied parallel to the CNT axis lifts the valley degeneracy (see one particle considerations in Fig. 2.7(a)), which mixes the dark and bright exciton state. In addition to the bright exciton, also the dark exciton is predicted to be optically-active in the presence of a magnetic flux [110]. Successful experimental procedures of brightening the dark exciton have been reported [43, 111].

		$\Delta_D$	$\Delta_K$
9	$A_i$	18.425 meV nm <sup>2</sup>	13.907 meV nm <sup>2</sup>
	$B_i$	12.481 meV nm <sup>3</sup>	-5.016 meV nm <sup>3</sup>
	$C_i$	-0.715 meV nm <sup>3</sup>	-1.861 meV nm <sup>3</sup>

From an experimentalist point of view it is reasonable to write the energy splittings with respect to the bright exciton. Thus, the parameters for the k-momentum splitting  $\Delta_K$  vary from those given in the original publication, that presented a  $\Delta_K$  with respect to the lowest dark singlet-exciton state [34].

## 2. Theoretical considerations

### k-momentum exciton

Capaz et al. also give an analytical expression for the splitting  $\Delta_K$  between the bright and the k-momentum exciton. This expression is of the same form as Eq. (2.30) but different parameters ( $A_K, B_K$ , and  $C_K^g$ ). Accordingly,  $1/d_t^2$  is also the leading term in  $\Delta_K$ .

Due to its finite momentum, the k-momentum exciton can not decay into a photon without validating momentum conservation principle. However, exciton-phonon coupling [80] mediates the creation (annihilation) of an exciton and a phonon by absorption (emission) of a single photon. The phonon sidebands around the k-momentum exciton are at  $\pm\hbar\omega_{\text{ph}}$ . Here,  $\hbar\omega_{\text{ph}}$  denotes the energy of the created or annihilated phonon, which equals approximately 160 meV. With respect to the bright exciton the sidebands are split by  $\Delta_K \pm \hbar\omega_{\text{ph}}$  and were observed experimentally in both the absorption and the emission spectra of CNTs [42].

### Triplet exciton

Additional exciton states with energies below the dark exciton arise from the mixing of electron and hole spins. Considering the total spin  $s$  of electron and hole, each of the above identified four exciton states splits in four spin states: one singlet state ( $s = 0$ ) and three triplet states ( $s = 1$ ). As all triplet states carry a net spin, their optical decay is spin forbidden. Therefore all triplet states - including the triplet counterparts of the bright exciton - are dark states. Nevertheless, they play an important role in the life-time of bright excitons since there is a strong relation between optical inactivity and the exchange energy [64].

Theoretical values for the splitting between the bright exciton singlet and its triplet counterpart  $\Delta_{\text{ST}}$  were reported by Capaz et al. [55]. However, their report did not include an analytical expression like for the splitting between the four singlet states (Eq. 2.30). Within acceptable error limits we were able to extract the explicit values  $\Delta_{\text{ST}}$  for many chiralities from their report using image processing. These values are summarized in Appendix B. For vacuum condition the splitting scales roughly with  $(80 \text{ meV nm})/d_t$ .

Direct emission from triplet exciton states has been observed in single CNT spectroscopy. To this end the symmetry of a CNT must be broken either by treatment with intense laser pulses [45] or by chemical adsorption of hydrogen atoms [112]. The broken symmetry gives rise to spin flip processes that allow the emission from this otherwise dipole forbidden state.

### Trion exciton

A trion is a many-particle bound state either consisting either of two holes and one electron ( $X^+$ ) or one hole and two electrons ( $X^-$ ). Due to the excess of one charge it is also denoted as a charged exciton. For many reasons the trion is of special interest. As a charged quasi-particle it could be controlled by external gates. Furthermore, its net spin of  $1/2$  could open the door to investigation of spin physics in CNTs. This could be further facilitated by its energy splitting between the bright and the charged exciton  $\Delta_{\pm}$  that exceeds by far values known from charged excitons in other nano-scaled emitters, e.g. quantum dots. We will briefly discuss the origin of this splitting, which is given by

$$\Delta_{\pm} = \Delta_{\text{ST}} + S^{\pm} \quad (2.31)$$

that is the sum of the singlet-triplet splitting of the uncharged exciton and the binding energy  $S^{\pm}$  for an excess electron ( $-$ ) or hole ( $+$ ). Here, we focus on the "singlet trion state" where the binding energies for an additional hole or electron are almost identical. In vacuum ( $\epsilon = 1.846$ ) the binding energy scales roughly with  $(100 \text{ meV nm})/d_t$ . Within the here discussed experimental results we cannot distinguish whether a trion is positively or negatively charged. Thus, trion emission lines will be generally termed as  $X^{\pm}$ . The explicit numbers for positively and negatively charged singlet and triplet trions have been reported by Rønnow et al. [81] and are summarized in Appendix B.

Under high excitation power signatures of the emission from trion states was observed [49] but also the effectiveness of chemical doping was reported recently [47,50]. Also re-normalization of the CNT band gap by doping with oxygen creates low-energetic satellite peaks. The energy splitting between these satellites and the bright exciton is consistent with the formation of a trion [48,51].

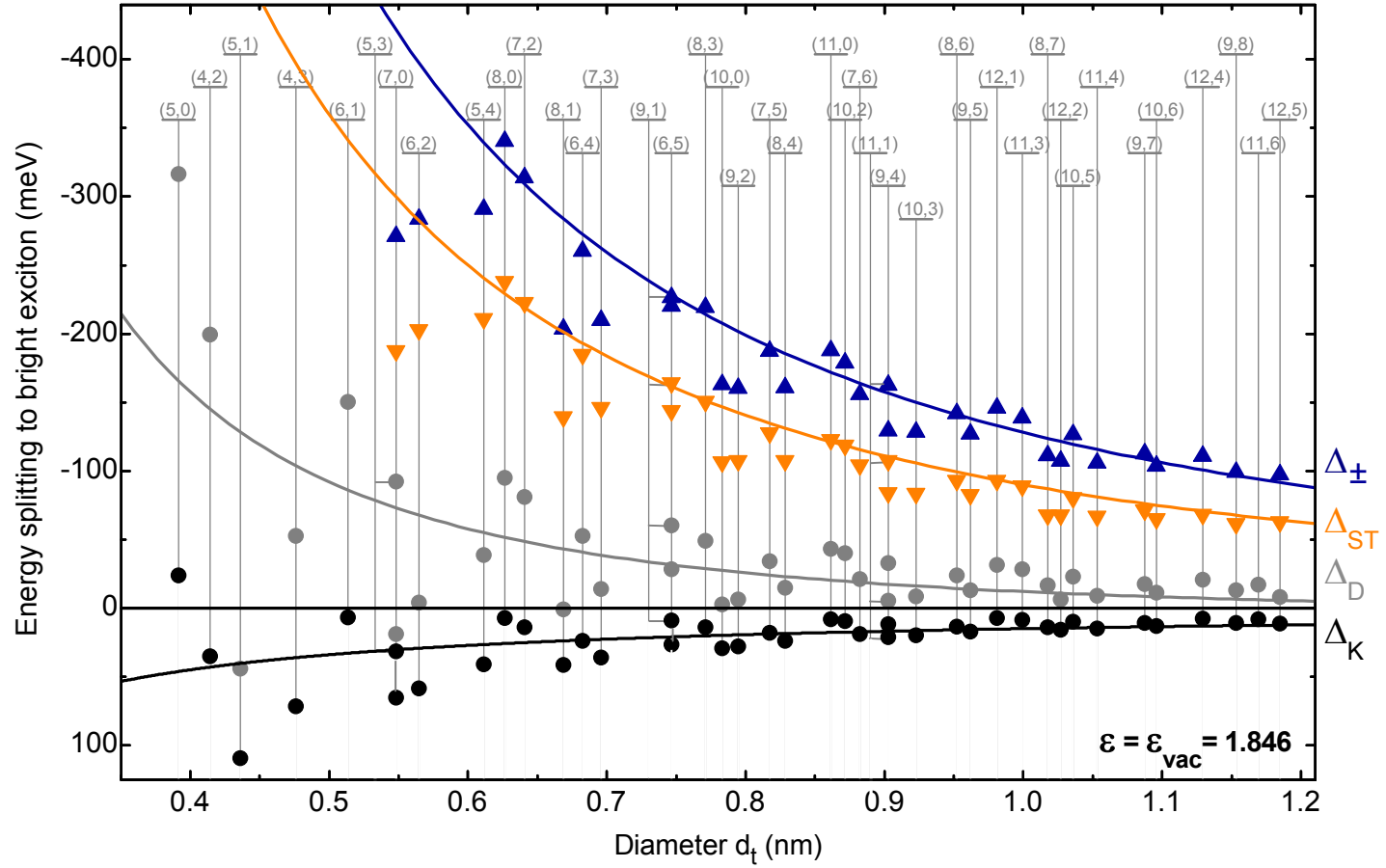


Figure 2.8.: **Energy splittings to the bright exciton** calculated for vacuum conditions ( $\epsilon = 1.846$ ). The energy splitting to the bright exciton state are shown for many small-diameter chiralities (grey numbers). Splitting to k-momentum exciton  $\Delta_K$  black circles, to dark exciton  $\Delta_D$  in grey circles, to the triplet state  $\Delta_{ST}$  in orange triangles, and to the trion state  $\Delta_{\pm}$  in blue triangles.

### 3. Photoluminescence of individual carbon nanotubes

Reliable methods of identifying and imaging CNTs are crucial for sample fabrication intended for optical spectroscopy of individual CNTs. Here we investigated commercial CoMoCat CNTs [113] with well established values of diameter and chirality distribution [114] by applying three complementary imaging techniques: scanning electron microscopy, atomic force microscopy and confocal photoluminescence microscopy at cryogenic temperatures. Lithographically defined metallic markers on a Si-SiO<sub>2</sub>-substrate allowed a comparative study, in which we imaged sequentially specific regions of a layer of dispersed individual CNTs with all three methods. Exploiting the complementary advantages of these imaging techniques we have developed a systematic characterization routine of CNT samples that lays the foundation for the construction of advanced CNT samples.

In addition to controlling the distribution of CNT length, diameter, and density, samples with metallic markers allowed to record PL spectra at various temperatures. Such spectra revealed characteristic features of the PL of individual CNTs: asymmetric line shapes at cryogenic temperatures [59, 60] and shifts in the PL energy when the sample temperature was increased. Both effects can be interpreted as arising from the localization of excitons in cryogenic CNTs.

### 3.1. Laser setup and confocal microscope

The experimental apparatus consisted of a confocal microscope, which could be operated at cryogenic temperature, and a sample, which accommodated individualized CNTs. The following section gives an overview on the microscopy setup whereas various sample layouts, methods for processing, and characterization are discussed separately in the respective chapters (3.2, 4.1, 5.3). Excited by a laser beam, which was controlled in color, wavelength, and intensity, spectroscopy of individual CNTs was carried out with use of a confocal microscope. This positioned individual CNTs in the focus of this laser beam and collecting emitted PL light. This light was analyzed using different detection devices, which allowed to quantify the PL wavelength and intensity, but also to resolve PL dynamics or to correlate emission events. As similar microscopy setups were documented explicitly [91, 115–117], most of it is only briefly presented here. The main focus lies on the table top laser setup outputting an excitation beam with a well defined wavelength, polarization, and intensity. The layout and performance of devices used for time resolved measurements are documented in Chap. 5.2.2.

#### 3.1.1. Confocal microscope

The layout of the employed confocal microscope is sketched in Fig. 3.1. The upper part consisted of two arms: First, the horizontal excitation arm (black beam line), which collimated the excitation laser beam from a single-mode fiber (SM<sup>1</sup>) at the fiber coupler FC<sup>2</sup>; secondly, the upright detection arm (orange beam line) that coupled the collected light into a single-mode fiber guiding to a detection devices. Both fibers acted like pinholes or spatial filters ensuring point illumination and detection. The microscope objective consisted of a single lens<sup>3</sup> (L) with a numerical aperture NA= 0.68. We compensated for the chromatic aberration of the objective by (fine-)adjustment of the excitation beam collimation. This ensured the identical focal plane for excitation (low wavelength) and detection (high wavelength) beam paths. As shown below, this compensation reduced the optical resolution only slightly.

A pair of opposing long- and short-pass filters (SP, LP<sup>4</sup>) suppressed the excitation light by more than  $10^{-12}$  in the detection arm. We controlled the polarization

---

<sup>1</sup>by Diamond GmbH

<sup>2</sup>Lens C220TME-B by Thorlabs

<sup>3</sup>C330TME-B by Thorlabs

<sup>4</sup>AELP900, AESP900, AELP860, AELP860 by OmegaOptical Inc. Brattleboro, VT, USA

### 3.1. Laser setup and confocal microscope

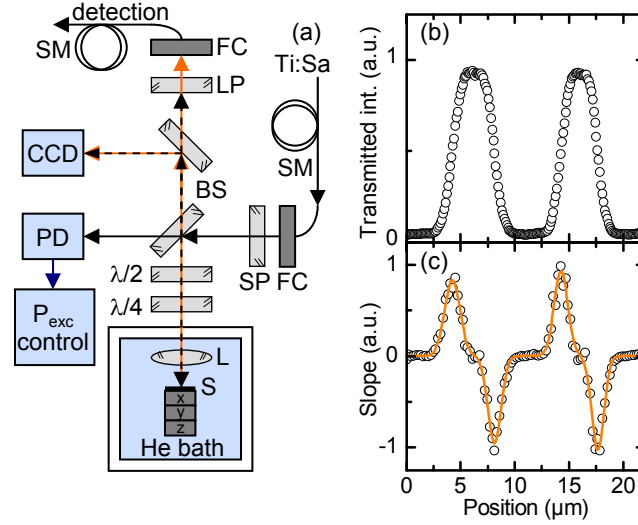


Figure 3.1.: **Confocal microscope setup:** (a) Schematic microscopy setup. (b) Intensity transmitted through a grating in the focal plane as a function of its position. (c) Differential transmission intensity as a function of the grating position (open circles). The solid line represents a fit of four convoluted Gaussian peaks indicating a beam diameter of 1.1  $\mu\text{m}$ .

of the excitation beam using a half-wave-plate ( $\lambda/2$ ) and an additional, removable quarter-wave-plate ( $\lambda/4$ ) for circular polarization. The latter was employed for pre-experiments only.

The sample was mounted on a piezo-based positioning stack<sup>5</sup>, which positioned the sample with respect to the focal spot along all three dimensions using finite steps of displacement. An additional scanner<sup>6</sup> allowed continuous positioning in the focal plane, which we employed particularly for recording of spatially resolved maps (see Chap. 3.3). A photodiode<sup>7</sup> beneath the sample measured the transmitted intensity. For cryogenic operation the microscope's lower part (positioner, sample and objective lens) was cladded in a tube, evacuated, and positioned in a bath cryostat<sup>8</sup>. Helium exchange gas (pressure 20 mbar at room temperature) coupled the sample thermally to the coolant bath. Depending on the desired temperature  $T$  of 4.2 or 77 K, this coolant was either liquid helium or liquid nitrogen, respectively.

The optical resolution of a confocal microscope is given by the size of the focal spot [115]. We evaluated the spot size with a grating (periodicity  $10\mu\text{m}$ ) placed in

<sup>5</sup> ANPx/z-100/101 by attocube systems AG, München, Germany

<sup>6</sup> ANSxy100 by attocube systems AG, München, Germany

<sup>7</sup> BPW 34 by Siemens

<sup>8</sup> Supercompact Cryomagnetic System customized by Cryogenic Consultant Limited, Nottingham, United Kingdom

### 3. Photoluminescence of individual carbon nanotubes

the focal plane of a 960 nm laser beam. The grating was shifted laterally in perpendicular direction to its grating pattern through the focal spot while recording the transmitted intensity as a function of the grating position as depicted in Fig. 3.1(b). The transmitted intensity is given by the convolution of the Gaussian beam profile and a sum of rectangular functions representing the grating pattern. Differentiating the intensity curve with respect to the grating position eliminates these rectangular functions in favor of delta peaks located at every grating edge. In contrast, the Gaussian beam profile is not affected by this differential operation. The curve of the differential transmission intensity is shown in Fig. 3.1(b). Fitting the width of the (here four) convoluted Gaussian peaks gives the diameter (=full width half maximum) of the focal spot. Routinely, we found a focal spot diameter of about 1  $\mu\text{m}$  close to the diffraction limit of  $\lambda/2 \cdot \text{NA}$ .

#### 3.1.2. Laser power stabilization

The coherent light source for the excitation beam in all our experiments was a titan sapphire laser system (Ti:Sa<sup>9</sup>) pumped by a diode laser<sup>10</sup>. It operated either in continuous wave (cw) or pulsed mode. In pulsed mode the laser emitted a sequence of  $\sim 200$  fs short pulses with a repetition rate of 76.0 MHz. In both modes the output wavelength was tunable over a wide range from 700 to 980 nm by rotating a micrometer screw. By mechanically coupling this screw to a stepping motor<sup>11</sup> the wavelength was controlled electronically via a central LabView routine. The current wavelength was measured with a resolution of  $\sim 1.5$  nm by an auxiliary spectrometer<sup>12</sup> from a side arm beam and recorded by the LabView routine.

However, the laser output intensity varied over several orders of magnitude whenever the wavelength is detuned. And even for a constant wavelength it fluctuated  $\sim \pm 3$  % due to thermal drift of the laser resonator and other intensity fluctuations. Hence, we employed the following stabilization setup that largely decoupled the beam intensity from the chosen wavelength and further suppressed temporary intensity fluctuations and long-term drifts.

Its central part was an acousto-optic modulator<sup>13</sup> (AOM). Inside such an AOM, an acoustic wave is induced into a quartz Bragg cell by an attached piezo-electrical transducer, which is usually driven by a radio-frequency resonator (here 80 MHz). The

---

<sup>9</sup>Mira 900 by Coherent

<sup>10</sup>Verdi V-10 by Coherent

<sup>11</sup>PD4-K by NanoTec Electronics GmbH, Landsham, Germany

<sup>12</sup>USB4000-VIS-NIR by OceanOptics

<sup>13</sup>AOM 3080-125 by Crystal Technology Inc.

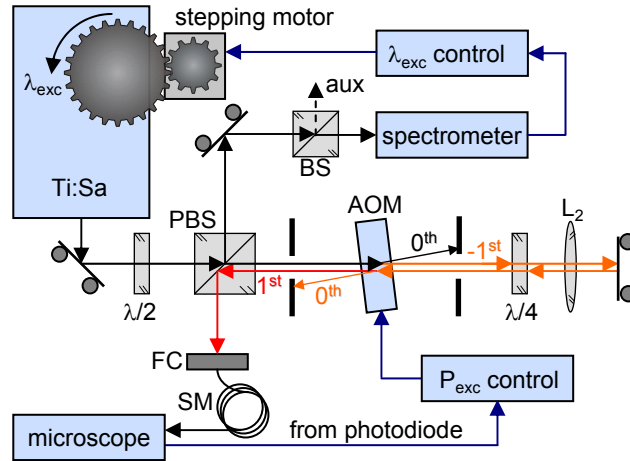


Figure 3.2.: **Laser beam line:** A LabView routine controlled electronically the wavelength of the titan-sapphire laser system via a stepping motor. The laser beam double-passed through an acousto-optical modulator (AOM) that allowed to stabilize and control the laser power by adjusting the driving amplitude of the AOM.

acoustic wave comes along with periodic modulation of the quartz' refractive index giving rise to Brillouin scattering of light. The intensity of the respective diffraction order is conditioned by the amplitude of the acoustic driving signal. Hence, the intensity of a diffracted beam is a function of the input power from the driving resonator and can be controlled easily via a voltage input.

As depicted in Fig. 3.2, we used a double pass layout [118]. Since the diffraction angle is a function of the beam wavelength, a single pass layout would result in a tilt whenever the wavelength is varied. That can be compensated for by passing the beam twice in opposing orders of diffraction. The net tilt adds up to zero regardless of the beam wavelength. Within our setup, a lens (L) focused the beam on a reflecting mirror and provided for the re-collimated beam being parallel to the incident beam regardless of tilt angle. In each pass an order selecting aperture filtered other orders of diffraction.

In addition, the linearly polarized beam passed twice through a quarter-wave-plate. After the first transition it was circularly polarized and after the second transition linearly polarized - however now rotated by  $90^\circ$  and hence reflected by the polarizing beam splitter (PBS). Coupled into a single-mode fiber (SM) the light was guided to the microscope. A reference photodiode (depicted in Fig. 3.1) monitored the current laser intensity in the microscope. A home-built proportional-integral-derivative

### 3. Photoluminescence of individual carbon nanotubes

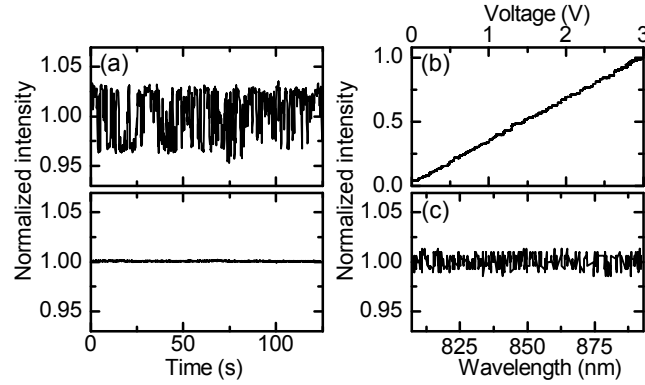


Figure 3.3.: **Performance characteristics of the stabilized laser setup:** (a) Time trace of laser intensity at constant wavelength measured in the confocal microscopy without laser stabilization (upper panel) and with laser stabilization (lower panel) showing a reduction of intensity fluctuations below 0.1%. (b) The laser power was linearly controlled by an external d.c. voltage over two orders of magnitudes. (c) Laser intensity as a function of the laser wavelength showing small fluctuations below 0.7% even when the Ti:Sa laser was tuned over a wide spectral range.

(PID<sup>14</sup>) controller compared the actual intensity with a reference given by an external dc voltage. By altering the AOM driver output the PID controller readjusted the beam intensity to the reference. As the bandwidth of the PID controller and the reference photodiode were below the Ti:Sa repetition rate, the stabilization worked for both continuous and pulsed laser operation.

The performance of this setup is illustrated in Fig. 3.3. Whereas a non-stabilized beam fluctuated up to  $\pm 2.7\%$ , the stabilization setup reduced fluctuations below  $\pm 0.1\%$  of the overall intensity for constant wavelength. Furthermore, it allowed the control of the beam intensity by setting a dc voltage via the central LabView routine. The laser wavelength was controlled without any readjustments in a range of  $\sim 100$  nm by the same LabView routine. Within such a spectral range the beam intensity was constant to within  $\pm 0.7\%$  of the overall intensity as depicted in Fig. 3.3(c). The here presented trace was taken from an eight hour measurement and demonstrates the long-term stability of the power stabilization setup.

The reference diode as well as the diode used for detecting the intensities in Fig. 3.3 were silicon based photodiodes of the same type<sup>15</sup>. However, the traces presented here do not account for their wavelength dependent sensitivity that is typically fea-

<sup>14</sup>Home-build device with a bandwidth of 0 – 3 kHz. We thank Stephan Manus for his effort on construction of this device.

<sup>15</sup>Both BPW34 by Siemens

tured by semiconductor photodiodes. Nevertheless, in a wide range between 780 and 980 nm the sensitivity of the used photodiodes is reported to vary less than 10 % [119].

### Detection devices

We analyzed the collected PL light either spectrally or time-resolved. For recording of PL spectra we used a commercial spectrometer<sup>16</sup>, which dispersed the PL light with a monochromating grating and imaged on a liquid-nitrogen-cooled CCD. Depending on the used grating of either 300 or 1200 grooves per mm, we reached a spectral resolution of 220  $\mu\text{eV}$  and 40  $\mu\text{eV}$ , respectively. Since layout and performance of this spectrometer was reported in detail before [91, 116, 117], it will not be elaborated here. Devices used for time-resolved measurements, e.g. an Hanbury-Brown-and-Twiss interferometer, are presented in Chap. 5.2.2.

## 3.2. Sample preparation and characteristics

This work considers three different sample layouts, which provide the CNT with different dielectric environments and differ in the fundamental method of CNT processing. Either, the CNTs were commercially available, grown with the use of a cobalt-molybdenum catalyst (CoMoCat CNTs). Or, they were home-grown in a chemical-vapor-deposition process with the use of an iron-ruthenium catalyst (CVD CNTs). Also, CNTs in these samples are either freely suspended in vacuum or embedded in a dielectric medium. And finally, we introduce an external parameter - an electric field perpendicular to the CNT axes - to probe for exciton localization, to determine the perpendicular polarizability of excitons in CNTs, and to switch charge

<sup>16</sup>Acton SP2500 by Princeton Instruments

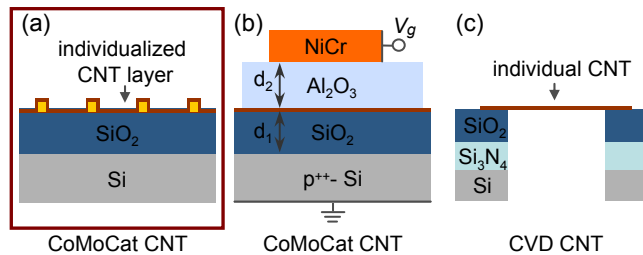


Figure 3.4.: **Sample layouts I:** CoMoCat CNTs on a silicon oxide surface, which features a metallic grid (a). CoMoCat CNTs embedded in an electric gate device (b). CVD CNT freely suspended over a crater (c).

### 3. Photoluminescence of individual carbon nanotubes

states localized in the dielectric medium. In detail, these layouts are illustrated in Fig. 3.4. In this chapter, we focus on the first layout depicted in (a). We studied commercially available CoMoCat CNTs on a Si-SiO<sub>2</sub>-substrate, which featured a lithographically defined metallic grid.

#### 3.2.1. Metallic grid

As a first step, we defined a grid on an Si-SiO<sub>2</sub>-substrate. This grid allowed to trace the respective position of individual CNTs at various temperatures in the confocal microscopy setup. Furthermore, it enabled the complementary imaging of the same sample section in different imaging devices, e.g. a scanning electron microscope or an atomic force microscope. The grid consisted of lithographically defined gold markers each sized  $\sim 1 \mu\text{m}$ . These markers partitioned parts of the sample surface in  $10 \times 10 \mu\text{m}^2$  squares each confined by four markers located in the square corner. The detailed layout is reported in [91] and [117].

#### 3.2.2. CoMoCat material

As a basic source for CoMoCat CNTs we used a commercially available aqueous CoMoCat CNT solution<sup>17</sup>, in which the CNTs were dissolved and individualized by a sodium-cholate (SC) surfactant. Since the CoMoCat method favors the outcome of certain semiconducting chiralities - namely (6,5) and (7,5) as well as those with similar diameters -, around 95% of these CNTs show photoluminescence in the near-infrared spectral range [114]. The detailed recipe for processing a layer of mostly individualized CNTs on a substrate is documented in Appendix C of this thesis. In brief, the CNT solution (with an initial density of 1g CNT/l) was diluted in an aqueous SC solution<sup>18</sup> and spun on a cleaned silicon substrate, which was prepared with a metallic grid as necessary. The density of CNTs on the surface was controlled via the mixing ratio of the CNT solution and the SC solution. It was typically adjusted to less than one CNT per  $\mu\text{m}^2$ . This allowed for individual optical access with the confocal microscope with a spatial resolution of  $\sim 1 \mu\text{m}$ .

### 3.3. Spatially resolving imaging techniques

Since it featured a metallic grid, the presented sample design enabled us to retrace the exact position of a small sample section. First, the grid allowed to record effec-

<sup>17</sup>SG65 by SouthWest NanoTechnologies, Inc., Norman, OK, USA

<sup>18</sup>Cholic acid sodium hydrates by Sigma-Aldrich Corp.

### 3.3. Spatially resolving imaging techniques

tively the PL spectra of individual CNTs at different temperatures, which is focus of the next Chap. 3.5. Secondly, the grid enabled us to investigate a section using different imaging techniques. Evaluating the respective detection effectiveness of each imaging technique is a prerequisite, when layers of individualized CNTs need to be characterized. Since each imaging technique features unique advantages, they were employed collectively to control and adjust the parameters for processing layers of individualized CNTs (see previous section 3.2). Thereby, we were able to characterize layers of individualized CNTs with respect to CNT density (using scanning electron microscopy and atomic force microscopy), with respect to optical properties (using photoluminescence microscopy), and with respect to the formation of bundles, which is mediated by strong van-der-Waals interaction between CNTs (using atomic force microscopy).

Scanning electron microscopy (SEM) provides for fast imaging of large sample areas with a medium resolution of  $\sim 40$  nm. Although this resolution exceeds the diameter of CNTs ( $\sim 1$  nm), we were able to record a detectable contrast between CNTs and the Si-SiO<sub>2</sub>-substrate using a commercially available scanning electron microscope<sup>19</sup> operated with an acceleration voltage of 0.7 kV. In fact, SEM overestimated the CNT diameters by far, but resolved many CNTs in large sample sections ( $\sim 100\mu\text{m}^2$ ) during a recording time of a few seconds. However, the scanning electron beam deposits carbon from the ambient residual gas in the microscope chamber. This deposition gives rise to excessive non-radiative recombination of excitons and thus quenches all PL. Therefore, we employed SEM only in post-PL imaging and to adjust the mixing ration of the CNT solutions resulting in a desired CNT density.

Atomic force microscopy (AFM) is a high resolving imaging technique featuring a height resolution below 1 nm. Thus, it allows to estimate the diameter of individual CNTs without drawbacks on their optical properties. We used a commercially available atomic force microscope<sup>20</sup> in tapping mode and scanned typically sections of  $2 \times 2\mu\text{m}^2$  with a lateral resolution of 512 pixels in 216 lines. Due to the precise height resolution we assume that all CNTs in a section could be detected with AFM imaging. Although AFM is in principle capable of resolving down to the atomic scale, the use of an unspecified tip precluded to determine the exact diameter of individual CNTs that were furthermore wrapped in the SC surfactant. Indeed, AFM enabled us to distinguish between a single CNT and a CNT bundle, but kept us uncertain about the chirality of a specific CNT. Further, this technique is very time

---

<sup>19</sup>eLine by Raith GmbH, Germany

<sup>20</sup>Nanoscope 3100 by Digital Instruments now Bruker Corporation MA, USA

### 3. Photoluminescence of individual carbon nanotubes

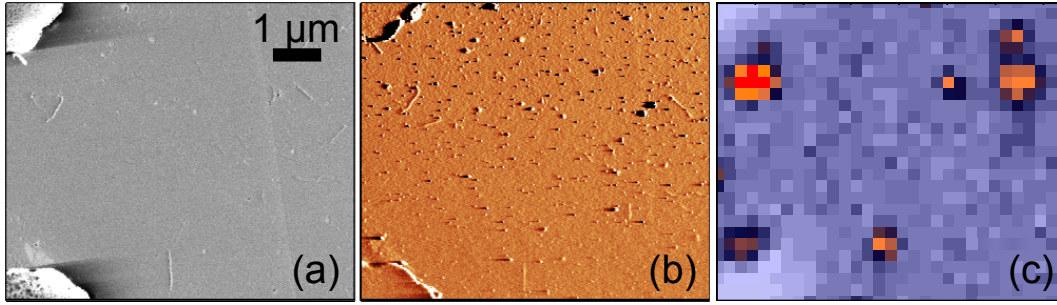


Figure 3.5.: **Complementary imaging** of the same sample area of  $10 \times 10 \mu\text{m}^2$  using (a) scanning electron microscopy, (b) atomic force microscopy, and (c) spatially resolved PL microscopy.

consuming. For instance, recording of the section depicted in Fig. 3.5(b) took more than 7 hours. We used AFM routinely to check in spot tests layers of individualized CNTs with respect to CNT density and formation of CNT bundles. In addition, AFM allowed to adjust the mixing ratio of the SC surfactant in the CNT solution.

Spatially resolved PL microscopy was accessible with our microscopy setup at various temperatures ( $T = 300 \text{ K}$ ,  $77 \text{ K}$ ,  $4.2 \text{ K}$ ). To record a spatially resolved map a sample section was scanned point by point while recording a spectrum at every coordinate point with a fixed excitation wavelength, intensity and (circular) polarization. Reproducible positioning of the sample was facilitated by the use of the lateral scanning unit (see Chap. 3.1.1). In contrast to the stepping units, it continuously positioned the sample with reference to an external voltage. In this scheme, hysteresis effects and long term drifts were kept well below the spatial resolution of the confocal microscope [120]. We set the distance between two coordinate points typically with  $0.5 \mu\text{m}$ , which was half of the microscope resolution of  $1 \mu\text{m}$ . Although this technique is time consuming, it reveals the optical properties of the CNTs located in the sample section. In contrast to the other imaging techniques, spatially resolved PL microscopy reveals only CNTs that show PL in a limited spectral range. Many others stay dark, like metallic CNTs, CNTs with a too low (big) band gap, or CNTs with quenched PL emission.

The diploma thesis of M. Hofmann included a detailed comparative study [91], which revealed the effectiveness of these imaging techniques. Samples with a metallic grid allowed to record the same sample sections with all three imaging technique. Exemplarily, a  $10 \times 10 \mu\text{m}^2$  sized section is shown in Fig. 3.5. The bright patterns in the left corners are part of the metallic grid. The SEM image, which is depicted in Fig. 3.5(a), features individual CNTs as white lines. The similarity to the AFM

### 3.4. Signatures of individual CoMoCat CNTs

image (b) is particularly apparent for the triangle constellation of three CNTs below the upper metallic pattern on the left image border and for the single long tube in the middle slightly above the lower image border. Compared to the PL map taken at  $T = 4.2$  K both areas showed also bright PL intensity.

Due to its outstanding height resolution, AFM images can be taken as a reference for the total number of CNTs located in a sample section. By comparison with the other imaging techniques we find that approximately 80% of the CNTs showed a detectable contrast to the substrate in SEM images. Around 70% of the CNTs showed PL in the spectral range (900-1020 nm). This is in good agreement with the estimated share of 95% semiconducting CNTs resulting from the CoMoCat growth process<sup>21</sup>. However, the PL emission of some of these CNTs was not included in the observed spectral range - as is the case for the (7,6) chirality, which typically emits at 1120 nm [88] and makes up around  $\sim 10\%$  of all CoMoCat CNTs [114].

In summary, we have established a procedure to form a layer of individualized CNTs on a Si-SiO<sub>2</sub> substrate. The use of complementary imaging techniques allowed us to adjust effectively the mixing ratios for the CNT solution and other processing parameters. The density of CNTs was well-adjusted to ensure exclusive access to individual CNTs with a confocal microscope, whose spatial resolution was close to the diffraction limit. This lays the foundation for optical spectroscopy of individual CNTs.

### 3.4. Signatures of individual CoMoCat CNTs

The PL of individual CNTs was first reported independently by Lefebvre et al. [27] and Hartschuh et al. [26]. They revealed several signatures of individual CNTs that differ from those of CNT ensembles: Namely, single (asymmetric) emission peak at cryogenic temperature and highly polarization dependent absorption and emission due to the antenna effect (see Chap. 2.2.3).

Whenever we scanned the sample laterally for searching individual CNTs, we used a circularly polarized, cw excitation beam while shifting the sample through the focal spot in lateral steps with the piezo positioners. However, we had only limited information about the present microscopic formation of CNTs in the focal spot. Unless we would employ other imaging techniques, much remained unclear like the exact number of CNTs, whether these formed bundles or whether they were metallic or semiconducting with unfitting band gap or quenched PL. However, we could rule

---

<sup>21</sup>Compare to data sheet of SG65 CNTs or Ref. [114].

### 3. Photoluminescence of individual carbon nanotubes

out these objection by processing properly the layer of individualized CNTs. This included the use of a SC surfactant that individualized the CoMoCat CNTs and prevented them from forming bundles [104]. Plus, we adjusted the density on the substrate below one tube per  $\mu\text{m}^2$ . In addition, we focussed on sample sites, which showed unambiguous spectral PL response as we will discuss here and in Chap. 4.4. The spectral range of interest was limited by the used long-pass filter and by the chromatic aberration of the confocal microscope that narrowed the range to  $\sim 50$  nm. Thus, our view was respectively concentrated on a few CNT chiralities<sup>22</sup> that emit within this range (see Kataura plot Fig. 2.5).

As exemplified in Fig. 3.6(b), we found single emission peaks, whose intensity typically exceeded other background emission (that consisted of Raman emission from the CNT but dominantly from the silicon substrate) by at least a factor of 100. These were laterally confined and intensified particularly when the sample was positioned vertically in the focal plane. The background was mostly composed of a characteristic Raman signal that we assigned to originate from the silicon substrate. This signal was observed independently from the lateral position and, in contrast to CNT PL signals, was also very robust against variations of the sample's vertical positioning to the focal plane. At cryogenic temperature ( $T=4.2$  K) the recorded PL peaks were predominantly asymmetric with a steep edge on the high-energy side and a smoother fall to low energy. Fitting a Lorentzian peak showed good agreement

<sup>22</sup>Namely, in the range from 860 to 1000 nm PL emission is expected from the chiralities (6,2), (6,4), (6,5), (7,0), (7,3), (8,3) and (9,1). Their diameter varies from 0.56 to 0.78 nm.

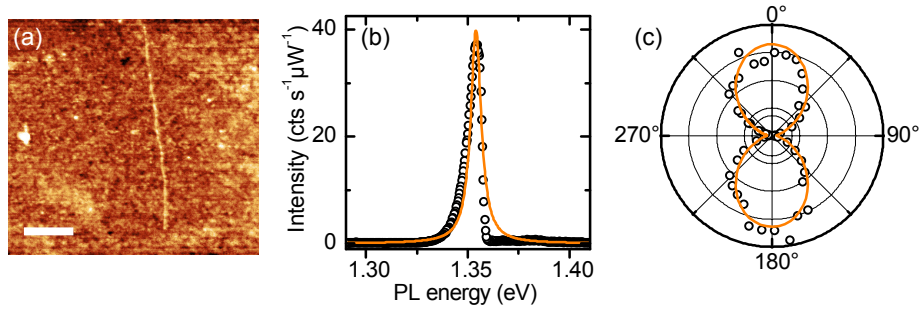


Figure 3.6.: **Photoluminescence of a single carbon nanotube:** (a) A single CNT imaged by AFM. The scale bar measures 500 nm. (b) Excited continuously by a linearly polarized laser beam with  $\lambda_{\text{exc}} = 845$  nm an individual CNT shows a single asymmetric emission line. Whereas a Lorentzian peak (solid line) is unable to reproduce the emission peak's asymmetry it gives reliable measures of the central PL energy and the peak width. (c) Normalized PL intensity (radial degree on a linear scale) as a function of the linear polarization angle  $\zeta$  (relative to the CNT axis). The solid line displays a  $\cos^2$  fit.

with the low-energy edge, but did not reproduce the high-energy slope. Nevertheless, it provided a reliable measure for the PL central energy  $E_{\text{PL}}$ , the peak width  $\Gamma$  and the PL intensity  $I$ . For investigation of the asymmetry we split a PL peak around the central PL energy into two halves, which can be each reproduced by an halved Lorentzian peak. This procedure is discussed in the following Chap. 3.5.

Further, individual CNTs showed a pronounced antenna effect with a high aspect ratio ( $\sim 50 : 1$ ) between intense emission for the excitation polarization being parallel to the tube axis and vanishing PL emission for perpendicular excitation. As depicted by the solid line in Fig. 3.6(b) the intensity followed a  $\cos^2 \zeta$ , where  $\zeta$  denotes the angle between excitation polarization axis and the tube axis.

A definite proof that an emission site is due to an individual CNT can only be shown by the detailed analysis of its photon statistic. As we will discuss in Chap. 5, we have successfully performed such measurements on substrate supported CNTs. Without any exception, all of them showed photon anti-bunching, which excluded the presence of a second (identical) CNT in the focal spot.

In summary, samples with layers of individualized CNTs, which we controlled effectively by complementary imaging techniques, showed clear evidence of PL from individual CNTs (single asymmetric peaks, antenna effect, photon anti-bunching). As a synopsis of the here presented experimental results, interaction of an individual CNT with neighboring CNTs (like in bundles) can be regarded as precluded.

### 3.5. Exciton localization at low temperatures

Whereas the previous considerations focussed merely on methods for processing and characterizing layers of individualized CNTs, we now turn to the optical properties of individual CNTs at various temperatures. Previously reported experiments [60, 76, 121] traced the PL signal of only a single individual CNT while changing the temperature. Thus, the sample must be cooled-down and warmed repetitively to achieve a significant number of spectra from several individual CNTs. However, every change of temperature includes the risk that the sample might detach from the piezo positioners or that the piezo positioners freeze. In contrast, samples with metallic grids enabled us to record a number of PL maps at 4.2 K and then repeated this at 77 K and 300 K, which required only one temperature iteration. In analysis of these maps, we concentrated on sites, which showed a single asymmetric emission line at 4.2 K. Fig. 3.7(a) illustrates the main characteristics of a PL spectrum recorded

### 3. Photoluminescence of individual carbon nanotubes

at various temperatures: a broadening of the line width towards a symmetric line shape and a shift of the central PL emission energy [60].

As we will discuss now, both features can be traced back to the localization of excitons at cryogenic temperatures [122]. Before recombination excitons probe ten thousands of CNT lattice sites during their diffusion, so that the PL signal of CNTs was identified as particularly sensitive to environmental fluctuations and bonding of individual ad-atoms to the CNT [73, 123, 124]. During diffusion excitons experience variations in the energy landscape, which can result in localization of excitons and formation of bright emission sites along a CNT [58]. Typically, such sites show PL emission with an energy shifted to the red by several 10 meV [125]. The localization of excitons was also revealed by analyzing the ultra-fast dynamics of exciton generation and decay [126]. In addition, the localization of excitons is purposefully responsible for the asymmetric PL emission line shape [59] and the quantum dot like photon emission of cryogenic CNTs [76, 77, 127].

We begin with the analysis of the PL line shape. Its asymmetry has been identified as a fundamental property of the PL from individual CNTs at lowest temperatures, whereas the line shape becomes symmetric at higher temperatures of  $T = 77$  K and beyond [60, 121]. As exemplified in Fig. 3.7(a), we observed an analogous behavior within our experiments. To quantify the line shape of a PL peak, we used a simple asymmetric peak function, which was composed of two halved Lorentzians<sup>23</sup> each featuring a different width (full width half maximum). The half on the blue side exhibited a steep width  $\Gamma$ , whereas the half on the red was additionally broadened by  $\Gamma_{\text{asy}}$ . The total width of this asymmetric peak was given by  $\Gamma + \Gamma_{\text{asy}}$ . As depicted by the blue solid line in Fig. 3.7(b), this asymmetric peak function reproduced the PL spectra of individual CNTs at  $T = 4.2$  K.

The broadening of the line width as a function of the temperature  $\Gamma(T)$  has been investigated by Yoshikawa et al. [121]. Since these studies covered only temperatures ranging from 40 K to 300 K, the line shapes were predominantly symmetric. In agreement with these studies, we find  $\Gamma$  following a model [128] that considers exciton

---

<sup>23</sup>The Lorentzians are halved around the central PL energy  $E_{\text{PL}}$ . The asymmetric peak function is defined as

$$I(E) = \left\{ \begin{array}{ll} \frac{2I_0(\Gamma+2\Gamma_{\text{asy}})}{\pi} & \frac{\Gamma+2\Gamma_{\text{asy}}}{4(E-E_{\text{PL}})^2+(\Gamma+2\Gamma_{\text{asy}})^2}, \quad \text{for } E < E_{\text{PL}} \\ \frac{2I_0\Gamma}{\pi} & \frac{\Gamma}{4(E-E_{\text{PL}})^2+\Gamma^2}, \quad \text{for } E \geq E_{\text{PL}}. \end{array} \right\} \quad (3.1)$$

Here,  $I_0$  denotes the intensity.  $\Gamma$  is the symmetric part of the line width, whereas  $\Gamma_{\text{asy}}$  denotes the asymmetric part. The total line width is then given by  $\Gamma + \Gamma_{\text{asy}}$ .

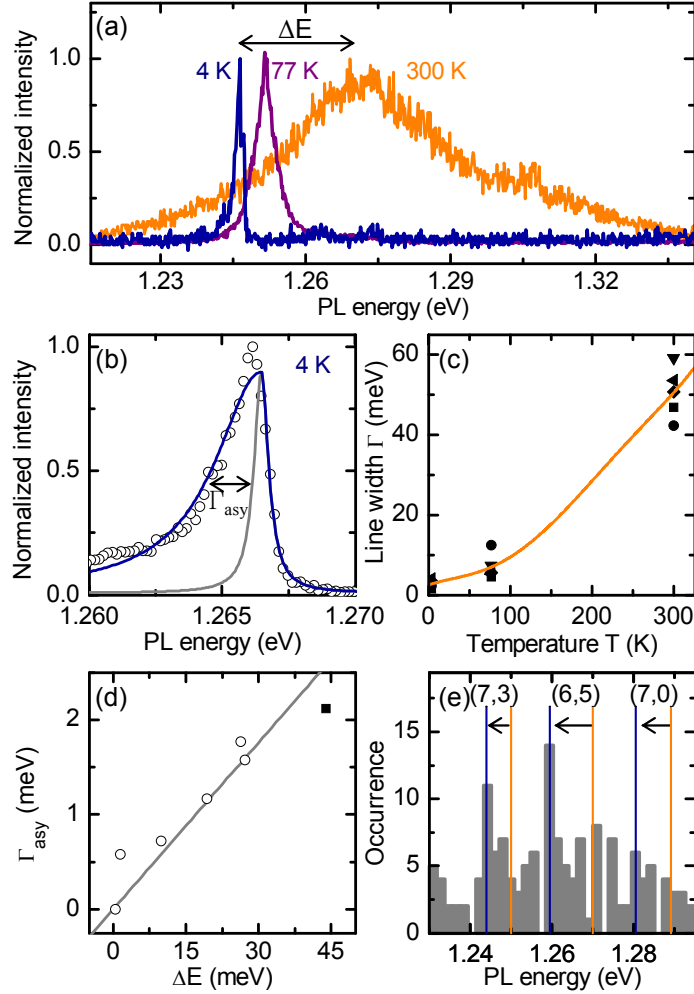


Figure 3.7.: **Spectra of individual CNTs at various temperatures:** (a) For various the temperature of 4 K (blue solid line), 77 K (purple), and 300 K (orange) the spectrum of an individual CNT features a total energy shift  $\Delta E$ . (b) The asymmetric line shape at  $T = 4.2$  K is reproduced by an asymmetric peak function (blue solid line), which quantifies the asymmetry  $\Gamma_{\text{asy}}$  on the lower energy side. (c) Symmetric line width as a function of temperature agrees to a model including interaction to low- and high-frequency phonon modes [128] depicted as orange solid line. (d) Asymmetry  $\Gamma_{\text{asy}}$  as a function of the energy shift  $\Delta E$  revealing a positive correlation between localization potential and asymmetric line shape. Filled square: data reported by [59]. Grey solid line: linear guide to the eye. (e) PL energy of 145 individual CNTs at  $T = 4.2$  K (grey histogram). For the chiralities (7,3), (6,5) and (7,0) the most common observed PL energies are marked by blue solid lines. These are shifted to lower energy compared to experimental room temperature data [88], which are indicated by orange solid lines.

### 3. Photoluminescence of individual carbon nanotubes

coupling to low- and high-frequency phonon modes

$$\Gamma = \Gamma_0 + A T + B \frac{1}{e^{\frac{\hbar\omega_{\text{phonon}}}{k_B T}} - 1} . \quad (3.2)$$

In this model the parameter  $A$  measures the coupling to low-frequency phonon modes, whereas  $B$  gives the coupling to high-frequency phonon modes. The energy of the high-frequency phonon modes is termed as  $\hbar\omega_{\text{phonon}}$ . When this model is applied to our findings as indicated by the orange solid line in Fig. 3.7(c),  $A = (0.05 \pm 0.04)$  meV/K agrees with the previously reported value of 0.03 meV/K [121]. In contrast to Yoshikawa's report, the interaction with high frequency phonon modes can not be neglected because our experiments covered a broader temperature range. Considering only interaction to the radial breathing mode (RBM), we find  $B = (141 \pm 41)$  meV/K.

$\Gamma_{\text{asy}}$  quantified the peak asymmetry and ranged typically from 0.04 meV to 1.8 meV with an mean value of  $(0.4 \pm 0.1)$  meV at  $T = 4.2$  K. We observed for some emission peaks a  $\Gamma_{\text{asy}}$  that exceeded  $\Gamma$  up to a factor 150 at  $T = 4.2$  K, whereas the asymmetric part became insignificant  $\Gamma_{\text{asy}} < 0.22\Gamma$  for all investigated CNTs at room temperature. As origin of the asymmetry at cryogenic temperature Galland et al. [59] proposed a model based exciton-phonon coupling of localized excitons. They evaluated localization potentials on the scale of a few 10 meV and associated explicitly an asymmetry of  $\Gamma_{\text{asy}} = 2.1$  meV with a localization potential of 44 meV. Although their model allows to describe the asymmetry of CoMoCat CNTs at cryogenic temperatures, it fails to understand the ultra-narrow emission of suspended CVD CNTs, which are highly isolated from their environment (discussed in Chap. 5). Thus, we will not evaluate the localization potential in their terms. Rather, we will use a different measure to quantify the localization potential. This is termed as  $\Delta E$  and quantifies the apparent energy shift on the PL energy, when the temperature is increased

$$\Delta E = E_{\text{PL}}(T = 300 \text{ K}) - E_{\text{PL}}(T = 4.2 \text{ K}) , \quad (3.3)$$

which is also depicted in Fig. 3.7(a). For all investigated CNTs, this shift was positive between 0.4 meV up to 27.3 meV indicating a generally reduced PL emission energy at cryogenic temperature. As illustrated in Fig. 3.7(d), we were able to find a positive correlation between this energy shift  $\Delta E$  and the asymmetry  $\Gamma_{\text{asy}}$ . This correlation coincides with Galland's report, which is marked as black filled circle in Fig. 3.7(d).

### 3.5. Exciton localization at low temperatures

Analogous to Galland’s proposal this correlation suggests that the asymmetry of the PL emission peak and the energy shift have the same physical origin.

Furthermore, we identified energy shifts on the same order of magnitude by considering the distribution of the PL energies of 145 CNTs recorded at  $T = 4.2$  K as illustrated in the histogram in Fig. 3.7(e). For the most frequent CNT chiralities (6,5), (7,0) and (7,3) this histogram displays solid orange lines, which indicate room temperature values of the PL energy of CoMoCat CNTs reported by Weisman et al. [88]. In addition, blue solid lines indicate the most common PL energies observed within our experiments at  $T = 4.2$  K. Comparing both lines, the distribution of the PL energy at cryogenic temperature can be interpreted as generally reduced by 60, 105 and 85 meV for (7,3), (6,5) and (7,0) CNTs, respectively (black arrows). Although Weisman’s report considers CNTs with SDS surfactant, only  $\sim 5$  meV of the redshift results from the different surfactant [129]. If we furthermore account for the dielectric SiO<sub>2</sub> substrate with a dielectric constant of  $\epsilon = 3.9$ , environmentally induced redshifts were not reported to exceed 49 meV [106, 130]. Thus, the vast majority of cryogenic CoMoCat CNTs featured an PL energy that was several 10 meV lower than expected. This energy scale agrees with the energy shift  $\Delta E$  as well as with the localization potential observed by Galland et al. [59] in the context of localized excitons interacting with phonons. It is further in accordance with the reduced PL energy of localized excitons directly observed by Georgi et al. [125].

Several alternative mechanisms for temperature induced variation of the PL energy of pristine CNTs are reported. First, a higher temperature increases the carbon-carbon bond length  $a_{cc}$  resulting in a smaller overlap integral  $\gamma_0$  (see Chap. 2.2) and thus a smaller band gap. This was confirmed theoretically [54] and experimentally [60]. Applied to our experiments, this mechanism would result in an higher PL energy at cryogenic temperature. Secondly, axial strain varies the CNT band-gap [131] causing family selective shifts of the PL energy to the red *or* the blue. However, for all the here considered chiralities<sup>24</sup> strain induces shifts only to the blue, which do not exceed a few meV [132]. So, both mechanisms would manifest in an increased PL energy for cryogenic temperatures, which contradicts the here observed energy shifts to lower PL energies.

In summary, we have identified several indication for the localization of excitons in CNT quantum dots at cryogenic temperatures. These are asymmetric emission peaks at low temperature, which has been purposed to originate from the localization of excitons [59]. This comes along with a reduction of the PL energy on the scale of a few

---

<sup>24</sup>(6,5), (7,0) and (7,3) belong to the same family.

### 3. Photoluminescence of individual carbon nanotubes

$\sim 10$  meV that agrees with typical localization potentials of localized excitons [58]. A correlation between the magnitude of the localization potential and the asymmetry of an emission profile indicates that both phenomena have the same physical origin. Thus, our findings can be interpreted by the localization of excitons in CNT quantum dots at cryogenic temperatures. Since these traps measure a few 10 meV, excitons are presumably unable to overcome these localization potentials and recombine mostly from confined emission sites (CNT quantum dots). Not before their energy is on same order of magnitude - as it is the case for room temperature ( $k_B$  300 K  $\approx$  26 meV) - excitons delocalize, which becomes apparent in symmetric emission peaks with a PL energy matching to the CNT band-gap.

A final remark should regard the excitation laser. As we will discuss in Chap. 4.7 localized exciton states can be generated by pumping via higher harmonics of the trapping potential. Tuning the excitation laser to (phonon-)sidebands slightly above the  $E_{11}$  energy gap, could increase the creation of localized exciton states and would make the search for CNTs highly selective to such CNTs that feature exciton localization. This could explain, why experiments using excitation via sidebands face asymmetric PL line shapes [59, 133] and photon anti-bunching [76, 77, 127] indicating for localization of excitons. In contrast, experimentalists using excitation via the  $E_{22}$  electronic states reported mostly on symmetric emission lines [60, 73, 121].

## 4. Tuning the photoluminescence with electric fields

We investigated the PL of cryogenic CoMoCat CNTs as a function of a perpendicularly applied electric field. Prior spectral classification allowed to distinguish between two CNT types [134]: The first consisted of individual CNTs showing a single asymmetric emission peak. As a function of the electric field the PL energy of these CNTs was shifted to the red, which was mediated by the perpendicular polarization of excitons [82,135]. Within our experiments, the energy of both lines was shifted linearly as a function of the applied electric field. We interpret our findings that CNTs of the second type featured a permanent dipole moment that arose from impurities induced breaking of the CNT symmetry.

As a third characteristic, CNTs featured a reversible emergence of an additional satellite peak. In favor of the satellite intensity the intensity of the bright exciton emission line was systematically quenched as a function of the applied electric field. The energy splitting of this satellite peak to the bright exciton line agrees with experimental [47–49] and theoretical [55, 81] values of the charged exciton (trion) splitting. Thus, our findings can be interpreted with the generation of trions by field induced doping of CNTs.

In addition to the homogenous electric field, switching of charge states in the dielectric medium close to a CNT altered an inhomogenous electric field. Controlled by the gate voltage inhomogenous electric fields systematically tuned the localization potential of excitons in individual CNTs [62]. Using photoluminescence excitation spectroscopy [136] we identified that the harmonic excitation spectrum of a CNT quantum dot featured signatures of a phonon bottleneck in the relaxation of excited exciton states [137].

## 4.1. Electric field structure

In order to study optical properties of individual CNTs as a function of an external electric field, we fabricated a metal-oxide-semiconductor (MOS) capacitor device sketched in Fig. 4.1(b). Applying a dc gate voltage ( $V_g$ ) between its top and back gates generates a homogeneous electric field perpendicular to the CNT axis regardless of their orientation on the substrate. To provide for high electric fields, the insulating layers should exhibit a high dielectric strength. As required for efficient PL spectroscopy of CNTs such a device must exhibit (semi-) transparent layers and must be functional at cryogenic temperatures.

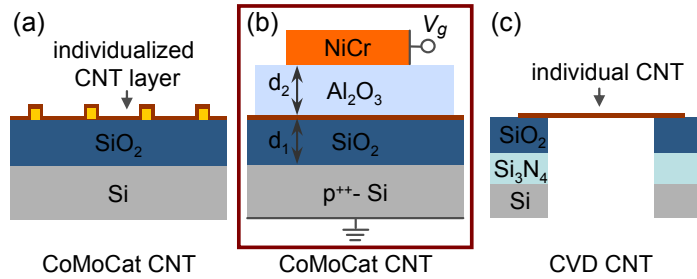


Figure 4.1.: **Sample layouts II:** (a) CoMoCat CNTs on silicon oxide surface, which features a metallic grid. (b) CoMoCat CNTs embedded in an electric gate device. (c) CVD CNT freely suspended over a crater.

For fabrication of such a MOS capacitor, we started with a layer of individualized CNTs on a Si-SiO<sub>2</sub> substrate considered previously in Chap. 3.2. Since the silicon substrate was highly doped, it exhibited a sufficient electric conductance to act as back gate. The CNTs were insulated from the back gate by the dielectric SiO<sub>2</sub> film. To complete the gate structure a second insulating layer (here aluminium oxide Al<sub>2</sub>O<sub>3</sub>) and a semi-transparent metallic top gate (nickel chromium NiCr) were required. As characteristic MOS capacitor, the device exhibited a capacitance-voltage profile (CV) that was dominated by the creation rate of charge carriers in the semi-conducting back gate and by oxide charge states within the insulating layers.

### 4.1.1. Growth and characterization of thin films

#### Silicon oxide

We used highly p<sup>++</sup>-doped silicon wafers<sup>1</sup> (boron dopant) polished on both sides as a substrate material for all devices. The room temperature resistivity was measured to

<sup>1</sup>Acquired from Wacker AG with special thanks to P. Stallhofer

be  $5 - 10 \text{ m}\Omega \text{ cm}^{-1}$  - equivalent to a dopant concentration of  $1 - 2 \cdot 10^{19} \text{ cm}^{-3}$  [138]. The thickness of the thermal silicon oxide film ( $\text{SiO}_2$ ) measured  $d_1 = 100 \text{ nm}$  and was not altered for different sample layouts presented. For further processing the wafer was cut into pieces of  $7 \times 7 \text{ mm}^2$ . On top a layer of individualized CoMoCat CNTs was processed according to methods documented in Appendix C.

### Aluminium oxide

Thin aluminum oxide ( $\text{Al}_2\text{O}_3$ ) films exhibit a high dielectric strength, which are reported to exceed  $10^7 \text{ V/cm}$  [139]. Additionally,  $\text{Al}_2\text{O}_3$  acts as a barrier for mobile sodium ions. These typically contaminate  $\text{SiO}_2$  films and play a central role in the breakdown of pure  $\text{SiO}_2$  capacitors [140]. Thus,  $\text{Al}_2\text{O}_3$  complements ideally to  $\text{SiO}_2$  films for fabrication of thin film capacitors. Furthermore,  $\text{Al}_2\text{O}_3$  is transparent in the visible and near infrared and thus ideal for optical applications.

We deposited  $\text{Al}_2\text{O}_3$  films by electron beam evaporation in a high-vacuum chamber. During the growth process, a quartz microbalance monitored deposition rate (typically  $1 \text{ \AA s}^{-1}$ ) and film thickness. Although this microbalance granted for comparable control of the deposition parameters, it generally underestimated the oxide thickness by  $\sim 30\%$ . More reliable results for the oxide thickness were obtained with ellipsometry measurements<sup>2</sup>. The values measured with this method were in accordance with two other methods used for the determination of the oxide thickness. Firstly, the thickness of the oxide layers were evaluated from the capacitance of the MOS capacitor. Secondly, the color of thin oxide films is governed by the refractive index  $n$  and the film thickness  $d$ . Color tables for thin  $\text{SiO}_2$  films as a function of their thickness are summarized in Ref. [138]. We adopted them to  $\text{Al}_2\text{O}_3$  using  $n_{\text{Al}_2\text{O}_3} \cdot d_{\text{Al}_2\text{O}_3} = n_{\text{SiO}_2} \cdot d_{\text{SiO}_2}$ .

This thesis presents experimental data measured on four different MOS capacitor devices with different thickness of the  $\text{Al}_2\text{O}_3$  film ( $d_2 (\simeq 7 \text{ nm}, 17 \text{ nm}, 39 \text{ nm}$  and  $42 \text{ nm})$ ).

### Nickel chromium

In order to excite CNTs within the gate device and to detect their PL signal the top gate has to be transparent in the near-infrared spectral range. Ideal materials for the top gate would be indium-tin-oxide (ITO) [141] or a mono-layer graphene flake [142]. Alternatively, thin metallic films of nickel chromium (NiCr) films can be used [116]. These are easy to fabricate and semi-transparent in the near infrared.

<sup>2</sup>PC 2300 by Plasmos GmbH, Germany

#### 4. Tuning the photoluminescence with electric fields

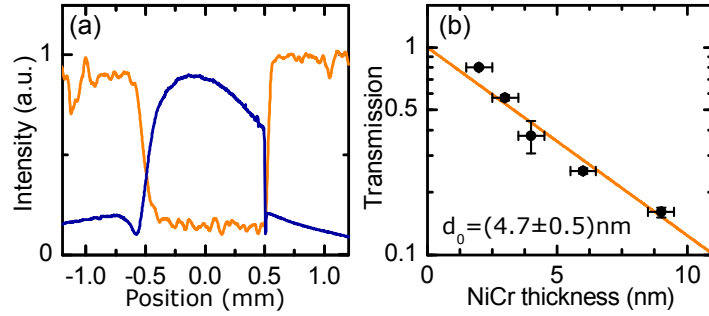


Figure 4.2.: **Fabrication of a semi-transparent top gate:** (a) Transmitted (orange trace) and reflected (blue trace) intensity as a function of the laser spot position. The range within  $\pm 0.5$  mm was covered with a NiCr film. (b) Transmission coefficient as a function of the NiCr film thickness. The solid orange line represents an exponential decay fit of Lambert-Beer's law.

We deposited a thin layer of NiCr as a top gate by thermal evaporation in a high-vacuum chamber. The deposition rate was controlled by a quartz crystal microbalance and usually set to  $1 \text{ \AA s}^{-1}$ . We used shadow masks to define the shape of the top gate with an area of  $4.6 \text{ mm}^2$  centered on the substrate piece. After deposition we checked the film thickness by ellipsometry. Ellipsometry measurements on composites of NiCr and  $\text{Al}_2\text{O}_3$  films on Si-SiO<sub>2</sub> substrates were reported by Ohlidal et al. [143].

The ideal NiCr thickness is a trade-off between light absorption and electric bulk conductivity. Fig. 4.2 summarizes the transmission coefficients for NiCr films with various thickness measured at 960 nm. Applying the Lambert-Beer law [144], we find a half-value thickness  $d_0 = (4.7 \pm 0.5) \text{ nm}$ . Further, we performed measurements of the electrical dc resistance on test samples. We did not observe any deviations from a bulk conductor and found a constant resistivity for all films thicker than 2.0 nm. For all MOS devices considered in this thesis the NiCr thickness was between 2.0 and 4.5 nm.

##### 4.1.2. Ohmic contacts

In order to apply a voltage between the NiCr film (top gate) and the highly doped silicon substrate (back gate) both were contacted to a voltage source. Contacting a thin metallic wire to the semiconducting back gate could result in a junction dominated by a Schottky barrier [145] whereas the junction between a metallic wire and the metallic top gate was not subject to this difficulty. Such non-ohmic behavior would inhibit a reasonable operation of the device especially at low temperatures.

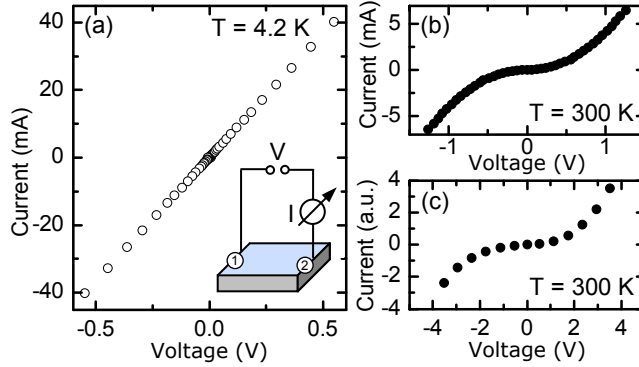


Figure 4.3.: **Ohmic contacts:** (a) Linear current-voltage characteristic of two ohmic contacts generated by electric welding. (b-c) Examples of non-ohmic contacts, created by adhering a wire with conductive silver varnish to an untreated area and showing a resistance depending on the applied voltage.

We achieved a sufficiently small Schottky barrier by depositing a contact metal with appropriate work function on the edge of the silicon wafer. For highly boron doped  $p^{++}$  doped silicon we used boron doped gold<sup>3</sup> that was diffused into the substrate material. Since the melting temperature of gold (1064 °C) is far above the decomposition temperature of carbon nanotubes ( $\simeq 400^\circ\text{C}$ ), gold should be heated only in a locally confined area at the sample edge. We achieved this by employing the following electric welding technique: A dc voltage of 18 to 22 V was applied between two sharpened boron doped gold wires. Parallel to these wires we loaded a large capacitor ( $\sim 1 \mu\text{F}$ ) in order to provide the high current required during the welding and to save the power supply from damage.

At first, the insulating silicon oxide layer was removed using a glass cutter. This procedure roughened also the substrate in the contact area. Then, we pressed the ends of both gold wires on the roughened surface and reduced the distance slowly until a bright discharging arc occurred. Using a standard optical microscope, small gold droplets were visible where gold diffused into the silicon substrate forming an Ohmic contact. After recharging the capacitor we repeated the procedure a few times and then contacted a metal wire to the treated area with the use of a conductive silver paste<sup>4</sup>.

Ohmic and non-ohmic contacts are compared in Fig. 4.3. We measured the current through a silicon substrate as a function of the applied voltage. The voltage source was connected to two points on the substrate, which were both either prepared with

<sup>3</sup>Thickness: 44.5 g per 3 m, with special thanks to Jörg P. Kotthaus

<sup>4</sup>Leitsilber 200, Hans Wolbring GmbH, Höhr-Grenzhausen, Germany

#### 4. Tuning the photoluminescence with electric fields

(a) or without (b-c) gold contacts. For the gold treated samples we found ohmic junctions with a linear current-voltage characteristic even at a temperature of 4.2 K. In contrast, the contact resistance of an untreated sample revealed a non-ohmic behavior even at room temperature.

## 4.2. Capacitance-voltage characterization

The first part of the following section gives a brief theoretical overview on the electrical properties of an ideal MOS device. Then, we present capacitance-voltage (CV) measurements on our MOS capacitor samples. Knowing the CV characteristic of a device allowed to evaluate the electrostatic field through the layer of individualized CNTs. On a microscopic level this field was not only dominated by the homogeneous electric field generated between the biased top and back gate capacitor plates. Rather, an additional inhomogeneous electric field arose from oxide charge states located in the dielectric medium close to the CNT layer. From comparative measurements of devices with different layer geometry we evaluated the oxide charge density in the MOS capacitor device.

### 4.2.1. Ideal MOS capacitor

The ideal MOS device is *not* an ideal parallel-plate capacitor [138]. Rather, its CV characteristic is dominated by the semiconducting nature of the back contact. Particularly, the generation rate of charge carriers within the semiconductor contrasts mainly to a metal-plate capacitor. Fig. 4.4(a) depicts the density of charge carriers  $Q_s$  as a function of the surface potential  $\phi_s$  (that is not identical to the applied gate voltage  $V_g$ !) for a p-type semiconductor. For reverse bias  $\phi_s < 0$ , accumulation of majority charge carriers provides for a metal-like charging characteristic. For small forward bias, the majority carriers are depleted from the semiconductor surface. The width of the depletion region is denoted by  $x_d$ . Since there are no minority carriers available, the intrinsic Fermi level  $E_i$  is still above the Fermi energy  $E_F$ . Only when  $E_i$  is bent below  $E_F$ , forward biasing gives rise to the accumulation of minority carriers also referred to as inversion.

In the following, we briefly present the calculations by Grove et al. [146] for a p-type MOS capacitor. These are also summarized in the standard textbook on semiconductor physics by Sze [138], which elaborates particularly on the effects of charge states. We followed these calculations to relate the applied gate voltage  $V_g$  to

## 4.2. Capacitance-voltage characterization

the strength of the created homogeneous electric field  $F$ . Furthermore, we determined the average density of oxide charge states  $Q_{OT}$  in the surrounding of the CNT layer.

In general, the capacitance of a MOS device can be regarded as a series connection of the oxide capacitance<sup>5</sup>  $C_o$ , which is the capacitance of a parallel plate capacitor with identical dimensions  $C_o = \epsilon\epsilon_0/d$ , and the differential or space charge capacitance  $C_s$  accounting for all effects due to the semiconducting nature of the back gate

$$\frac{1}{C} = \frac{1}{C_o} + \frac{1}{C_s}. \quad (4.1)$$

In thermodynamic equilibrium, the carrier concentration of electrons and holes within the semiconductor is given as a function of the surface potential  $\phi_s$  by

$$p = n_i \exp(u_F - u_s) \quad (4.2)$$

$$n = n_i \exp(u_s - u_F) \quad (4.3)$$

where we define the relative potentials  $u_s = q\phi_s/k_B T$  and the intrinsic carrier concentration  $n_i$ . At  $T = 300$  K,  $n_i(300\text{ K})$  is given by  $n_i^0 = 1.45 \cdot 10^{10} \text{ cm}^{-3}$ . For other temperatures  $n_i$  scales with  $T^{3/2} \exp(E_g/k_B T)$ . The relative Fermi potential  $\phi_F$  depends on the dopant concentration only. For a p-type semiconductor the bulk density of acceptors  $N_A$  exceeds the density of donors  $N_D$ . Thus, the Fermi level is shifted towards the valence band and we can write for the Fermi potential

$$2n_i \sinh u_F = q(N_A - N_D) > 0. \quad (4.4)$$

Solving the Poisson equation yields the total net charge density  $Q_s$  within the semi-

<sup>5</sup>In accordance with Ref. [138, 146]  $C$  denotes here the capacitance per area given in units of  $\text{F}/\text{cm}^2$

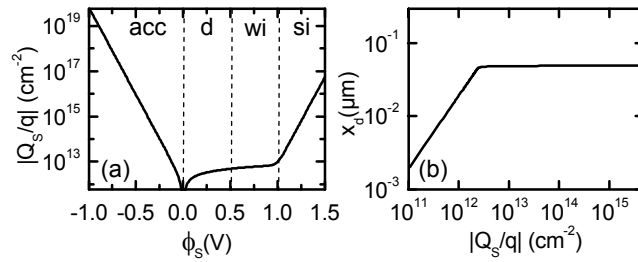


Figure 4.4.: **Charge density  $Q_s$  and depletion width  $x_d$**  calculated for the given sample parameters at  $T_{\text{eff}} = 324$  K. (a)  $Q_s$  as a function of the surface potential  $\phi_s$  showing accumulation (acc), depletion (d), weak (wi) and strong inversion (si). (b) Depletion width  $x_d$  saturates when weak inversion sets in.

#### 4. Tuning the photoluminescence with electric fields

conductor as shown by Kingston et al. [147]. So,  $Q_s$  is expressed as a function of the surface potential  $\phi_s$  and reads as

$$Q_s = -2 \frac{u_s}{|u_s|} q n_i L_D \sqrt{2 [\cosh(u_s - u_F) - \cosh(u_F) + u_s \sinh u_F]} \quad (4.5)$$

with the Debye length  $L_D$  defined by

$$L_D = \sqrt{\frac{k_B T \epsilon_s \epsilon_0}{2q^2 n_i}} . \quad (4.6)$$

Here,  $k_B$  denotes the Boltzmann constant,  $q$  the elementary charge and  $\epsilon_s$  the dielectric constant of the semiconductor. Fig. 4.4(a) depicts the number of charge carriers  $|Q_s/q|$  as a function of the surface potential  $\phi_s$ . For large forward ( $\phi_s \gg 0$ ) and reverse ( $\phi_s \ll 0$ ) bias, it shows a metal like exponential increase, which results in strong inversion (si) and accumulation (acc) of holes, respectively. Around zero bias,  $|Q_s/q|$  increases only slightly in the depletion (d) and saturates for weak inversion (w) due to the lack of electrons.

#### Generation of minority carriers

At equilibrium, the space charge capacitance  $C_s^{\text{minority}}$  is given by the derivative of the charge density  $Q_s$  with respect to  $\phi_s$ . Using Eq. (4.5), we find

$$C_s^{\text{minority}} = \epsilon_s \epsilon_0 \frac{q(p - n + 2n_i \sinh u_F)}{Q_s} . \quad (4.7)$$

#### Domination of majority carriers

However, the situation is different when there is only an insufficient density of minority carriers available. This is the case for high modulation frequency or at low temperature. Here, the CV characteristics is solely governed by majority carriers and their depletion, which sets in at small forward biasing. The width of the depletion region  $x_d$  is defined by

$$x_d = \frac{Q_s}{q(N_D - N_A)} , \quad (4.8)$$

which is the ratio of the surface charge density  $Q_s$  to the uniform doping (bulk) density  $N_D - N_A$ . Knowing the dopant concentration,  $x_d$  can be evaluated explicitly with use of Eq. (4.5). For the given material properties of our devices, Fig. 4.4(b) plots  $x_d$  as a function of the surface potential  $\phi_s$ . The depletion width  $x_d$  saturates

## 4.2. Capacitance-voltage characterization

when the charges in the depletion region screen completely the electric field from the semiconductor. Hence, the resulting space charge capacitance  $C_s^{\text{majority}}$  is only determined by  $x_d$  and reads as

$$C_s^{\text{majority}} = \frac{\epsilon_s \epsilon_0}{x_d} . \quad (4.9)$$

### Charge states

The used MOS devices differed from the above considered ideal CV curve in several points. Charge impurities were the most dominant difference. On a microscopic level, an individual CNT was subject to the inhomogeneous electric field of charge states in addition to the homogenous electric field generated by the charged gates. However, CNTs were only affected by neighboring charge states located in the dielectric medium whereas they were insensitive to charge states on the Si-SiO<sub>2</sub> interface. The latter resulted from open silicon bonds and are termed as interface trap charges. Their surface density is here denoted as  $Q_{\text{IT}}$ . In contrast, volume states ranged over the entire dielectric medium and originate from oxide trap charges<sup>6</sup>. The density of these oxide charge states is given by  $Q_{\text{OT}}$ . Thus, we can state the total density of charge states  $Q_{\text{tot}}$  as the sum of the interface charge density and the oxide charge density

$$Q_{\text{tot}} = Q_{\text{IT}} + Q_{\text{OT}} . \quad (4.10)$$

### Gate voltage $V_g$ as a function of the surface potential $\phi_s$

Up to now we considered all relations as a function of the surface potential  $\phi_s$ . In experiments however, only the gate voltage  $V_g$  applied between top and back gate was controllable. This applied voltage is enhanced by the work function difference between the metallic top gate and the semiconducting back gate  $\phi_{\text{MS}}$  (for NiCr and Si  $\phi_{\text{MS}} \approx -1.0$  V) and by possible charge states  $Q_{\text{tot}}$ . On the other hand, the surface potential  $\phi_s$  is lowered by the potential, which arises from the space charge capacitance  $Q_s/C_o$ . Hence, we can write

$$V_g - \phi_{\text{MS}} + Q_{\text{tot}}/C_o = \phi_s - Q_s(\phi_s)/C_o . \quad (4.11)$$

---

<sup>6</sup>Here, we do not distinguish between the respective physical origin of a charge state in the insulator volume. Of course they can be oxide traps, mobile ions, fixed charges [138] or of any other nature. To simplify matters they are all summarized in the term "oxide charge state".

#### 4. Tuning the photoluminescence with electric fields

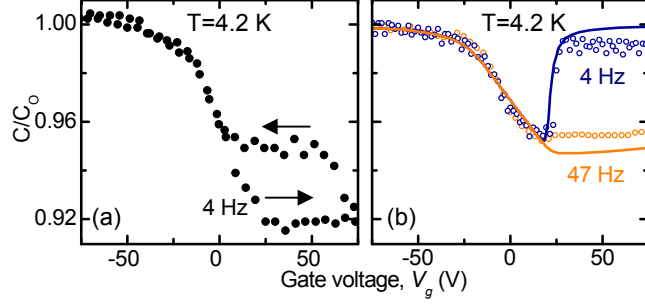


Figure 4.5.: **CV characteristics of the MOS capacitor device:** (a) Capacitance as a function of gate voltage  $V_g$  measured on a typical sample ( $d_1 = 100$  nm,  $d_2 = 7$  nm) at  $T=4.2$  K with a modulation frequency  $f_{\text{mod}} = 4$  Hz. (b) The same sample but illuminated with a diffuse laser beam which enhanced the generation rate of charge carriers. For low modulation frequency ( $f_{\text{mod}} = 4$  Hz, blue circles) the capacitance recovered to  $C_o$  for positive biasing, whereas it remained reduced for high modulation frequency ( $f_{\text{mod}} = 47$  Hz, orange circles). The solid lines display the theoretical limits of a sufficient (blue solid line) and insufficient (orange solid line) generation rate of minority carriers, here plotted for  $T_{\text{eff}} = 324$  K and  $Q_{\text{tot}} = 3.6 \cdot 10^{-12} \text{cm}^{-2}$ .

To evaluate our experimental results, which were given as a function of  $V_g$ , with the here presented theoretical considerations, which were a function of  $\phi_s$ , it is necessary to transpose all the foresaid analytic expressions for the capacitance (Eqs. 4.7 and 4.9) as a function of the gate voltage  $C(V_g)$ . However, this is a delicate task since  $Q_s$  and  $x_d$  are both function of  $\phi_s$ . Thus, we did not evaluate an analytic expression for  $C(V_g)$  explicitly. Rather, we preserved the parameter  $\phi_s$  for the later following fitting procedure. In detail, we employed a two-dimensional fitting routine to fit value pairs  $V_g(\phi_s)$  (Eq. 4.11) and  $C(\phi_s)$  (Eqs. 4.7 and 4.9) to experimental data.

#### 4.2.2. Measuring the capacitance

For all spectroscopic experiments we employed a Yokogawa<sup>7</sup> dc source, which delivered a highly stable voltage ranging from -32 to 32 V ( $\pm 0.001\%$ ). However, this range was insufficient for the entire characterization of the MOS capacitor. Thus, we used here a Delta Electronika<sup>8</sup> dc source with a wide but uni-polar range up to 300 V. Of course, this was expandable -300 V by inverting the polarity with respect to the top and the back gates.

We employed a differential capacitance measurement technique by admixing a sinusoidal modulation voltage with amplitude  $\delta V = 10$  mV and frequency  $f_{\text{mod}}$  in

<sup>7</sup>7651 Programmable DC Source by Yokogawa Electric Corporation, Tokyo, Japan

<sup>8</sup>ES0300-0.45 by Delta Elektronika, Zierikzee, The Netherlands

## 4.2. Capacitance-voltage characterization

the range of 4 to 450 Hz to a dc gate voltage  $V_g$ . The resulting ac current was demodulated with a lock-in amplifier<sup>9</sup>. Thereby the in-phase or resistive current was close to zero whereas the out-of-phase or capacitive current was scaled to the current of a reference capacitance. For a detailed investigation we performed voltage sweeps by starting at zero bias.  $V_g$  was first increased to its maximum value  $V_g^{\max} = +80$  V, then decreased down to its minimum  $V_g^{\min} = -V_g^{\max} = -80$  V and finally ramped back to zero.

At room temperature, already ramping  $V_g$  to a few volts caused an exponentially increasing leakage current. By careful increase of  $V_g$  this rise of current could be used as a precursor for a following breakthrough. Thus, we ramped the voltage immediately back to zero whenever it occurred. Unfortunately, this low dielectric strength prevented the characterization of the CV profile for almost all investigated samples at room temperature.

At cryogenic temperature of  $T = 4.2$  K all samples routinely showed only small resistive currents even for high dc voltages. In accord with the geometry of our devices we obtained a typical capacitance of  $\sim 1$  nF. This capacitance varied slightly with the applied gate voltage  $V_g$ . As exemplarily depicted in Fig. 4.5(a) for a device with  $d_1 = 100$  nm and  $d_2 = 7$  nm, the CV curve was dominated by majority charge carriers (holes) showing a reduction of capacitance to  $C_{\min}/C_o \simeq 0.93$  but no recovery of the capacitance for positive voltages. This characteristic remained invariant for all investigated frequencies, indicating a generally low generation rate of electrons. Additionally, the CV curve exhibited a hysteresis for positive voltages, which is well-understood in the context of mismatched rates for charging and discharging of charge traps at the Si-SiO<sub>2</sub> interface [148].

### 4.2.3. Total charge state density $Q_{\text{tot}}$

In order to generate minority carriers even at low temperature, we employed a diode laser ( $\lambda = 685$  nm) to illuminate the entire sample. This was performed on the same device, whose CV curve is shown in Fig. 4.5(a). The CV characteristic of the illuminated device is illustrated for high ( $f_{\text{mod}} = 47$  Hz) and low ( $f_{\text{mod}} = 4$  Hz) frequency modulation in Fig. 4.5(b). For low-frequency modulation (blue traces) the depletion of holes was almost completely compensated by electrons for forward biasing. Due to this strong inversion, the capacitance recovered to its initial value  $C_o$ . In contrast, the generation-recombination rate of minority carriers could no longer follow the higher modulation frequency (orange traces).

---

<sup>9</sup>7265 DSP Lock-in Amplifier by Signal Recovery, Oak Ridge, TN, USA

#### 4. Tuning the photoluminescence with electric fields

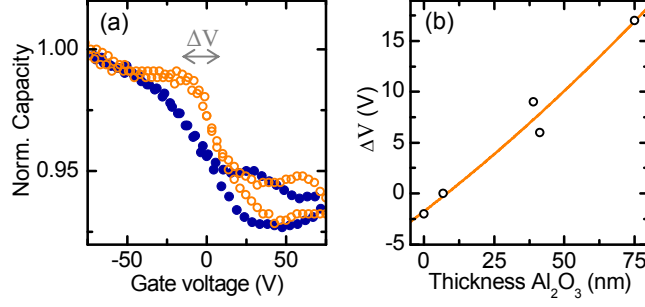


Figure 4.6.: **Estimation of the oxide charge density:** (a) CV characteristic of two samples differing only in their respective thickness of the Al<sub>2</sub>O<sub>3</sub> film, which is  $d_2 = 7$  nm (orange open circles) and  $d_2 = 75$  nm (blue filled circles), respectively. Due to the different concentration of charge states  $Q_{\text{tot}}$  the curves are shifted by  $\Delta V$ . (b)  $\Delta V$  as a function of  $d_2$ . The solid line displays a fit according to Eq. (4.12) and estimates the surface charge density  $Q_{\text{IT}}$  as well as the respective oxide charge volume densities  $Q_{\text{SiO}_2}/d_1$  and  $Q_{\text{Al}_2\text{O}_3}/d_2$ .

We were able to bring these curves in accord with the theoretical predictions using identical fitting constants for both of them. We employed Eq. (4.9) for the case of high frequency modulation or domination of majority carriers and Eq. (4.7) for low frequency modulation. We used the dopant concentration<sup>10</sup> and the oxide capacitance<sup>11</sup> as sample specific material constants and the physical constants summarized in the Appendix A.1.

As one out of two free fitting parameters, we introduced an effective temperature  $T_{\text{eff}}$ , which varied the intrinsic carrier concentration  $n_i$ . Thereby  $T_{\text{eff}}$  accounts for the unknown number of minority carriers created by the laser light. Secondly, we used the total density of charge states  $Q_{\text{tot}}$ , which was incorporated in the mapping of the surface potential  $\phi_s$  to the gate voltage  $V_g$  (Eq. 4.11). As depicted by the solid lines in Fig. 4.5(b),  $T_{\text{eff}} = 324$  K and  $Q_{\text{tot}} = 3.6 \cdot 10^{-12} \text{cm}^{-2}$  resulted in the best accordance with the experimental data.

However, this method gave only a first estimation of the total charge state density  $Q_{\text{tot}}$  in this specific device. Thus, we compared the CV characteristics of five different samples to distinguish between the oxide charge state density  $Q_{\text{OT}}$  in the insulator volume and the surface charge state density  $Q_{\text{IT}}$  at the Si-SiO<sub>2</sub> interface. These five samples differed only in their thickness  $d_2$  of the respective Al<sub>2</sub>O<sub>3</sub> film. As shown in Fig. 4.6(a), the corresponding CV curves were respectively shifted by  $\Delta V$  due to a

<sup>10</sup>dopant concentration  $N_A - N_D = 5 \cdot 10^{-19} \text{cm}^{-3}$

<sup>11</sup>oxide capacitance  $C_o = 3.25 \cdot 10^{-8} \text{F cm}^{-2}$

varying total charge state density  $Q_{\text{tot}}$ . Comparing with Eq. (4.11) we can write

$$\Delta V = q Q_{\text{tot}} \frac{1}{C_o} = q(Q_{\text{IT}} + Q_{\text{OT}}) \left( \frac{d_1}{\epsilon_0 \epsilon_{\text{SiO}_2}} + \frac{d_2}{\epsilon_0 \epsilon_{\text{Al}_2\text{O}_3}} \right). \quad (4.12)$$

However, the oxide density  $Q_{\text{OT}}$  (surface density!) is also a function of  $d_2$ . Thus, we used the volume density  $Q_{\text{OT}}/(d_1 + d_2)$  as a free fitting parameter since this is constant for all  $d_2$ . Including our first estimation of  $Q_{\text{tot}}$  from our previous considerations and fitting this relation to the relative voltage shifts as a function of  $d_2$  (see Fig. 4.6), we obtained an estimation of the oxide charge volume densities  $Q_{\text{OT}}/(d_1 + d_2) = 2.7 \cdot 10^{17} \text{ cm}^{-3}$  and the surface charge density  $Q_{\text{IT}} = 8.2 \cdot 10^{11} \text{ cm}^{-2}$ . In particular, the latter value accords with previous reports [146]. Finally, we could estimate the number of oxide charges neighboring an individual CNT. Assuming an average tube length of 200 nm, one oxide charge state is expected in a radius of 2.4 nm around the tube axis.

### 4.3. Jitter analysis

Several experiments [63, 149] investigated the optical properties of CNTs interacting with a substrate, which could arise from charge fluctuations in the substrate material and results in the spectral diffusion of the PL emission. In contrast, freely suspended CNTs are isolated from any substrate material and show a reduced spectral diffusion [71, 127]. The same holds for CNTs embedded in a polymere medium, which is free of fluctuating charge impurities [77]. Both is not applicable for construction of electric devices that allow to apply high electric fields perpendicular to the CNTs, like the MOS capacitor presented in the previous sections. Here the CNTs were sandwiched between two oxide materials that exhibit plenty of charge impurities as they became apparent in the CV characteristics (see Chap. 4.2). Furthermore, all experiments were carried out at a temperature of 4.2 K, which resulted narrow emission lines (see Chap. 3.5) that were particularly sensitive to spectral diffusion. Thus, the PL of individual CoMoCat CNTs featured spectral diffusion due to interaction with close fluctuators and intermittency due to shelving into dark states. We quantified spectral diffusion and intermittency of individual CNTs embedded in a MOS capacitor by recording systematically PL time traces for CNTs in all three environmental conditions: Firstly, these CNTs were located on a  $\text{SiO}_2$  substrate, secondly, CNTs embedded between  $\text{SiO}_2$  and  $\text{Al}_2\text{O}_3$  films, and thirdly CNTs within the gate struc-

#### 4. Tuning the photoluminescence with electric fields

ture (namely, on a  $\text{SiO}_2$  surface and under a thin film of  $\text{Al}_2\text{O}_3$  that is additionally covered by a semitransparent NiCr film).

Fig. 4.7 displays spectra (upper panels) and PL time traces in false color plots (lower panels) for a representative CNT of each environmental condition. They revealed the main spectral features of micelle-encapsulated CoMoCat CNTs at cryogenic temperatures reported previously [59,76]: asymmetric line shapes and spectral jitter. The latter shall be analyzed here with regard to intensity and PL energy. At first we turn to the evolution of the PL energy that is termed as spectral diffusion. In the next section we will analyze these time traces with respect to blinking and intermittency.

##### 4.3.1. Energy jumps

Fernée et al. reported on a statistical method to identify the origin of spectral diffusion observed in colloidal quantum dots at low temperature [150]. For a series of spectra taken in short time intervals, they analyzed the statistical dependence of the emission energy on its "past". This allows to distinguish between continuous and discrete evolution of the emission energy. The interaction of a nano-emitter with a bath of external fluctuators results in a continuous evolution of its emission energy, which is statistically independent from its "past". The magnitude of spectral jumps follows a Poissonian statistics for all time scales. In contrast, a discrete evolution

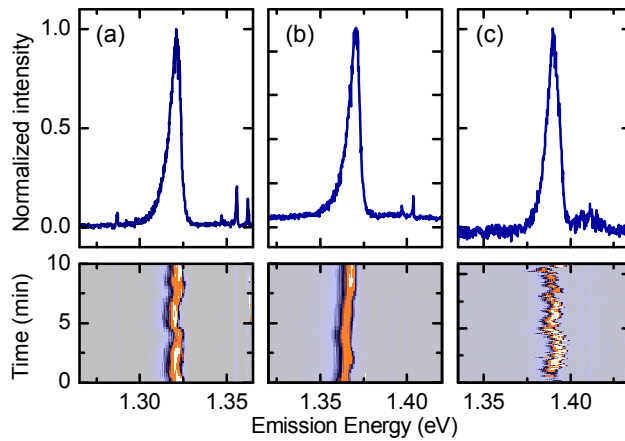


Figure 4.7.: **Spectra (upper panels) and time traces (lower panels) for CNTs on the MOS capacitor samples:** Asymmetric line shapes and spectral jitter were identified for all CNTs on these samples, regardless if they were embedded in the MOS capacitor (a), covered with an  $\text{Al}_2\text{O}_3$  film (b) or located on the bare  $\text{SiO}_2$  substrate.

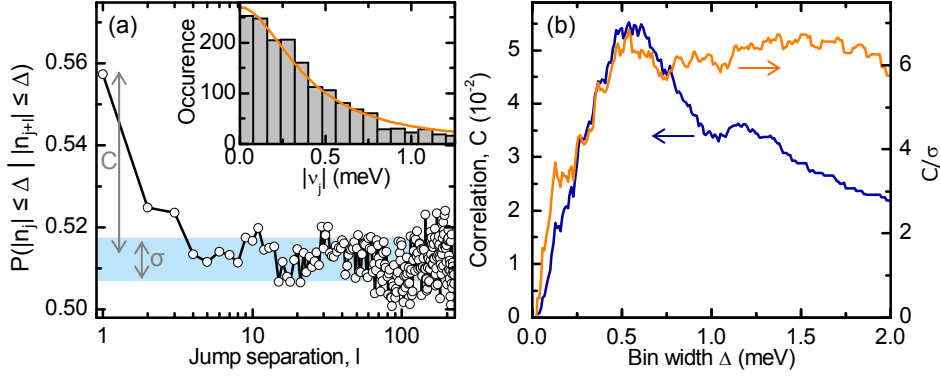


Figure 4.8.: **Jitter correlation in PL time traces:** (a) Conditional probability  $p_{|\nu_j| \leq \Delta | |\nu_{j+l}| \leq \Delta}$  as a function of the jump separation for a jump separation of  $\Delta = 0.41$  meV. The inset depicts the distribution of spectral jumps  $|\nu_j|$ . (b) Correlation  $\mathcal{C}$  (normalized to the standard deviation  $\sigma$ ) as a function of the jump separation.

memorizes its recent past and thus is statistically dependent on its former state. This discrete evolution results from interaction with only few neighboring fluctuators.

We analyzed a large number of spectra ( $N=300-1800$ ) taken sequentially with a short integration time of 1 s and used a standard fitting procedure to obtain the central PL energy for every spectrum. The magnitude of a spectral jump  $\nu_j$  is defined as the energy difference  $E_{\text{PL}}^j - E_{\text{PL}}^{j+1}$  taken from two consecutive spectra  $j$  and  $j+1$ . To evaluate the statistical dependence of the spectral jumps, we considered the conditional probability  $p(l, \Delta) = p_{|\nu_j| \leq \Delta | |\nu_{j+l}| \leq \Delta}$ , which is the probability to find two jumps separated by  $l-1$  (jumps) being both smaller than the bin width  $\Delta$ . This probability would be independent from the separation length  $l$ , if the magnitude of the jump  $\nu_j$  followed Poissonian statistics without remembering its "past".

However,  $\nu_j$  did not exhibit Poissonian statistics for the investigated CNTs, as exemplified in Fig. 4.8(a). Rather  $p(l, \Delta)$  exceeded systematically the general mean probability  $-p(\text{inf}, \Delta)$  by several standard deviations  $\sigma$  (for the shown example by  $7\sigma$ ). This systematic deviation from a Poissonian statistics becomes further apparent, if we consider the degree of correlation as a function of the bin width  $\Delta$ , which is defined as

$$\mathcal{C} = p(1, \Delta) - p(\text{inf}, \Delta) . \quad (4.13)$$

For the CNT discussed here, Fig. 4.8(b) depicts the degree of correlation (normalized to  $\sigma$ ) as a function of the bin width  $\Delta$ . For all investigated CNTs,  $\mathcal{C}/\sigma$  increased

#### 4. Tuning the photoluminescence with electric fields

linearly for small  $\Delta$  and saturated after  $\mathcal{C}$  reached its maximum. Since only a limited number of spectra was considered,  $\mathcal{C}$  converged to 0 for very large bin width  $\Delta$ . In simple terms, more and more energy jumps fit in an increasing bin width  $\Delta$  and  $p(\nu, \Delta)$  converges to 1. If we consider  $\mathcal{C}/\sigma$ , this is compensated as  $\sigma$  decreases accordingly.

We identified analogous correlation of the spectral jitter for all investigated CNTs regardless of their environment (Fig. 4.8). In general  $\mathcal{C}_{\max} > 2.2 \sigma$  for all CNTs. This deviates systematically from a Poissonian statistics and a continuous evolution of the PL energy, as it would be expected for excitons that diffuse freely along a CNT and probe an averaged bath of close fluctuators. Thus, this discrete evolution can be interpreted by the formation of CNT quantum dots, which interact with only few neighboring fluctuators. Further experimental support for the localization of excitons in CoMoCat CNT is presented in this thesis: characteristic asymmetric line-shapes (Chap. 3) and photon anti-bunching (Chap. 5). Chap. 3.5.

In brief, a probabilistic analysis of the spectral jitter of cryogenic, individual CNTs revealed that the PL energy is statistically dependent on its recent past. As this characteristic was apparent for all investigated CoMoCat CNTs regardless of their surrounding (see Fig. 4.9(d-f)), we can exclude detrimental effects on the spectral diffusion of individual CNTs, when they are embedded in a MOS capacitor device.

#### 4.3.2. Intermittency and blinking

The fluorescence rate of nano-emitters, may they be nanocrystals or single molecules, features intermittency or blinking. This has been intensively investigated for many different emitters and was summarized in a detailed review by Cichos et al. [151]. Also for CoMoCat CNTs we were able to identify PL blinking, which followed a general power-law. Such a power-law was accordingly reported for many colloidal quantum dots or other single molecule emitters [152].

$$p(\tau_i) \propto \tau_i^{-\chi_i} . \quad (4.14)$$

Here,  $p(\tau_i)$  denotes the probability that an emitter remains in the "on" ("off") state for a period  $\tau_{\text{on}}$  ( $\tau_{\text{off}}$ ). This law was reported to describe intermittency over 2 to 3 decades of  $\tau_i$  with  $\chi_i \sim 1.5$  [151]. Latest experimental reports [63] show that such power laws hold also for fast intermittency in the PL of individual CNTs. Although we were unable to resolve fast intermittency due to a low fluorescence rate, we find a similar power law holds for the range between 1 and 10 s. Figs. 4.9(a-c)

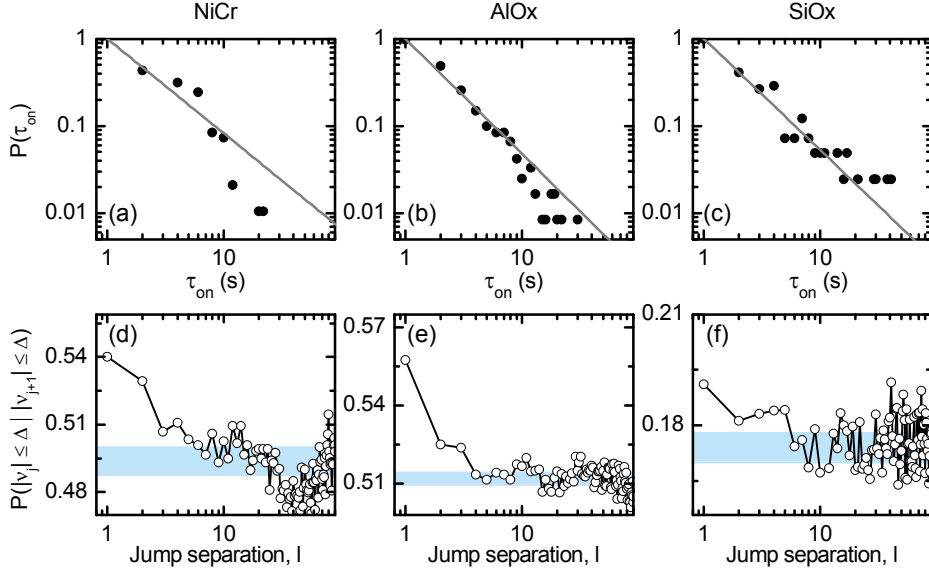


Figure 4.9.: **Intermittency and spectral drifting:** (a-c) Probability distribution for characteristic time in "on" state  $\tau_{\text{on}}$  following a power-law (grey solid lines) for each investigated CNT. (d-f) Jitter correlation: Conditional probability  $P_{|\nu_j| \leq \Delta \mid |\nu_{j+l}| \leq \Delta}$  as a function of the jump separation. The respective range of the standard deviation  $\pm\sigma$  is shaded in light blue.

illustrate  $p(\tau_{\text{on}})$  for a representative of each sample regions. For a given time trace, we investigated the PL intensity for every single spectrum and associated those showing an intensity above (below) the mean PL intensity with the "on" ("off") state. Then we summed over the respective number of consecutive spectra in the "on" ("off") state. Generally  $\chi_{\text{on}}$  was reported between 1.1 and 2.2 for various nanomitters [151], which agrees with our findings of  $\chi_{\text{on}}$  ranging from 1.08 to 1.52 and a mean of value of  $1.28 \pm 0.16$ . We identified an analogous power-law for  $p(\tau_{\text{off}})$  with  $\chi_{\text{off}}$  ranging between 0.97 and 1.63.

In the context of molecules or nanocrystals such intermittency behavior was generally assigned to (photo activated) charging. Whereas  $\chi_{\text{on}}$  is generally independent of the dielectric surrounding [151], colloidal quantum dots show a systematic relation between  $\chi_{\text{off}}$  and  $\epsilon$  due to random charging and de-charging [153]. However, we could not identify a positive relation between the dielectric medium around a CNT and  $\chi_{\text{off}}$ .

PL intermittency of individual CNTs could originate from charging and discharging of CNTs. Such charging would shelve the exciton to a trion state [47–49] while quenching the PL intensity in favor of a trion satellite peak outside the detection

#### 4. Tuning the photoluminescence with electric fields

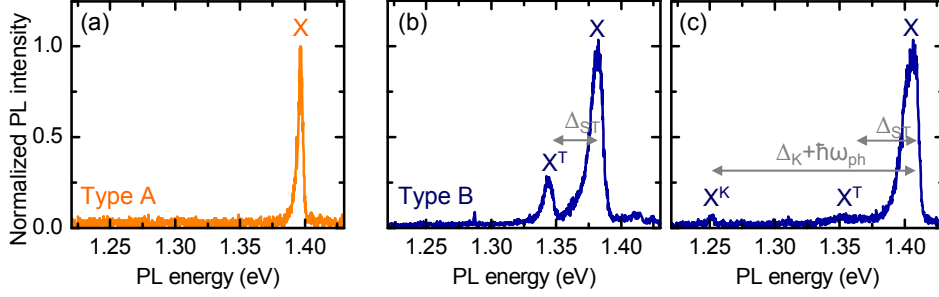


Figure 4.10.: **Example spectra for type A and type B CNTs:** (a) Spectrum of a type A CNT characterized by a single emission line of the bright exciton X. (b-c) Spectra of type B CNTs showing multiple emission lines due to brightening of k-momentum exciton  $X^K$  and triplet excitons  $X^T$ . The respective energy splittings  $\Delta_i$  are defined as positive values.

range. As we will show in the last section of this chapter, this doping of CNTs governed by the nearest surrounding of a CNT quantum dot. This close surrounding consists not only on the dielectric medium ( $\text{SiO}_2$  and  $\text{Al}_2\text{O}_3$ ) but also on an experimentally uncontrolled amount of surfactant molecules. In consequence, the closer dielectric medium around a CNT could vary between  $\epsilon \approx 2.2$  for a CNT packed into sc surfactant and  $\epsilon > 3.9$  for a CNT close to  $\text{SiO}_2$  and  $\text{Al}_2\text{O}_3$ . This could also impede the identification of positive relation between an locally varying  $\epsilon$  and  $\chi_{\text{off}}$ .

In conclusion, the general intermittency of the PL rate from individual CNTs was not affected by embedding these into a MOS capacitor device. Since such blinking is generally associated with charge trapping [151] or the mobility of quenching sites [63], it is consistent with the picture of exciton localization at cryogenic temperature.

## 4.4. Classification of CNTs

### 4.4.1. Multiple peak emission spectra

Before we analyze the PL of individual CNTs as a function of an externally applied electric field, we turn back to the spectral properties of CoMoCat CNTs. In addition to one-peak spectra, which we discussed in Chap. 3, we have identified a second type of spectral emission profile from individual CNTs. The PL spectra of these CNTs showed multiple emission peaks. Two exemplary spectra are depicted in Fig. 4.10. In most cases, we found a bright asymmetric emission peak and a less intense satellite peak shifted to the red. However, in some cases the satellite peaks were on the blue side.

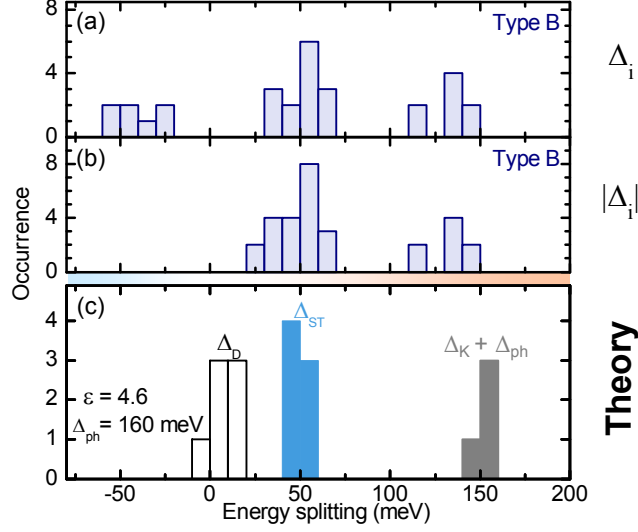


Figure 4.11.: **Energy splittings in two-peaked emission spectra:** (a) Investigating 29 type B CNTs, the energy splitting  $\Delta_i$  between bright emission line and the satellite peak accumulated around -50 meV, +50 meV and 120 meV. (b) Statistical distribution of  $|\Delta_i|$ . (c) Theoretically expected energy splittings of dark exciton (singlet) states from the bright exciton for chiralities within our spectral range. The values base on calculations summarized in Fig. 2.8.

Statistics of the energy splittings  $\Delta_i$  between the bright emission line and satellite peak are illustrated in Fig. 4.11. We identified them clustering around 120 meV and  $\pm 50$  meV, respectively. This accumulation around two discrete energies speaks in favor of a CNT intrinsic energy scale, rather than an external scale like the previously identified depth of localization potentials (see Chap. 3.5).

Indeed, these splittings agree with theoretical predictions of the singlet-triplet splitting [55] and the energy of the k-momentum excitons [34]. Here, we took account for the CNT environment by screening accordingly the Coulomb interaction using Eq. (2.22). We found the best agreement assuming an average dielectric constant of  $\epsilon = 4.6$ , which is expected for CNTs in a medium consisting of aluminium oxide ( $\epsilon_{\text{Al}_2\text{O}_3} = 9.1$ ), silicon oxide ( $\epsilon_{\text{SiO}_2} = 3.9$ ) and sodium-cholate ( $\epsilon_{\text{sc}} \simeq 3.5$ ). Fig. 4.11(c) shows theoretical energy splittings for CNT chiralities within our spectral range. We assign satellites that are red-shifted by  $\sim 50$  meV from the bright exciton as emission from the triplet exciton  $X^T$ . In the same way, we assigned splittings of  $-50$  meV to a less intense bright exciton line and an intense triplet exciton line. Furthermore, satellites with an energy splitting of  $\sim 120$  meV were presumably phonon-sidebands of the k-momentum exciton.

We did not detect any signatures of brightening the lowest dark (singlet) exciton

#### 4. Tuning the photoluminescence with electric fields

state ( $X^D$ ). Nevertheless, emission from the dark exciton was experimentally realized only by use of axial magnetic fields [39–41] and bases on magnetic flux induced valley mixing of bright and dark exciton states [110]. However, theoretical calculations show that such valley mixing cannot originate from impurities [154].

The occurrence of satellite peaks in the emission spectra of individual CNTs is in agreement with recent reports on brightening emission from the k-momentum (singlet) exciton [42, 43] or from triplet exciton states [44–46, 112]. Whereas the first results from mixing of the bright exciton with the k-momentum excitons via exciton-phonon coupling, the other is a consequence of impurity induced spin-orbit coupling. A proposed mechanism is based on a single impurity that distorts the orbitals of single carbon atoms from  $sp^2$  to  $sp^3$  and results in enhanced spin-orbit coupling [78]. Hence, bright (=singlet) and dark (=triplet) exciton states are admixed so that even the dark triplet state acquires a finite oscillator strength [79]. In most reports, the impurities were actively added to the CNTs, for instance by chemical adsorption of hydrogen atoms [112]. Also CNTs treated by intense laser radiation showed satellite emission peaks from exciton triplet states [43, 155].

Within our experiments the used CoMoCat CNTs were commercially purchased in solution. However, dissolving and individualizing CNTs in an aqueous solution required harsh treatment like ultra-sonication that creates lattice defects [156]. Hence, a certain degree of lattice defects was expected. Our results suggest that a large fraction of CNTs was unable to preserve the symmetry upon the cool-down to cryogenic temperatures. Structural defects or charge traps in the surrounding dielectrics were presumably responsible for the breakdown of the trigonal warping model used to describe optical transitions in ideal CNTs. At this point, however, our experiments did not provide insight into the detailed microscopic origin of the reconfiguration of excitonic states in CNTs at cryogenic temperatures.

However, we observed similar two-peaked spectra also for a different CNT material of substrate supported CVD CNTs that we will discuss in Chap. 5. These CNTs featured a single emission peak, when the spectra were recorded within 1 s. However, accumulating their spectral diffusion resulted in two-peaked emission profiles with similar energy splittings of  $\pm 50$  meV. Although this agrees with the splitting to the triplet exciton, the discrete switching between emission *either* from the singlet *or* from the triplet state, contrast the picture of state mixing giving finite oscillator strength to both exciton states.

#### 4.4.2. Emission spectra of type A and type B CNTs

Based on the previous considerations we categorized CNTs into two major classes: Type A CNTs were characterized by a single asymmetric emission line due to recombination from the bright exciton X. In contrast, type B CNTs showed additional emission from dark exciton states, namely triplet excitons  $X^T$  or phonon-sidebands  $X^K$ . Hence, these were identified by their emission spectra showing multiple emission peaks.

A similar categorization was introduced by Matsuda et al. [134] for investigation of spectra diffusion. Whereas type A showed single emission lines with only small spectral diffusion, CNTs with a presumably broken symmetry showed an increased spectral diffusion, which was considered in the framework of a quantum-confined Stark effect.

As we will show in the following, Matsuda's categorization agrees with our findings. Localized excitons in CNTs with a broken symmetry carry a permanent dipole moment that couples the PL energy efficiently to electric field, like external charge fluctuations. Hence, type B CNTs show a broader line-width and an increased spectral diffusion. In contrast, CNTs of type A preserve their symmetry even at low temperature and do not exhibit a permanent dipole moment. As consequence their PL is robust against surrounding charge fluctuations. Thus, type A CNTs show a narrow line-width with a stable emission energy.

### 4.5. Electric field sweeps

For all investigated MOS devices, the overall capacitance changed only on the order of a few percent as a function of the applied gate voltage  $V_g$  as we have shown previously in Chap. 4.2. This allowed to treat the homogeneous electric field strength  $F$  simply as a linear function of the gate voltage,  $F = V_g/(d_1 + d_2)$ . However, we limited the gate voltage to  $V_g^{\max} = 16 - 30$  V to keep the samples from fatal breakdowns. Depending on the thickness  $d_2$  of the aluminium oxide layer electric fields up to  $\pm 0.3$  V/nm were generated.

In the following, we recorded PL spectra of individual CNTs as a function of the electric field  $F$ . In order to distinguish the resulting effects on the PL from the omnipresent spectral diffusion and to trace possible hysteresis effects, we used the following voltage sweep scheme. At first, we took 10-15 PL spectra while keeping top and back gates grounded ( $V_g = 0$ ). Then we ramped the electric field to its maximum  $F_{\max}$  in discrete steps  $\Delta V_g$  (0.5 – 2.5 V) while recording a spectrum

#### 4. Tuning the photoluminescence with electric fields

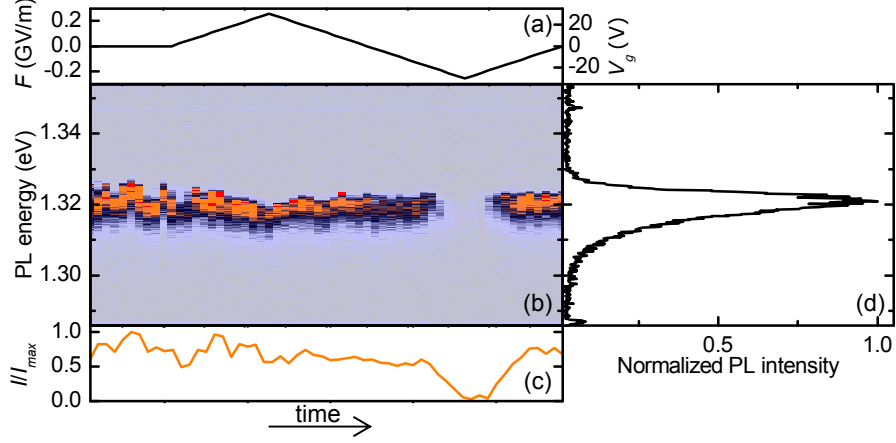


Figure 4.12.: **Polarizability and reversible PL quenching:** (a) Electric field sweep. (b) Contour plot of the PL of an individual CNT showing only small shifts of the PL energy but pronounced reversible quenching of the PL intensity for negative electric fields. (c) Fitted PL intensity illustrating reversible quenching. (d) Spectrum at  $V_g = 0$ .

after each step. From  $F_{max}$  we ramped the field in the same way to its minimum  $F_{min} \approx -F_{min}(V_g^{max} = V_g^{min})$  and finally back to zero. In a nutshell, we recorded a short time trace with no applied electric field and two spectra for every electric field step. The smoothed trace of such an electric field sweep is depicted in Fig. 4.14(a).

During these sweeps, we kept all other controllable parameters constant (sample position, excitation power, wavelength and polarization). For each CNT investigated the excitation wavelength was respectively tuned to a resonance 50-175 meV above  $E_{PL}$  to increase the PL emission intensity. To maximize the PL emission, the axis of linear polarization was adjusted parallel to the tube axis.

##### 4.5.1. Transverse polarizability of excitons

Following this experimental scheme, we investigated type A CNTs, which we pre-classified due to their single asymmetric emission line. Fig. 4.12 exemplifies the trace of the PL spectrum as a function of the electric field. For all type A CNTs investigated the PL energy  $E_{PL}$  varied slightly with the electric field. However, some type A CNTs - as the one depicted here - exhibited a reversible quenching of the PL intensity to less than 10 % of its initial intensity. We could associate this quenching either to doping of the CNT or to detuning of exciton localization potential from the excitation laser. Both effects will be discussed in the second part of this chapter.

Here, we focus on the energy dispersion of the PL as a function of the electric

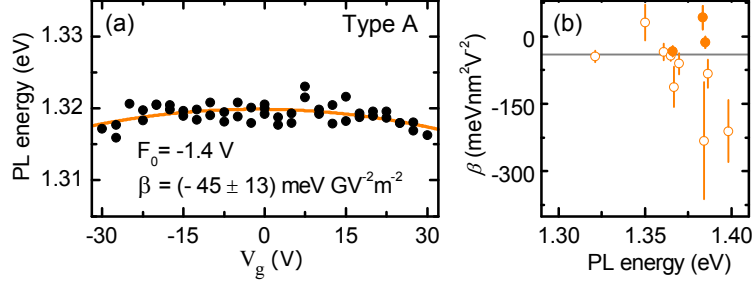


Figure 4.13.: **Transverse polarizability of CNTs:** (a) PL energy as a function of the applied field. Orange solid line displays a quadratic fit with the parameters  $\beta$  and  $F_0$  representing the transverse polarizability and the local field modulation, respectively. (b) Statistics on the polarizability:  $\beta$  as a function of  $E_{\text{PL}}$ . CNTs, which exhibited a high local field modulation ( $|F_0| > 8 \text{ V}$ ) are indicated by filled circles, whereas open circles represent CNTs with small local field modulations ( $|F_0| < 8 \text{ V}$ ). The grey solid line depicts the average of  $\beta = -40 \pm 20 \text{ meV}/(\text{V}/\text{nm})^2$ .

field strength. Fig. 4.13(a) illustrates the energy of the PL maximum as a function of the gate voltage (for the same CNT shown in Fig. 4.12). For all type A CNTs we observed a quadratic relation between the applied electric field and the emission energy.

Previous reports considered energy shifts in the PL of individual CNTs as a result of mechanical stress [132]. However, energy shifts observed within our experiments were a factor of 100 bigger than those expected by the electrostatic pressure between the biased gates<sup>12</sup>. Thus, we exclude that the PL shifts were of mechanical origin.

Rather, we argue that applied electric field probes for the transversal polarizability

<sup>12</sup>CNTs embedded in a frozen water ambient show an energy shift due to external longitudinal stress [132]. Depending on their chirality the shift is either to the red *or* the blue with up to 12 meV/GPa. In contrast, the electrostatic pressure between the biased top and back gate acted only perpendicular to the CNT axes. We consider the work  $W$  to charge the capacitance in order to estimate the electrostatic pressure within our device.

$$W = \frac{1}{2} C V_g^2 = \frac{1}{2} \epsilon \epsilon_0 \frac{A}{d} V_g^2 . \quad (4.15)$$

With the force  $f = W/d$ , the pressure  $p$  is given by

$$p = \frac{f}{A} = \frac{1}{2} \epsilon \epsilon_0 \frac{V_g^2}{d^2} . \quad (4.16)$$

and does not exceed 3.7 MPa for a maximum voltage  $V_g^{\text{max}} = 30 \text{ V}$  and a minimal capacitor distance  $(d_1 + d_2)_{\text{min}} = 107 \text{ nm}$ . But even if we assume a similar energy shift due to perpendicular pressure as reported for longitudinal stress, this energy shift would not exceed a few tens  $\mu\text{eV}$  ( $\simeq 42 \text{ meV/GPa} \cdot 3.7 \text{ MPa}$ ). This is by about a factor 100 smaller than the here considered shifts of  $3.2 \text{ meV}$  ( $\beta \cdot F^2 \simeq -40 \text{ meV}(\text{GV}/\text{m})^2 \cdot (30 \text{ V}/107 \text{ nm})^2$ ).

#### 4. Tuning the photoluminescence with electric fields

of excitons. For type A CNTs the shift of the PL energy was best approximated by a parabolic function  $E(F) = E_{\text{PL}} + \beta(F - F_0)^2$  where  $E_{\text{PL}}$  is the PL energy at  $V_g = 0$ , and  $F_0 = V_0/(d_1 + d_2)$  accounts for local field modifications, e.g. due to the presence of a charge in the vicinity of the CNT. The fitting procedure yields local built-in fields of the order of  $\pm 0.1$  V/nm. This value is as big as the strength of the externally applied field and is consistent with the electric field strength of a single elementary charge impurity located as close as  $\sim 2$  nm to the CNT. This distance agrees well with rough estimations of the charge state density we evaluated from CV measurements. In this context, a random distribution of oxide charges in the dielectric medium would account for one charge state in a radius of 2.4 nm around a 200 nm CNT (see Chap. 4.2.3).

A summary of the fit parameter  $\beta$  is depicted in Fig. 4.13(b). Most type A CNTs exhibited field-induced redshifts with an average curvature of  $\beta = -40 \pm 20$  meV/(V/nm)<sup>2</sup>. However, we also identified insignificant shifts for three CNTs, which featured a high value of  $|F_0|$ . For those, the here generated homogeneous electric fields were insufficient to outperform local field modulations. Assuming that the energy dispersion of type A CNTs is entirely due to the quantum confined Stark effect, we interpret  $\beta$  as the transverse exciton polarizability. This is consistent with recent experimental [135] and theoretical [82] results for CNT excitons in perpendicular electric field as well as calculations of the transverse CNT polarizability based on tight-binding models [157–159] or first-principle approaches [160–162].

However, it should be taken into account that a blueshift due to field-induced doping [163] would counteract a redshift caused by the exciton polarizability whenever doping occurs. We could not identify such a blueshift for those CNTs that showed signatures consistent with the doping of excitons (discussed in Chap. 4.6).

#### 4.5.2. Permanent dipole moments

The energy dispersion changes drastically if we turn to type B CNTs as exemplified in Fig. 4.14. Their two-peaked spectra featured wide shifts of the emission energy of the bright exciton  $X$  and the satellite  $X^{\text{T}}$  as a function of the electric field  $F$ . Depending on the polarity of  $F$ , the PL energy was shifted to both the red *and* the blue exceeding for some CNTs  $\pm 10$  meV or several line widths.

Furthermore, the PL intensity was quenched as a function of the electric field  $F$ , which is illustrated in Fig. 4.14(c). Since this quenching was reversible on both emission peaks, we interpret this with PL energy shifts inducing misalignment of the excitation resonances with the excitation laser.

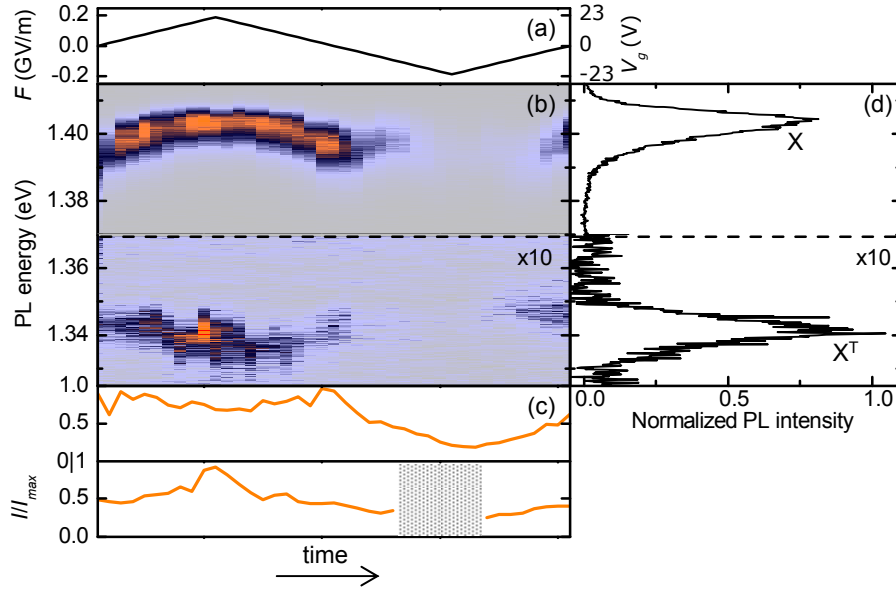


Figure 4.14.: **Permanent dipole moment of an individual CNT - part I:** (a) Electric field sweep. (b) Contour plot of the PL of an individual type B CNT showing distinctly field induced shifts on the bright exciton  $X$  and the triplet  $X^T$ . (c) Fitted PL intensity illustrating reversible quenching due to loss of resonance with the excitation laser (d) Spectrum at  $V_g = 20$  V.

Plotting the energy of the PL maxima as a function of  $V_g$  (Fig. 4.15(a)) revealed a linear energy shift and a negligible parabolic component, which we fit with  $E(F) = E_{\text{PL}} + pF$ . The presence of a transverse permanent dipole moment  $p$ , which gives rise to a linear Stark shift, is at first surprising since the  $C_2$  rotational symmetry (see Chap. 2.1.2) forbids pristine CNTs to carry such a permanent dipole moment.

Ab-initio calculations state a band-gap re-normalization for zig-zag and chiral CNTs with mono-vacancy defects [164,165]. Their band-gap is predicted to be modified linearly with the strength of a perpendicularly applied electric field. Sign and magnitude of the resulting energy shifts depend strongly on the orientation of the electric field to the remaining symmetry axis of the defective CNT. For (anti-)parallel orientation maximum energy shifts of  $|\Delta E/\Delta F| \simeq 0.63 \text{ e\AA}$  are expected where we scaled the reported theoretical values to the here considered CNT diameters. As depicted in Fig. 4.15 this agrees with our findings.

Despite this coincidence in  $\Delta E/\Delta F$ , this scenario is *not* applicable to the CNTs of our samples since it also implies a defect-induced band-gap reduction of the order of 50% at zero external field. Moreover, a general re-normalization of the band gap contradicts our findings of opposing energy shifts for the bright exciton and its

#### 4. Tuning the photoluminescence with electric fields

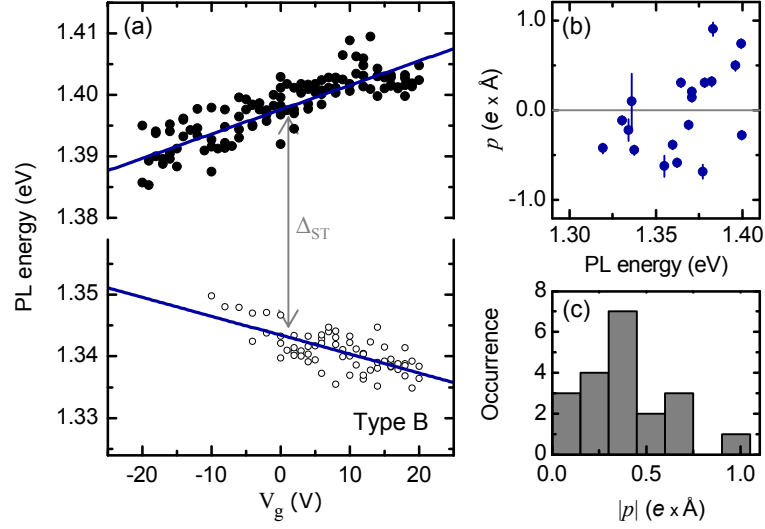


Figure 4.15.: **Permanent dipole moment of an individual CNT - part II:** (a) Energy of the PL maximum of the bright exciton peak  $X$  (filled circles) and triplet exciton peak  $X^T$  (open circles) as a function of the applied gate voltage. The permanent dipole moment equals the slope of the linear fits (solid blue lines) (b) Permanent dipole moment as a function of PL energy. (c) The histogram displays the distribution of the permanent dipole moment.

satellite in almost all type B CNTs, which is exemplified in Fig. 4.16(b). Instead of a band-gap re-normalization, we argue that defect-induced admixing of bright and dark excitons may give rise to built-in dipole moments that are a small fraction of the exciton Bohr radius  $p \simeq 0.01 \cdot a_B \cdot e$ . Indeed, built-in dipole moments were only present in type B CNTs, which were characterized by their state mixing between bright and dark exciton states. As we illustrated in Fig. 4.11 their two-peaked spectra could be interpreted as arising from admixing of triplet excitons to the bright exciton state.

Their opposing energy shifts can be interpreted as the anti-parallel alignment of the permanent dipole moments of singlet  $p_X$  and triplet exciton  $p_{X^T}$ . Further indication for a fundamental physical origin is illustrated in Fig. 4.16(a), which plots the magnitude of the observed singlet dipole moment  $p_X$  as a function of the degree of state mixing. This degree was quantified by the intensity ratio between the  $X^T$  and  $X$  emission peaks<sup>13</sup>. Since the magnitude of the dipole moment correlates with the degree of state mixing, both could be induced by defects, which give rise to spin-orbit coupling [78] and permanent dipole moments of excitons. Within our experiments

<sup>13</sup>Due to a not resolved mechanism some CNTs exhibited an intense emission from the  $X^T$  state and only faint emission from  $X$ . For simplicity we consider the *inverse* intensity ratio between  $X^T$  and  $X$  for those CNTs.

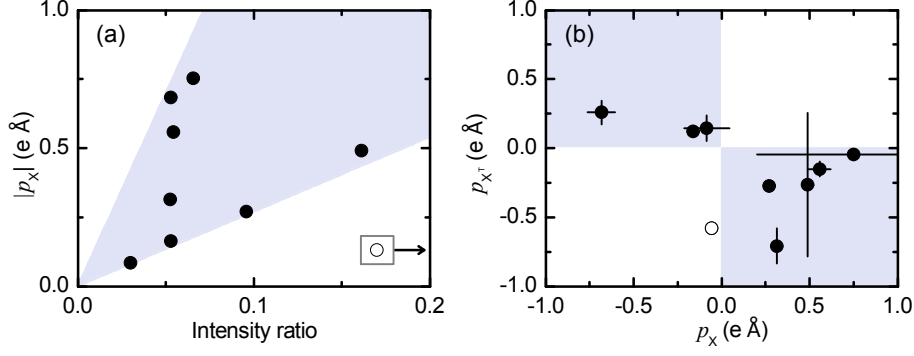


Figure 4.16.: **State mixing and permanent dipole moment:** (a) Magnitude of the permanent dipole moment  $|p_X|$  of the bright exciton state as a function of the degree of state mixing here quantified by the intensity ratio of  $X$  and  $X^T$ . (b) Permanent dipole moments of the triplet exciton state  $p_{X^T}$  and the bright excitons  $p_X$  are of opposite signs.

only one single CNTs disagrees with the above considered mechanism. Its dipole moments are depicted as open circles in Fig. 4.16.

However, the dipole moments observed here exhibit a transversal component, which cannot arise from mixing of exciton states from the  $E_{11}$  manifold. Rather, admixing to the  $E_{12}$  (or  $E_{21}$ ) manifold is required. Theoretical calculations show, that the energy bands even of pristine CNTs should reconfigure in transversal electric fields, although the band-gap is unaffected  $F < 0.3$  V/nm [166]. This is consistent with our findings of an only slightly varied PL energy of type A CNTs. Though a reconfiguration of the energy bands could admix singlet and triplet excitons from the  $E_{11}$  manifold to the  $E_{12}$  (or  $E_{21}$ ) manifold. In consequence, singlet and triplet excitons would acquire a permanent transversal dipole moment as they exhibited in a linear energy shift as a function of the transversal electric field.

In conclusion, we have identified CNTs with a broken symmetry featuring two-peaked PL emission profiles that arise from mixing dark and bright excitons states. By their energy splitting we could assign satellite peaks to the triplet exciton  $X^T$  or the phonon sideband of the k-momentum exciton  $X^K$ , respectively. In a transversal electric field, we observed linear, but opposing shifts on PL energy of bright and satellite PL emission, which we interpret with anti-parallel permanent dipole moments of both states. As states from the  $E_{11}$  exciton manifold do not intrinsically feature transversal dipole elements, the permanent dipole moments observed here could presumably arise from admixing of the  $E_{11}$  to the  $E_{12}$  (or  $E_{21}$ ) exciton manifold. However, a comprehensive understanding requires further theoretical and

#### 4. Tuning the photoluminescence with electric fields

experimental investigation. Nevertheless, due to the permanent dipole moment of CNTs with a broken symmetry - here termed as type B CNTs - their PL energy couples efficiently to external charge fluctuations. This broadens the line width of the PL emission profile (see Fig. 4.10) and increases spectral diffusion, which was reported in Ref. [134]

### 4.6. Emission from trion states

In conclusion of this chapter we focus on CNTs with a single emission line (type A). As we have shown previously, their PL energy varied only slightly with the applied electric field. However, some type A CNTs exhibited severe but reversible quenching of the PL intensity, which cannot be explained solely due to an off-resonant excitation. In addition, some type A CNTs featured the emergence of a satellite peak as a function of the applied field. As the energy splitting of the satellite to the bright excitons agrees with the trion energy splitting  $\Delta_{\pm}$ , it seems likely that this satellite originates from electric field mediated creation of trions in CNTs. In the last part of this chapter, we focus on a second quenching mechanism, which is presumably due to the variation of the trapping potential for localized excitons.

It appears that both characteristics could be attributed to charge states that were switchable by the external gate voltage and could dominate the photo-physics of individual CNTs. Within the MOS capacitor, these charge impurities were located in both the insulating oxide films (termed as  $Q_{OT}$ ) and on the oxide-semiconductor interface (termed as  $Q_{IT}$ ) and were apparent in the CV characteristic of the devices (see Chap. 4.2). However, charge impurities at the oxide-semiconductor interface were with 100 nm too far away from the CNTs to create a considerable field strength and inhomogeneity. In contrast, oxide charge states were located in close neighborhood to the CNTs. As we have stated before, we expect on average one charge state in a radius of 2.4 nm around a 200 nm CNT.

We begin with CNTs that showed the emergence of a satellite peak as a function of the applied gate voltage. Fig. 4.17(a) illustrates exemplarily a PL spectrum at  $V_g = 0$ . This consisted of a single asymmetric line X at  $\sim 1.36$  eV indicating emission from the bright exciton of an individual (6,4) CNT (comparison with [88]). When we ramped the gate voltage up to a positive voltage of  $V_g = 16$  V, the PL from the bright exciton was steadily quenched. The quenching of the bright exciton emission was accompanied by the emergence of a satellite peak  $X^{\pm}$  split by  $\Delta_{\pm} \simeq 100$  meV from the main PL resonance. In any case, the creation of this satellite peak was

robust and reversible. It came along with a quenching of the PL emission from the bright exciton.

The upper panel of Fig. 4.17(b) depicts the intensity of both emission peaks  $I_X$  and  $I_{X^\pm}$  as a function of the applied gate voltage<sup>14</sup>. As a typical feature for CNTs on substrate both emission lines showed pronounced intensity fluctuations. However,

<sup>14</sup>Only for this example,  $I_X$  was quenched also for negative voltages. This might originate from a delocalization process as discussed in the previous chapter. However, the occurrence of both quenching mechanisms was more a rare exceptional case and not reproduced by any other CNT.

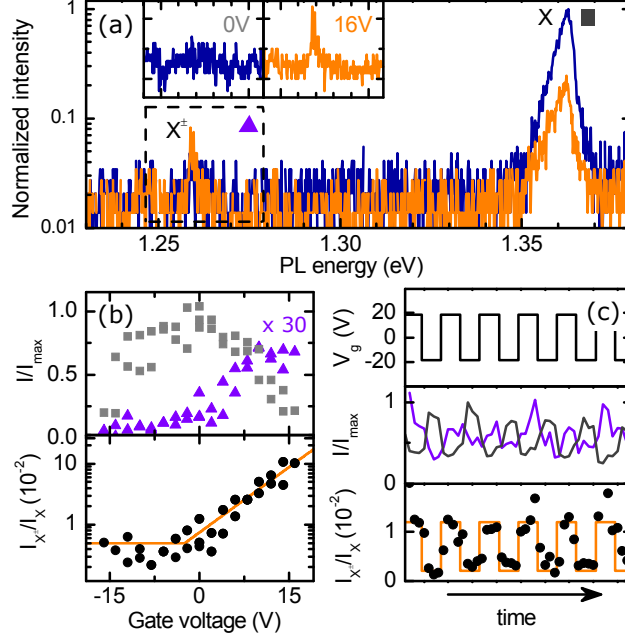


Figure 4.17.: **Voltage-induced trion generation in a single carbon nanotube:** The trion satellite  $X^\pm$  emerged for positive gate voltages redshifted by 100 meV with respect to the main emission peak at 1.36 eV (blue and orange spectra in (a) were recorded at 0 V and +16 V, respectively; the insets show zooms to individual spectra in the satellite peak region for given gate voltages). (b) Upper panel: The integrated PL intensity of the main peak  $I_X$  (grey data points) decreased for positive gate voltages whereas the intensity of the redshifted satellite  $I_{X^\pm}$  (purple data points, multiplied by a factor of 30) increases for positive and vanishes for negative voltages. Lower panel: The intensity ratio  $I_{X^\pm}/I_X$  on a log scale as a function of the gate voltage. As  $I_{X^\pm}/I_X$  featured a smoother trace,  $X$  and  $X^\pm$  were affected by the same intensity fluctuations. The orange solid line displays an exponential fit for  $V_g \geq -2.5$ . (c) The emission intensity was reversibly switched between minimum and maximum values when we applied a square wave voltage between -20 V and +20 V (grey and purple solid lines correspond to the peak intensity of the main resonance and the satellite, respectively). Data in (a-b) and (c) were measured on two different CNTs.

#### 4. Tuning the photoluminescence with electric fields

the ratio between both intensities  $I_{X^\pm}/I_X$  was less affected by these fluctuations, which indicates that both emission lines originated from the same CNT (lower panel in Fig. 4.17(b)).

Furthermore, we were able to perform a robust digital switching scheme between X and  $X^\pm$ , which is illustrated in Fig. 4.17(c) for a second CNT. We employed a square wave voltage scheme switching  $V_g$  between +20 V and -20 V (upper panel). Once again, the intensity ratio  $I_{X^\pm}/I_X$  followed the squares of the applied voltage.

Similar red-shifted satellites have been observed in recent experiments and attributed either to a band-gap re-normalization due to an oxygen substitute [48, 51] or to the formation of charged exciton complexes (trions) [47, 49, 50]. All reports included furthermore a quenching of the bright exciton intensity when these satellites emerged. As we will discuss now, the energy splitting between X and  $X^\pm$  agrees with these experimental reports and theoretical calculations [55, 81]. Thus, the emergence of  $X^\pm$  could originate from of CNT with an additional charge  $\pm e$ . This gives rise to the formation of trions while the X intensity is quenched in favor of PL emission from the trion peak  $X^\pm$ .

Fig. 4.18 summarizes the splitting  $\Delta_\pm$  of the reversibly created satellite peaks for type A CNTs and the splittings found on type B CNTs (see Chap. 4.4). In addition to the splitting to the triplet state  $\Delta_{\text{ST}}$  and the sideband of the k-momentum exciton  $\Delta_K + \hbar\omega_{\text{ph}}$  identified previously,  $\Delta_\pm$  constitutes a third class in the energy hierarchy of the exciton fine structure. We emphasize that all previous reports on the optical emission from trion states included particular screening effects. These were indispensable to bring the respective experimental results [47, 49] in agreement with the theoretical values for the trion binding energy predicted by Rønnow et al. [81]. Theoretical reference values for  $\Delta_\pm$  were presented in Chap. 2.3.6. However, newest theoretical considerations [167] predict that the trion binding energy is much less susceptible to Coulomb screening than anticipated by the general scaling of the Coulomb energies (Eq. 2.22). Thus, we neglected any screening effect on the trion binding energy, but re-scaled the fraction of the singlet-triplet exchange interaction to the environment ( $\epsilon = 4.6$ ). For all CNTs featuring emission from trion states we find energy splittings  $\Delta_\pm$  that agree with theoretical calculations.

Our findings add a new paradigm to the generation of trions in CNTs: their intensity can be controlled with a static electric field. As depicted in the lower panel in Fig. 4.17(b), the intensity ratio increased with the gate voltage. Whereas the PL emission spectra consisted of a single peak for  $V_g < 2.5$  V, the generation of trions set

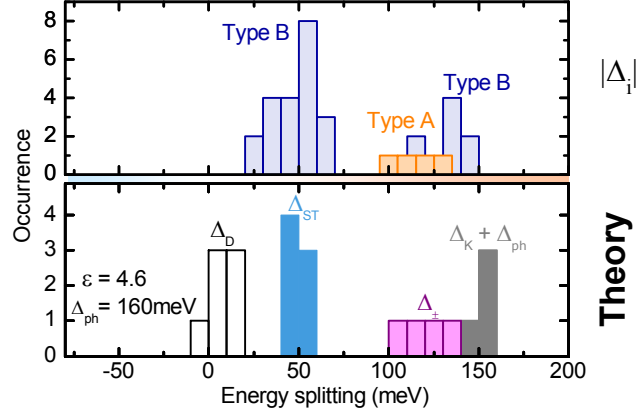


Figure 4.18.: **Complete hierarchy of low-energetic PL emission:** Upper panel: Experimentally confirmed energy splittings to the bright exciton line X for CNTs with broken symmetry (type B in orange) and electrically doped CNTs (type A in dark blue). Lower panel: Considering only chiralities with  $E_{\text{PL}}$  within the investigated spectral range, the histogram depicts theoretically predicted energy splitting to the bright exciton of the lowest dark exciton  $X^{\text{D}}$ , triplet exciton  $X^{\text{T}}$ , trion  $X^{\pm}$  and the phonon-sideband of the k-momentum exciton  $X^{\text{K}} + \Delta_{\text{ph}}$ .

in after this threshold and increased exponentially<sup>15</sup>. A simple exponential function, which is illustrated as a solid line, reproduces the variation of the intensity ratio  $I_{X^{\pm}}/I_X \propto \exp(V_g/6.1 \text{ V})$  with the applied gate voltage for  $V_g \geq 0$ . This could rather originate from the CNT charging process than being a feature of the trion state itself. In previous reports CNTs were either doped all optically [49] or by chemical adsorption of complex add-molecules [47]. Within our experiments trion states were presumably generated by tunneling of charges from a close source onto the CNTs. Oxide charge states or other impurities of the insulator could be possible sources. By varying the gate voltage, we would lower the tunnel barrier, which gives exponential rise of doping. This exponential increase agrees with the fundamental theoretical considerations of the WKB approximation for tunneling in quantum mechanics [168].

In summary, we have identified PL emission from all excitonic states of today's known fine structure - excepting the lowest dark exciton singlet state. Symmetry breaking mixes dark and bright exciton states and allows dipole-forbidden transitions, which brightens the exciton triplet  $X^{\text{T}}$ . Furthermore, we observed emission due to k-momentum states  $X^{\text{K}}$  in their phonon sidebands at  $\Delta_{\text{K}} + \hbar\omega_{\text{ph}}$ . Last but not least, we identified the generation of charged exciton complexes (trions) and their

<sup>15</sup>We also observed the emergence of trion peak with negative voltages. The polarity of trion generation can be understood in the arrangement of the charge impurity to the CNT. The offset of a few volts agrees with the built in fields of our devices, see Fig. 4.6.

#### 4. Tuning the photoluminescence with electric fields

emission lines  $X^\pm$ . These were induced via the applied electric field via tunneling of charges from a close oxide charge state. However, the small number of doped CNTs registered in our experiments indicate that such charge sources were rare in our devices. In future experiments devices with a reduced silicon oxide thickness would feature a defined tunnel barrier to the back gate. This could allow for tailored doping of individual CNTs.

### 4.7. Tuning the localization potentials of excitons

#### 4.7.1. Photoluminescence excitation spectroscopy

Photoluminescence excitation (PLE) spectroscopy is a powerful experimental technique that monitors the emission of a semiconducting material as a function of the excitation wavelength [136]. In the past, this technique was successfully employed on CNTs revealing many of their fundamental properties. It resolved the chirality distribution of a CNT ensemble by the ratio of the  $E_{11}$  emission resonance to the  $E_{22}$  excitation resonance [88]. Also the excitonic nature of photoluminescence was firstly revealed by PLE spectroscopy of individual CNTs [37]. However, at low temperature the excitation spectrum of an individual CNT is not solely determined by the electronic  $E_{22}$  resonance. Rather electron-phonon coupling establishes phonon-sidebands between the energy of the bright exciton ( $\simeq E_{11}$ ) and  $E_{22}$  [83–87]. Actually, phonon-assisted excitation has been identified as efficient as excitation via electronic  $E_{22}$  states [83]. Typically, these sidebands occur at the major phonon modes of a CNT, which are namely the radial breathing mode (RBM), the graphene modes ( $G^\pm$ ) and the disorder mode (D). This last mode arises from vibration of non-hexagonal carbon rings including many lattice defects like vacancies, 5-7 defects and Stone-Walsh defects [169].

We define the laser detuning  $\delta_L$  as the difference between the excitation laser energy and the PL emission energy:

$$\delta_L = E_{exc} - E_{PL} . \quad (4.17)$$

For recording of PLE spectra, we excited individual CNTs with a continuous excitation beam - polarized parallel to the CNT axis and operated at constant intensity  $\simeq 10 \mu\text{W}/\mu\text{m}^2$ . By systematic variation of the laser wavelength, we shifted the laser detuning  $\delta_L$  in steps of 0.75 meV in a range between 30 to 300 meV and recorded an emission spectra after every step. We used a standard fitting routine that fit a

Lorentzian peak to the PL emission spectra and gave a reliable measure of the PL intensity. A PLE spectrum plots this integrated PL intensity as a function of the laser detuning  $\delta_L$ .

For all investigated CNTs the PLE spectra exhibited pronounced variations of the integrated PL intensity and featured excitation resonances where the PL intensity showed a local maximum. For many investigated CNTs the energy detuning at these maxima coincided with the energy of phonon-modes, e.g. RBM, D,  $G^\pm$ . These findings agree with an excitation mechanism via phonon-assisted sidebands reported previously [83–87].

However, some CNTs showed resonances at characteristic detunings that disagree with the phonon spectrum. Fig. 4.19 exemplarily depicts PL and PLE spectrum of such an individual CNT. This CNT was located on the sample next to the actual capacitor and was covered only by an aluminium oxide layer. As typical for a type A CNT, its PL spectrum consisted of a single asymmetric emission line at  $E_{PL} = 1.288$  meV. Its PLE spectrum featured several broad resonances, which included a striking phonon-sideband due to the RBM mode but showed only small signatures of other common phonon-assisted sidebands (D,  $G^\pm$  modes). Especially

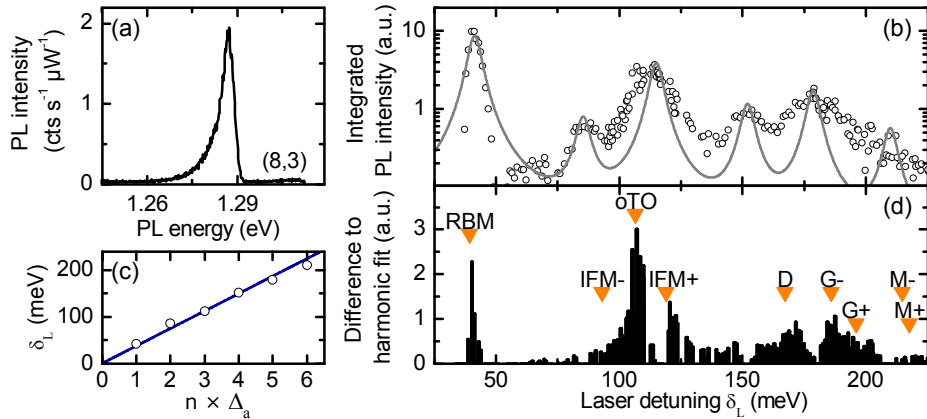


Figure 4.19.: **Photoluminescence excitation spectra revealing exciton localization:** (a) Spectra of an individual CNT with chirality (9,1) continuously excited at 880 nm, which equals a laser detuning  $\delta_L \simeq 130$  meV. (b) Integrated PL intensity as a function of laser detuning  $\delta_L$  reveals an excitation spectra dominated by a harmonic localization potential *and* phonon-assisted sidebands. The grey solid line depicts a fit of six Lorentzian peaks with equal width  $\Gamma_a = 5.8$  meV. (c) The central energies of these peaks were equidistant, which indicates a harmonic trapping with a fundamental localization energy  $\Delta_a = 37.4$  meV. (d) The difference between fit and experimental data coincides with a number of phonon energies, which are reported [170].

#### 4. Tuning the photoluminescence with electric fields

the excitation resonance around 110 meV disagrees with the energy of phonons in CNTs.

As we will discuss now, such PLE spectra could originate from an alternate excitation mechanism, which occurs in addition to the phonon-sideband assisted excitation of excitons in cryogenic CNTs. As exemplified by the solid line in Fig. 4.19(b), we were able to reproduce most of the PLE spectra by fitting (here six) Lorentzian peaks of equal width. Subtracting these Lorentzians from the PLE gave a "reduced excitation spectrum".

For the here exemplified CNT, this reduced excitation spectrum is depicted in Fig. 4.19(d) and local maxima could be assigned to phonon sidebands [170]. Most intense peak at 40.3 meV was clearly assigned to the RBM mode as this value agrees with the theoretical prediction of 40.6 meV of a (9,1) CNT [171]. However, the expected PL energy of a (9,1) CNT [88] disagrees with the here observed  $E_{\text{PL}} = 1.288$  eV, which is shifted by  $\Delta E = 54$  meV to the red. This energy scale is identical to the temperature induced energy shifts, which we presented in Chap. 3.

The second dominant phonon sideband was the out-of-plane transverse optical (oTO) phonon mode. Also its overtones ( $M^\pm$ ) were visible [172]. The occurrence of an oTO phonon mode is even more remarkable since the mirror symmetry of graphene forbids effective optical coupling to this phonon mode [172]. However, coupling to the oTO mode is associated with out-of-plane discontinuities in graphene [173]. Here, this discontinuity could be a chemically adsorbed aluminium atom (the CNT was covered by aluminium oxide). By forming an AlC<sub>2</sub> bond, the Al atom would be located outside the CNT shell [174] giving rise to out-of-plane vibrational modes. Indeed, the energy of the vibrational rocking mode of AlC<sub>2</sub> coincides with the here observed energy of 105 meV [175].

However, the greater share of the excitation spectrum was not governed by phonon resonances but dominated by six Lorentzian shaped peaks. At first glance, the fitting of Lorentzians peaks of equal width may appear as arbitrary. Nevertheless, the central energies of these peaks could be assigned as the first to the sixth multiple of a fundamental energy  $\Delta_a = 37.4$  meV as illustrated in Fig. 4.19(c). Thus, it can be interpreted as the six harmonics of an exciton localized in an harmonic trapping potential. Analogous quantum dot like signatures of a fundamental localization energy  $\Delta_a$  and its harmonics were apparent for many investigated CNTs. As we will demonstrate in the following chapter, the relaxation of higher excited excitons becomes particularly efficient by coupling to phonons. For the here discussed CNT, harmonic resonances were intensified when they coincide with phonons as it is the

case for the first (agrees with RBM mode) and the fourth (agrees with the oTO mode) harmonics.

In conclusion, our findings indicate the existence of an excitation mechanism for localized excitons. Similar to solid-states quantum dots [176,177], excitation via higher states of the localized excitons was highly efficient, exceeding the effect of electron-phonon coupling (phonon sidebands). In previous studies this might have been suppressed by rigorous pre-selection, which concentrates on CNTs with symmetric emission spectra [83].

#### 4.7.2. Tuning excitation resonances with the gate voltage

We recorded PLE spectra as a function of  $V_g$ . As we will now discuss, these revealed a variation of the localization potential  $\Delta_a$  and support the hypothesis of the here identified excitation mechanism. Further, it allowed us to understand the reversible quenching of the PL intensity as a function of the gate voltage  $V_g$ , which we observed for many type A CNTs. A theoretical model that is capable to reproduce both the excitation spectrum *and* the quenching of PL is included in Appendix D. It shall be exemplified here for the same CNT depicted in Fig. 4.12, which exhibited reversible quenching of PL for negative gate voltages.

In agreement with our findings depicted in Fig. 4.19, the PLE spectra of this CNT featured equidistant excitation resonances. All PLE spectra could be reproduced with Lorentzian shaped peaks that are illustrated by solid lines in Fig. 4.20(a). The peak width  $\Gamma_a$  was set to be identical for all peaks within a spectrum. Apparently, the shape of the excitation spectra varied with  $V_g$  as exemplified for three different gate voltages of 10 V, -10 V, and -20 V, respectively. In analogy to the previous discussion and exemplified in Fig. 4.20(b), we find the peak centers at multiple values of the fundamental localization potential  $\Delta_a$ . However, these modulations occurred only due to the variation of the electric field. For a constant gate voltage - and thus for the duration for measuring a single PLE spectrum - the localization energy  $\Delta_a$  was stable up to <2 %. As illustrated by the blue shaded area in Fig. 4.20(d), we could robustly repeat the variation of  $\Delta_a$  as a function of the gate voltage  $V_g$  within narrow limits.

However, the energies of mechanical (phonon) modes were well investigated by Raman spectroscopy and identified as insensitive to external disturbances [178]. Thus, we can exclude that the here presented characteristic arises from manipulated phonon energies that vary with the external electric field.

Rather, it is likely that this CNT is dominated by the previously identified ex-

#### 4. Tuning the photoluminescence with electric fields

citation mechanism of a localized exciton. In this context, the central energies of these peaks could be interpreted as the harmonics of a fundamental local localization energy  $\Delta_a$ . Theoretical calculations show that inhomogeneous electric fields, and in particular charge impurities [62], can create a sufficient localization potential for excitons in CNTs [179]. Within the here considered MOS capacitor devices, oxide charge states located in the dielectric medium close to the CNTs could provide for such inhomogeneous electric fields. As discussed in Chap. 4.2, these oxide charges were switchable by means of the externally applied electric field.

This model is sketched in Fig. 4.20(e) for an oxide charge state with an electric field dependent distance  $a$  to the CNT. A small (big) distance  $a_{\min}$  ( $a_{\max}$ ) can be associated with a stiff (smooth) localization potential. On the base of theoretical considerations [62], the localization potentials can be identified with an oxide charge impurity as close (far) as  $a_{\min}=4 \text{ \AA}$  ( $a_{\max}=7 \text{ \AA}$ ) from the CNT.

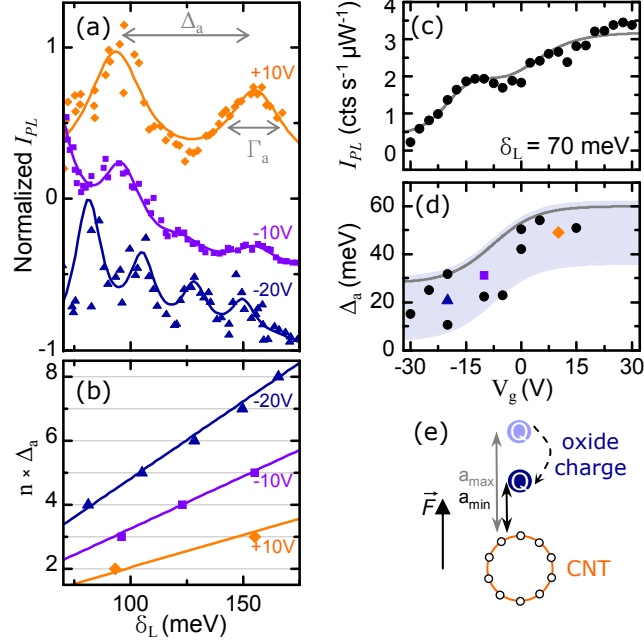


Figure 4.20.: **Variation of the exciton localization by the electric field:** (a) Photoluminescence excitation spectra of an individual CNT for three different gate voltages  $V_g = 10, -10$  and  $-20$  V. (b) Fitted resonances (filled diamond, square and triangle) for the three PLE spectra reveal that the localization potential  $\Delta_a$  of a harmonic oscillator was varied by  $V_g$ . (c) PL intensity as a function of  $V_g$  for a fixed excitation energy. The solid line depicts is based on our model presented in Appendix D. (d) The localization potential was robustly switched between a low value for negative voltages and a stiff localization for positive voltages. The solid line depicts is based on our model presented in Appendix D.

#### 4.7. Tuning the localization potentials of excitons

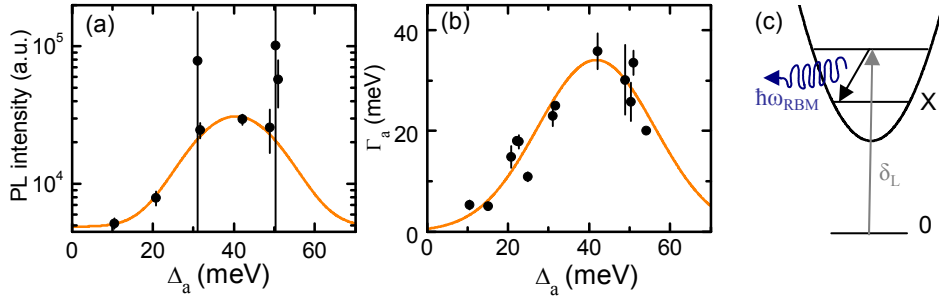


Figure 4.21.: **Phonon bottleneck:** (a) PL intensity as a function of the localization potential  $\Delta_a$  for excitation via the second harmonic  $\delta_L = 2 \cdot \Delta_a$ . The solid line displays a fit of a Gaussian that peaks at 40.5 meV. This value accords to the energy of the radial breathing mode RBM. (b) Line-width  $\Gamma_a$  of the excitation resonances as a function  $\Delta_a$ . The solid line displays a Gaussian fit. (c) Mechanism for relaxation of excited exciton states by coupling to phonon modes.

Apart from the harmonic trapping potential we identified another striking analogy to zero-dimensional quantum dots [137]: In the here considered CNT higher excited excitons were efficiently relaxed by coupling to phonon. In one- (or higher-) dimensional semiconductors phonons efficiently relax excited electronic states. However, in quantum dots this relaxation is inhibited when the energy splitting between an excited exciton state differs from the energy of the respective phonon modes, which is termed as a phonon-bottleneck [180].

In detail, Fig. 4.21(a) displays the PL emission intensity for excitation via the second harmonic ( $\delta_L = 2 \cdot \Delta_a$ ) as a function of the localization potential  $\Delta_a$ . It reveals a Gaussian distribution that peaks at  $\Delta_a^* = (40.5 \pm 2.6)$  meV. An analogous behavior can be identified for the width of the excitation resonances  $\Gamma_a$  with its maximum around the same value of  $(41.7 \pm 1.0)$  meV as illustrated in Fig. 4.21(b). Apparently, excitation and relaxation of excitons becomes highly efficient for such trapping potential. Indeed, the maximum  $\Delta_a^*$  agrees with the energy of the radial breathing mode  $\hbar\omega_{\text{RBM}}$  of a CNT with a diameter of  $(0.689 \pm 0.017)$  nm [171]. In summary, the PL of localized excitons in individual CNTs is maximized when the the harmonic localization potential is tuned to the energy of a phonon mode. These findings suggest that the relaxation of excited exciton states is driven by phonons. Fig. 4.21(c) sketches this model, which is indicative for a phonon-bottleneck reported on solid-state quantum dots [137]. Already the discussion summarized in Fig. 4.19 identified a highly efficient exciton relaxation by means of exciton-phonon coupling.

#### 4. Tuning the photoluminescence with electric fields

The central role of phonons for the dephasing of electronic states was theoretically predicted also for CNTs [181].

On the basis of our findings, we developed a model for the excitation of excitons in this specific CNT quantum dot. It is discussed at full length in Appendix D. Illustrated by the grey solid lines in Fig. 4.20 it is capable to link the quenching of the PL intensity in a voltage sweep (c) to the variation of the localization potential (d).

Against the previous discussion we emphasize that the harmonic exciton states did not feature any anharmonic signatures, even for the highest harmonics of  $n = 8$ . As the typical depth of a trapping potential, which we identified via the redshift of the PL energy, was on the same order of magnitude as  $\Delta_a$ , an anharmonic compression of the harmonic ladder would be expected already for  $n = 3$  in Fig. 4.20(b). Furthermore, the mechanism of phonon mediated relaxation is inconsistent for relaxation with  $\Delta n = 2, 3, \dots$ . This would be apparent in broad and intense resonances also for PLE spectra with  $2 \cdot \Delta_a = \hbar\omega_{\text{RBM}}$  for the here exemplified CNT. However, the fitting routine employed here reproduced the excitation spectra best when the Lorentzian peaks were of the same width within a spectrum.

In conclusion, we can state that the excitation spectra of individual CNTs at cryogenic temperatures could be dominated by resonances, which disagree with phonon sidebands. Within a spectrum these resonances could be associated to the multitudes of a fundamental energy scale on the order of  $\sim 10 - 50$  meV. In a single-shot experiment on a type A CNT embedded in the MOS capacitor device we were able to vary these resonances by means of the external electric field. This variation was reversible and could be interpreted as the variation of the fundamental trapping potential for localized excitons. However, the higher harmonics of the trapping potential did not feature any signatures that indicate for an anharmonicity as it would be essential for quantum dots. Although the relaxation of higher harmonic exciton states was highly efficient when the harmonic ladder was in resonance with the phonon energy  $\hbar\omega_{\text{RBM}}$ , the observed excitation spectra cannot be fully understood in terms of a phonon-bottleneck. Further experimental investigations are crucial for a deeper understanding of the here considered excitation of localized excitons.

## 5. Photon emission statistics

The realization of many proposed schemes for optoelectronic [29] application of CNTs in quantum information processing [182] or spintronics [183] are hindered by rapid decoherence of excitonic states due to nonradiative quenching [73], intermittency [77] or environmental dephasing [184]. As we recently reported [127], many of these issues could be overcome by localization of excitons. Although we have identified many indications for exciton localization in cryogenic CNTs, as-grown suspended CNTs are highly isolated from their environment and feature few, but well-defined defects. By analogy with nitrogen vacancy color centers in diamond lattices [185], they constitute a new class of quantum-dots in CNTs. This class exhibits unique, hitherto unrivaled optical properties like narrow line width and long exciton lifetime. Both were documented in spectral and time resolved measurements and compared with our used standard material of CoMoCat CNTs. Even on the shortest time scales PL emission from as-grown suspended CNTs lacks of any signature of intermittency or shelving to the lowest energetic dark exciton state, while featuring a significantly increased quantum yield.

## 5.1. Theoretical introduction

The second-order correlation function  $g^{(2)}(\tau)$  allows to characterize the intensity coherence of a light beam. In this framework we consider the photon statistics of an emitter showing discrete intensity fluctuations - termed as intermittency or blinking. For such an emitter, the photon emission rate is determined by the emitter's respective "intensity state". The number of photons emitted in any given time interval  $\tau$  is not statistically independent from the number emitted shortly before. Rather bunching of photons becomes dominant.

In contrast, a two-level system, which emits light as a result of spontaneous decay, shows anti-bunching of photons. Since the system must first be re-excited before it can emit a second photon, it emits only one single photon at once. Both processes will apply for CNTs in our experiments. The time scales for the radiative decay (typically a few 100 ps up to 5 ns) and the scales for blinking (typically a few 100 ns) differ so that both can be treated independently.

Here, we study both cases in a probabilistic rather than in a quantum optical context. For a proper quantum mechanical treatment of the optics of two-level systems we refer to Ref. [186].

### 5.1.1. Second-order correlation function

We shall now consider a monochromatic light beam with a cross section area  $\mathfrak{A}^1$  or more precisely a chain of indistinguishable photons with the energy  $\hbar\omega$ . If we divide the beam into sections of equal length, we find a specific number of photons  $\mathbf{n}_i$  in every section  $i$  of length  $c \cdot \tau$  - where  $c$  denotes the speed of light and we assume a beam propagating in vacuum. The mean photon number per section  $\bar{n}$  is then given by the ratio of the average beam intensity  $I$  and the photon energy  $\hbar\omega$ :

$$\bar{n} = \frac{I \mathfrak{A} \tau}{\hbar\omega} . \quad (5.1)$$

The standard deviation  $\Delta \mathbf{n}$  of the average  $\bar{n}$  measures [187]

- $\Delta \mathbf{n} = \sqrt{\bar{n}}$  for a beam of randomly distributed photons where the number of photons per section  $\mathbf{n}$  obeys **Poissonian statistic**.
- $\Delta \mathbf{n} > \sqrt{\bar{n}}$  for beams with fluctuating intensity where the standard deviation  $\Delta \mathbf{n}$  is increased - thus  $\mathbf{n}$  obeys **super-Poissonian statistic**.

---

<sup>1</sup>We omit the Gaussian beam profile.

- $\Delta n < \sqrt{n}$  for a beam with well-ordered photon-distribution. This **sub-Poissonian statistic** is not found in classical light beams.

The second-order correlation function  $g^{(2)}(\tau)$  quantifies intensity fluctuations of a light beam or its intensity coherence. It is defined as [188]<sup>2</sup>:

$$g^{(2)}(\tau) = \frac{\langle \mathbf{n}(t)\mathbf{n}(t+\tau) \rangle}{\langle \mathbf{n}(t) \rangle \langle \mathbf{n}(t+\tau) \rangle} \quad (5.2)$$

where  $\langle \mathbf{n}(t) \rangle$  is the time average given by

$$\langle \mathbf{n}(t) \rangle = \int_{-\infty}^{\infty} dt \mathbf{n}(t) \quad . \quad (5.3)$$

For an "infinitely long" beam it obviously holds true that  $\langle \mathbf{n}(t) \rangle = \langle \mathbf{n}(t+\tau) \rangle \propto I$ . However, the numerator  $\langle \mathbf{n}(t)\mathbf{n}(t+\tau) \rangle$  deserves closer study. It denotes the expected product of the photon numbers in two sections, which are separated by the length  $c \cdot \tau$ .

If the number of photons  $\mathbf{n}$  obeys Poissonian statistics, the number of photons in a specific section is statistically independent from the number in any other section. Thus, we can write the numerator as a product  $\langle \mathbf{n}(t)\mathbf{n}(t+\tau) \rangle = \langle \mathbf{n}(t) \rangle \langle \mathbf{n}(t+\tau) \rangle$  and obtain  $g^{(2)}(\tau) = 1$ .

In the following, we will study in detail both a light source with super-Poissonian statistics and a source with sub-Poissonian statistics. Due to the bunching of photons in a beam with super-Poissonian statistics, the photon number  $\mathbf{n}(t+\tau)$  is positively correlated with  $\mathbf{n}(t)$  and thus  $\langle \mathbf{n}(t)\mathbf{n}(t+\tau) \rangle \geq \langle \mathbf{n}(t) \rangle \langle \mathbf{n}(t+\tau) \rangle$ . We will show that this holds true for an emitter that fluctuates between two discrete intensity states. In contrast, for a beam with sub-Poissonian statistics we find  $\mathbf{n}(t+\tau)$  negatively correlated with  $\mathbf{n}(t)$  and thus  $\langle \mathbf{n}(t)\mathbf{n}(t+\tau) \rangle \leq \langle \mathbf{n}(t) \rangle \langle \mathbf{n}(t+\tau) \rangle$ . As we will show later, this is the case for a driven two-level system.

---

<sup>2</sup>"This is the intensity analogue to the first order correlation function  $g^{(1)}$  that determines the visibility of interference fringes." (Credits [187]).

## 5. Photon emission statistics

In summary for the three itemized statistical distributions, we expect for the second-order correlation function at  $\tau = 0$

- $g^{(2)}(0) = 1$  for a perfectly **coherent light** beam.
- $g^{(2)}(0) > 1$  for a beam obeying super-Poissonian statistics. This is generally denoted as **bunched light**.
- $g^{(2)}(0) < 1$  for a beam obeying sub-Poissonian statistics. This is generally denoted as **anti-bunched light**.

### 5.1.2. Blinking and intermittency

We start out with a blinking light source, whose intensity fluctuates between two discrete intensity states  $I_1$  and  $I_2$ . We assume a probabilistic two-state process, i.e. the emitter *changes* its emission state  $I_1 \leftrightarrow I_2$  independently from its previous history. Due to its similarity to Morse signals this is also called "telegraph noise". We define the rate for leaving the state  $I_1(I_2)$  with  $\gamma_1(\gamma_2)$ . The probability density is then given by

$$P(X \in \{I_1, I_2\}, t) = p_1(t)\delta(X - I_1) + p_2(t)\delta(X - I_2) , \quad (5.4)$$

which uses the Dirac delta-function  $\delta(x)$ . The probability  $p_{1(2)}$  is determined by the master equation [189]

$$\frac{\partial}{\partial t} p_1(t) = \gamma_2 p_2(t) - \gamma_1 p_1(t) \quad (5.5a)$$

$$\frac{\partial}{\partial t} p_2(t) = \gamma_1 p_1(t) - \gamma_2 p_2(t) . \quad (5.5b)$$

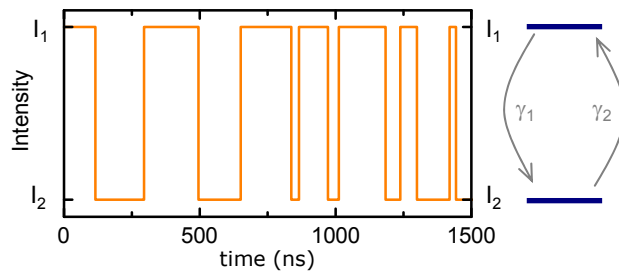


Figure 5.1.: **Blinking** of an emitter between two discrete "intensity states"  $I_1$  and  $I_2$  ("telegraph noise"). On the right: Illustration of rate  $\gamma_1$  ( $\gamma_2$ ) for leaving state  $I_1$  ( $I_2$ ).

With the use of arbitrary initial conditions  $p_1(t=0)$  and  $p_2(0) = 1 - p_1(0)$ , we find a probability function that solves this partial differential equation<sup>3</sup>

$$\begin{aligned} p_1(t) &= \frac{\gamma_2}{\gamma_1 + \gamma_2} + \left[ p_1(0) - \frac{\gamma_2}{\gamma_1 + \gamma_2} \right] e^{-(\gamma_1 + \gamma_2)t} \\ p_2(t) &= \frac{\gamma_1}{\gamma_1 + \gamma_2} - \left[ p_1(0) - \frac{\gamma_2}{\gamma_1 + \gamma_2} \right] e^{-(\gamma_1 + \gamma_2)t} . \end{aligned} \quad (5.6)$$

For a long time  $t$  the probabilities  $p_1(t)$  and  $p_2(t)$  converge to the steady-state probabilities:

$$\begin{aligned} p_1^{\text{inf}} &= \lim_{t \rightarrow \infty} p_1(t) = \frac{\gamma_2}{\gamma_1 + \gamma_2} \\ p_2^{\text{inf}} &= \frac{\gamma_1}{\gamma_1 + \gamma_2} . \end{aligned} \quad (5.7)$$

Assuming the emitter is initialized in state  $I_1$  - so  $p_1(t=0) = 1$  - we can now determine the conditional probabilities to find it in  $I_1$  ( $I_2$ ) after a time delay  $\tau$ . Obviously this is invariant under time reversal  $\tau \rightarrow -\tau$  and we can set  $\tau \rightarrow |\tau|$ :

$$\begin{aligned} p_{1|1}(\tau) &= \frac{\gamma_2}{\gamma_1 + \gamma_2} + \frac{\gamma_1}{\gamma_1 + \gamma_2} e^{-(\gamma_1 + \gamma_2)|\tau|} \\ p_{2|1}(\tau) &= \frac{\gamma_1}{\gamma_1 + \gamma_2} - \frac{\gamma_1}{\gamma_1 + \gamma_2} e^{-(\gamma_1 + \gamma_2)|\tau|} . \end{aligned} \quad (5.8a)$$

---

<sup>3</sup>Exemplarily, we show that this solves the differential equation (5.5a):

$$\begin{aligned} \gamma_2 p_2(t) - \gamma_1 p_1(t) &\stackrel{(5.6)}{=} + \gamma_2 \left\{ \frac{\gamma_1}{\gamma_1 + \gamma_2} - \left[ p_1(0) - \frac{\gamma_2}{\gamma_1 + \gamma_2} \right] e^{-(\gamma_1 + \gamma_2)t} \right\} \\ &\quad - \gamma_1 \left\{ \frac{\gamma_2}{\gamma_1 + \gamma_2} + \left[ p_1(0) - \frac{\gamma_2}{\gamma_1 + \gamma_2} \right] e^{-(\gamma_1 + \gamma_2)t} \right\} \\ &= \left[ -\gamma_2 p_1(0) - \gamma_1 p_1(0) + \frac{\gamma_2 \gamma_2}{\gamma_1 + \gamma_2} + \frac{\gamma_1 \gamma_2}{\gamma_1 + \gamma_2} \right] e^{-(\gamma_1 + \gamma_2)t} \\ &= \left[ -p_1(0)(\gamma_1 + \gamma_2) + \frac{\gamma_2(\gamma_1 + \gamma_2)}{\gamma_1 + \gamma_2} \right] e^{-(\gamma_1 + \gamma_2)t} \\ &= -(\gamma_1 + \gamma_2) \left[ p_1(0) - \frac{\gamma_2}{\gamma_1 + \gamma_2} \right] e^{-(\gamma_1 + \gamma_2)t} = \frac{\partial}{\partial t} p_1(t) . \end{aligned}$$

And fulfills the initial conditions

$$\begin{aligned} p_1(t=0) &= \frac{\gamma_2}{\gamma_1 + \gamma_2} + \left[ p_1(0) - \frac{\gamma_2}{\gamma_1 + \gamma_2} \right] = p_1(0) \\ p_2(t=0) &= \frac{\gamma_1}{\gamma_1 + \gamma_2} - \left[ p_1(0) - \frac{\gamma_2}{\gamma_1 + \gamma_2} \right] = 1 - p_1(0) = p_2(0) . \end{aligned}$$

## 5. Photon emission statistics

Correspondingly for initialization in  $I_2$  or  $p_2(0) = 1$ , we find

$$\begin{aligned} p_{1|2}(\tau) &= \frac{\gamma_2}{\gamma_1 + \gamma_2} - \frac{\gamma_2}{\gamma_1 + \gamma_2} e^{-(\gamma_1 + \gamma_2)|\tau|} \\ p_{2|2}(\tau) &= \frac{\gamma_1}{\gamma_1 + \gamma_2} + \frac{\gamma_2}{\gamma_1 + \gamma_2} e^{-(\gamma_1 + \gamma_2)|\tau|} . \end{aligned} \quad (5.8b)$$

The expectation values  $\langle I(t)I(t + \tau) \rangle$ ,  $\langle I(t) \rangle$  and  $\langle I(t + \tau) \rangle$  can now be evaluated explicitly. Since we assumed that the emitter can take only two discrete intensity states, we just sum up the products of all possible combinations of  $I_i$  and their respective probabilities:

$$\begin{aligned} \langle I(t)I(t + \tau) \rangle &= \sum_{i,j=1,2} p_j^{\text{inf}} I_j p_{i|j}(\tau) I_i \\ \langle I(t) \rangle &= \langle I(t + \tau) \rangle = \sum_{i=1,2} p_i^{\text{inf}} I_i \end{aligned} \quad (5.9)$$

By using the explicit conditional and steady-state probabilities from Eq. (5.7) and (5.8), we find the second order correlation function  $g^{(2)}(\tau)$  of a blinking emitter with

$$g^{(2)}(\tau) = \frac{\langle I(t)I(t + \tau) \rangle}{\langle I(t) \rangle \langle I(t + \tau) \rangle} = 1 + \frac{\gamma_1 \gamma_2 (I_1 - I_2)^2}{(\gamma_1 I_2 + \gamma_2 I_1)^2} e^{-(\gamma_1 + \gamma_2)|\tau|} . \quad (5.10)$$

This expression simplifies further, if we consider an emitter, which switches between the two states "on" and "off". This behavior is commonly denoted as emission intermittency and occurs in the PL of many single molecule or low-dimensional systems [190]. We set  $I_{\text{off}} = 0$  and obtain

$$g^{(2)}(\tau) = 1 + \frac{\gamma_{\text{on}}}{\gamma_{\text{off}}} e^{-(\gamma_{\text{on}} + \gamma_{\text{off}})|\tau|} . \quad (5.11)$$

Finally, we define the time constants  $\tau_i = \gamma_i^{-1}$  and find an expression, which was previously reported in the context of blinking quantum dots [89]

$$g^{(2)}(\tau) = 1 + \frac{\tau_{\text{off}}}{\tau_{\text{on}}} e^{-\left(\frac{1}{\tau_{\text{on}}} + \frac{1}{\tau_{\text{off}}}\right)|\tau|} . \quad (5.12)$$

### 5.1.3. Single photon emitters

In the preceding considerations a system emitted many photons depending on its "intensity state". We now focus on the emission process itself. Therefore, we modify the model to analyze the photon emission from a two-level system driven by continuous excitation, i.e. by a laser beam.

### A driven two-level system

We transform the former states  $I_1$  to the ground state  $|g\rangle$  and  $I_2$  to the excited state  $|e\rangle$ . In contrast to the preceding problem, light is only emitted as a single photon during the transition  $|e\rangle \rightarrow |g\rangle$  that happens on a characteristic time  $\tau_0$ . The system is re-excited  $|g\rangle \rightarrow |e\rangle$  for instance by laser excitation. The mean intensity  $\langle I(t) \rangle$  is then equivalent to the expected number of emitted photons. This number is solely determined by the steady-state probability  $p_{|e\rangle} = p_2^{\text{inf}}$  for the two-level system being in the excited state  $|e\rangle$ :

$$\langle I(t) \rangle = p_{|e\rangle} \stackrel{(5.7)}{=} \frac{\gamma_1}{\gamma_1 + \gamma_2} . \quad (5.13)$$

The same holds true for  $\langle I(t + \tau) \rangle$ .

Referring now to  $\langle I(t)I(t + \tau) \rangle$ : As a prerequisite for emission of a photon and a non-vanishing intensity  $I(t)$ , the system must be in the excited state  $|e\rangle$  at a particular instant of time  $t$ . This probability is again given by the steady-state probability  $p_{|e\rangle}$ . At  $t$  the system decays instantaneously to the ground state  $|g\rangle$  by emitting a photon. The probability for emitting a second photon at  $t + \tau$  is given by the conditional probability  $p_{|e\rangle||g\rangle}(\tau) = p_{2|1}(\tau)$ . Thus, we can write:

$$\langle I(t)I(t + \tau) \rangle = p_{|e\rangle} p_{|e\rangle||g\rangle}(\tau) \stackrel{(5.7),(5.8)}{=} \left( \frac{\gamma_1}{\gamma_1 + \gamma_2} \right)^2 (1 - e^{-(\gamma_1 + \gamma_2)|\tau|}) . \quad (5.14)$$

Using both expressions, the second-order correlation function  $g^{(2)}(\tau)$  for a driven two-level system reads as

$$g^{(2)}(\tau) = \frac{\langle I(t)I(t + \tau) \rangle}{\langle I(t) \rangle \langle I(t + \tau) \rangle} = \frac{\left( \frac{\gamma_1}{\gamma_1 + \gamma_2} \right)^2 (1 - e^{-(\gamma_1 + \gamma_2)|\tau|})}{\left( \frac{\gamma_1}{\gamma_1 + \gamma_2} \right)^2} = 1 - e^{-\frac{|\tau|}{\tau_0}} . \quad (5.15)$$

This holds true as long as we consider only spontaneous emission from the excited state to the ground state, which is always the case in our experiments. Here, the spontaneous emission time  $\tau_0$  equals the exciton lifetime.

### $\mathcal{N}$ independent single photon emitters

Finally, the photon statistics of  $\mathcal{N}$  identical, statistically independent single photon emitters is evaluated. Their mean intensity is just the sum of all single emitter

## 5. Photon emission statistics

intensities

$$\langle I_{\mathcal{N}}(t) \rangle = \mathcal{N} \langle I(t) \rangle \quad (5.16)$$

whereas the correlation intensity is given by pairwise combination of two photons that could originate from any emitter

$$\langle I_{\mathcal{N}}(t) I_{\mathcal{N}}(t + \tau) \rangle = \sum_{i=1}^{\mathcal{N}} p_{|e\rangle_i} \sum_{j=1}^{\mathcal{N}} p_{|e\rangle_j | g \rangle_i} . \quad (5.17)$$

If we assume that the emitters are statistically independent, the sum over  $j$  facilitates since we can distinguish two cases (of correlating photons from different or from the same emitter):

$$\begin{aligned} p_{|e\rangle_j | g \rangle_i} &= p_{|e\rangle} & \text{for } i \neq j \\ p_{|e\rangle_j | g \rangle_i} &= p_{|e\rangle_j | g \rangle_j} = p_{|e\rangle | g \rangle} & \text{for } i = j \end{aligned} \quad (5.18)$$

Writing the sums in Eq. (5.17) explicitly gives

$$\begin{aligned} \sum_{i=1}^{\mathcal{N}} p_{|e\rangle_i} \sum_{j=1}^{\mathcal{N}} p_{|e\rangle_j | g \rangle_i} &= \sum_{i=1}^{\mathcal{N}} p_{|e\rangle_i} ((\mathcal{N} - 1) p_{|e\rangle_i} + p_{|e\rangle_i | g \rangle_i}) \\ &= \mathcal{N}(\mathcal{N} - 1) p_{|e\rangle} p_{|e\rangle} + \mathcal{N} p_{|e\rangle} p_{|e\rangle | g \rangle} . \end{aligned} \quad (5.19)$$

Comparing this with Eq. (5.13) and (5.14), we obtain

$$\langle I_{\mathcal{N}}(t) I_{\mathcal{N}}(t + \tau) \rangle = \mathcal{N}(\mathcal{N} - 1) \langle I(t) \rangle^2 + \mathcal{N} \langle I(t) I(t + \tau) \rangle . \quad (5.20)$$

Thus, the second-order correlation function for  $\mathcal{N}$  identical but statistically independent emitters is given by

$$\begin{aligned} g_{\mathcal{N}}^{(2)}(\tau) &= \frac{\langle I_{\mathcal{N}}(t) I_{\mathcal{N}}(t + \tau) \rangle}{\langle I_{\mathcal{N}}(t) \rangle \langle I_{\mathcal{N}}(t + \tau) \rangle} = \frac{\mathcal{N}(\mathcal{N} - 1) \langle I(t) \rangle^2 + \mathcal{N} \langle I(t) I(t + \tau) \rangle}{\mathcal{N}^2 \langle I(t) \rangle \langle I(t + \tau) \rangle} \\ &= \frac{\mathcal{N} - 1}{\mathcal{N}} + \frac{1}{\mathcal{N}} (1 - e^{-\frac{|\tau|}{\tau_0}}) . \end{aligned} \quad (5.21)$$

### 5.1.4. Photon emission statistics of blinking carbon nanotubes

At low temperature CNTs exhibit non-classical photon statistics, i.e. the antibunching of photons [76, 77, 127]. Additionally they are affected by charge fluctua-

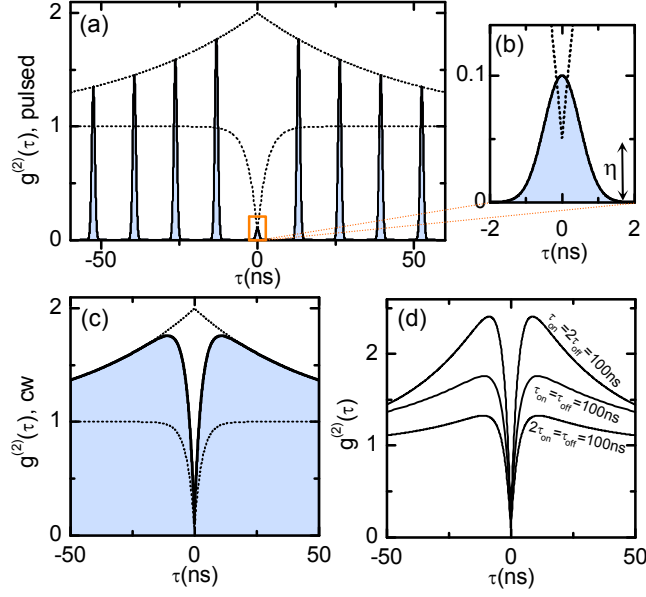


Figure 5.2.: **Expected photon statistics:** (a) Simulated photon statistics of a blinking single photon emitter under pulsed excitation ( $f^{-1} = \frac{1}{76 \text{ MHz}} \approx 13 \text{ ns}$ ) showing photon anti-bunching (lower dashed line) superimposed with photon bunching (upper dashed line). The spontaneous emission lifetime was  $\tau_{\text{sp}} = 3 \text{ ns}$ , the blinking times to  $\tau_{\text{on/off}} = 100 \text{ ns}$  and anti-bunching contrast to  $1 - \eta = 0.95$ . (b) Zoom in to  $\tau = 0$  shows the discrepancy between  $\eta = 0.05$  and  $g^{(2)}(0) = 0.1$ . (c) Photon statistics using the same parameters but a continuous excitation scheme. (d)  $g^{(2)}(\tau)$  for continuous excitation or envelope for pulsed excitation with different characteristic blinking times. Compared to a non-blinking emitter,  $g^{(2)}(\tau)$  is exaggerated up to 2.5 for  $\tau_{\text{on}} = 2\tau_{\text{off}} = 100 \text{ ns}$ .

tions in their environment leading to long term intensity fluctuations varying from a few 100 ns up to hours. Since the typical time scale of blinking  $\tau_{\text{on/off}}$  is far beyond the exciton lifetime  $\tau_0$  - even in the cleanest CNTs - we can keep both processes decoupled. Taking the product of Eqs. (5.12) and (5.15),  $g^{(2)}(\tau)$  of an individual CNT is given by

$$g^{(2)}(\tau) = \left( 1 + \frac{\tau_{\text{off}}}{\tau_{\text{on}}} e^{-\left(\frac{1}{\tau_{\text{on}}} + \frac{1}{\tau_{\text{off}}}\right)|\tau|} \right) \left( 1 - e^{-\frac{|\tau|}{\tau_0}} \right) . \quad (5.22)$$

In order to proof that a non-blinking emitter is a single-photon emitter, it is sufficient to consider  $g^{(2)}(\tau = 0)$ . The threshold for a single photon emitter is  $g^{(2)}(\tau) < 0.5$ . Due to the superimposed signature of photon-bunching especially for  $\tau = 0$  this does not hold for blinking photon emitters. Rather the influence due to the blinking condition has to be separated from the single emission process. Accounting for this,

## 5. Photon emission statistics

we introduce a contrast factor  $\eta$  that is defined as

$$\eta := \frac{g^{(2)}(\tau)}{1 + \frac{\tau_{\text{off}}}{\tau_{\text{on}}} e^{-\left(\frac{1}{\tau_{\text{on}}} + \frac{1}{\tau_{\text{off}}}\right)|\tau|}} = \frac{g^{(2)}(\tau = 0)}{1 + \frac{\tau_{\text{off}}}{\tau_{\text{on}}}} . \quad (5.23)$$

For a non-blinking emitter ( $\tau_{\text{off}} = 0$ ) this just equals  $g^{(2)}(0)$ . Therefore the threshold for single photon emission is again  $\eta < 0.5$ . The discrepancy between  $g^{(2)}(0)$  and  $\eta$  is illustrated in Fig. 5.2, which shows the simulated photon statistics expected from a blinking single photon emitter.

## 5.2. Hanbury-Brown and Twiss interferometer

### 5.2.1. Basic considerations

Proposed by Hanbury-Brown and Twiss [191] for astronomical application, their intensity correlating interferometer (HBT) has become an important tool for quantum optics since the first experimental proof of photon anti-bunching from single atoms by H.J. Kimble et al. [192]. The principle of an HBT interferometer is as follows. An incoming light beam is split into two paths (of same intensity in an ideal case). The intensity of each path is detected separately and then correlated. Hanbury-Brown and Twiss demonstrated that this correlation can be a linear multiplication of the intensity fluctuation or a coincidental measurement that counts the simultaneous arrival of photons on each detector.

For quantum optical application single photon counters (SPC) are widely used because they feature a high temporal resolution ( $\sim 350$  ps) and are sensitive to single photons. Thus, they are highly suitable for measuring the Fock state of a light beam [187]. An SPC generates a digital electric pulse whenever at least one photon is detected. After detection, it exhibits a dead-time  $\tau_{\text{dead}}$ , during which it cannot detect another photon. In order to correlate the two paths, a detection event on the SPC in path 1 triggers the "start" of an electronic time clock. A subsequent detection event on the SPC in path 2 triggers "stop". This scheme allows for determination of the time difference  $\tau$  between two consecutively incident photons and is particularly capable to resolve  $\tau < \tau_{\text{dead}}$ , which is impossible for a setup using a single detector only.

The statistical distribution of  $\tau$  is revealed in histograms that cumulate the time differences from many repeated measurements. Under certain conditions the second-

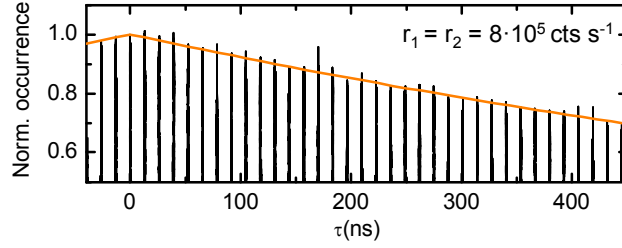


Figure 5.3.: **Normalized correlation histogram of an intense pulse light source** illustrates a weak saturation effect. The orange solid line displays the theoretically expected probability distribution  $\frac{r}{f_{\text{laser}}}$ . However, the respective count rates  $r_{1/2}$  exceeded typical count rates gained from an individual CNT by far. Thus, this saturation effect becomes negligible for the here presented experiments.

order correlation function  $g^{(2)}(\tau)$  (see Chap. 5.1) can be simply determined by normalization of these histograms. This requires [193]:

- The average time between two photons must be larger than the dead time of the SPC detectors.
- The investigated light source must not emit too many photons at once.
- The count rate must be adapted to the period of interest.

The following considers all these conditions. First of all we define the average count rate  $r_i$ , which is the temporal mean of photons detected by detector  $i$  per time unit. Typically SPCs feature dead-times  $\tau_{\text{dead}}$  below 70 ns. Hence, the first condition is fulfilled as long as  $r < 14 \cdot 10^6 \text{ cts s}^{-1}$ . This was the case in our experiments as count rates never exceeded  $2 \cdot 10^3 \text{ cts s}^{-1}$ .

Also the second condition was trivially fulfilled. As we will show below, the PL of individual CNTs at cryogenic temperatures featured characteristic photon anti-bunching, so that a CNTs emits typically photons one by one [76,77]. Of course, only a smaller fraction of these photons were detected. From such a source we expect all correlation events at  $|\tau| > 0$  and especially no saturation effects, which would occur for a very intense pulsed light beam. Additionally, placing the setup in a light-tight box and spectral filtering the PL light reduced background counts well below the intrinsic dark count rate of the used SPCs.

Only the third condition deserves a closer inspection, especially since the range of interest is much higher for investigation of a blinking emitter (typically 500-1000 ns) than for the proof of photon anti-bunching where a range of  $\pm 30 \text{ ns}$  is sufficient [76]. First, we will illustrate matters in a probabilistic approach. In order to create a

## 5. Photon emission statistics

correlation event at  $\tau$  in an HBT interferometer, it is not sufficient that two photons are incident on each SPC within the time interval  $\tau$ . Rather after the first photon triggers "start", no other (third) photon is allowed to trigger "stop" before the second photon does. Therefore the probability to detect correlation with a big time delay is lower than the probability for the detection of a small time delay. In practice no correlation event with  $\tau > 1$  h will be detected, although  $g^{(2)}(\tau = 1 \text{ h}) = 1$  in all known cases.

We examine a pulsed light source (repetition frequency  $f_{\text{laser}}$ ) that creates an identical average count rate on each detector ( $r = r_1 = r_2$ ). The probability to detect a correlation for the  $k^{\text{th}}$  pulse is then given by

$$P(k) = \frac{r}{f_{\text{laser}}} \left( 1 - \frac{r}{f_{\text{laser}}} \right)^{|k|} . \quad (5.24)$$

To illustrate this saturation we measured the correlation of an intense pulsed laser beam with a count rate of  $8 \cdot 10^5$  cts  $\text{s}^{-1}$  and a repetition frequency of 76.0 MHz. The count rates (normalized to  $\tau = 0$ ) are depicted in Fig. 5.3. The solid line displays the theoretical probability normalized to  $r/f_{\text{laser}}$ . In our experiments typical count rates did not exceed 2000 cts  $\text{s}^{-1}$ . For such low count rates the detection probability is only negligibly varied for  $\tau < 1000$  ns (or using pulsed excitation for the first 76 fringes of the histogram). In detail, the probability for correlating two photons from the same pulse  $P(k = 0)$  is only two tenth percent higher than the probability for correlating two photons separated by 1000 ns<sup>4</sup>:

$$P(k = 75) = 0.9980 \cdot P(k = 0) . \quad (5.25)$$

In summary, we fulfill all conditions to evaluate  $g^{(2)}(\tau)$  from normalization of the measured histograms correlating only two consecutive photons.

For faint PL signals we further used pulsed excitation to increase the signal-to-noise ratio. In consequence, this concentrates detection events to  $\tau = 0$  and multiples of the excitation pulse frequency instead of accumulating correlations for all possible values of  $\tau$ . Compared to continuous excitation, it allows for faster determination of the characteristic blinking times  $\tau_{\text{on/off}}$  and of the anti-bunching contrast  $1 - \eta$ .

---

<sup>4</sup> $P(75) = \left( 1 - \frac{2000 \text{ cts s}^{-1}}{76 \text{ MHz}} \right)^{75} \approx 0.9980$

### 5.2.2. Hanbury-Brown and Twiss interferometer setup

#### Single photon detectors

Silicon avalanche photodiodes (APD) are sensitive to single photons in a broad spectral range from the visible to the near infrared region [194]. Used in the Geiger mode - when the diode is highly reverse biased - a photon excites a single electron, which is accelerated to the diode's n-layer. During acceleration this electron excites secondary electrons from the intrinsic layer, which starts an avalanche process and results in a measurable current. This sudden gain of an avalanche current after incidence of a single photon allows the detection of single photons with an accuracy below 400 ps. Continuing the avalanche process would lead to gigantic current, which could harm the diode. Hence, shortly after occurrence of a detection event a control electronic reduces the bias voltage and stops the avalanche process. The time for stopping the avalanche process and re-biasing the diode adds up to a dead time of typical 70 ns after every detection event.

We employed two different APD models that will be compared in the context of APD cross talk later in this chapter. The first type was manufactured by PicoQuant<sup>5</sup> (PQ) and will be termed as PQ APD in the following. The second type was by Perkin Elmer<sup>6</sup> (PE) in the following PE APD. One of the PE APDs featured an FC fiber coupler placed before the optically active area. However, it could be also used in a free space setup provided that the beam was focussed appropriately.

#### Optical layout

Fig. 5.4 schematically depicts the setup of the used HBT interferometer, which was placed in a light-tight box. The optical signal was sent in via a single-mode fiber (SM<sup>7</sup>) and coupled to free space with a fiber coupler FC1<sup>8</sup>. The collimated beam was split at a 50:50 beam splitter (BS)<sup>9</sup> and each half was imaged on the optically active area of one APD by the lenses L<sub>1</sub> and L<sub>2</sub><sup>10</sup>, respectively. In order to reduce cross talk between both APDs, the collimated beams were not focused on the optically active areas but illuminated them as much as possible. In detail, this is discussed later

<sup>5</sup> $\tau$ -SPAD-20 by PicoQuant GmbH, Berlin, Germany

<sup>6</sup>SPCM-AQHR-15 by Perkin Elmer Optoelectronics, Vaudreuil, Canada

<sup>7</sup>single-mode fiber SM800 specified for 830 nm: SM800 5.6/125/245 by Diamond GmbH, Echterdingen, Germany

<sup>8</sup>Coupling lens: focal length  $f = 11$  mm; C220TME-B by Thorlabs

<sup>9</sup>BS010 by Thorlabs. The beam splitter is mounted on a flip mount. This allows to swing it out of the beam so all light is focussed on APD 1 only. This makes the setup versatile for other applications.

<sup>10</sup>focal length  $f = 18.4$  mm; C280TME-B by Thorlabs



### 5.2.3. Reducing the cross talk

During the avalanche effect an APD itself emits photons in a breakdown flash due to electroluminescence [195]. This flash is insignificant if the APDs are sufficiently distant from each other (space-like separated) or when only a single APD is used (like in measurements on the exciton lifetime discussed in Chap. 5.3.4). However, the APDs in the described setup were not space-like separated. Rather the breakdown flash of one APD reached the other within the range of interest and triggered falsified correlation events. This crosstalk can not be regarded as a minor artefact. First, it reduces the rate of significant correlation events. Further, it could become a limiting factor in the detection of possible fast intensity fluctuation (see Chap. 5.1.2).

Fig. 5.5(a) depicts the integrated cross talk events between two APDs in our HBT setup that were operated for 10 hours in complete darkness. We found two accumulation points for correlation events for  $\tau \approx \pm 5$  ns. This corresponded to  $c \cdot 5$  ns  $\approx 1.5$  m, which equals the optical path length from one APD to the fiber coupler and back to the second APD. By covering the fiber coupler FC1 with a nonreflective opaque beam block, we completely suppressed the cross talk between both APDs as illustrated by only five correlation events in 10 hours (orange bars in Fig. 5.5(a)).

We measured the spectrum of the breakdown flash by using a 50:50 fiber beam splitter connected to the fiber input of the HBT box as depicted in the inset of Fig. 5.5(b). We inserted a faint laser beam with a wavelength of  $\lambda_{\text{exc}} = 850$  nm through the beam splitter into the HBT input. This increased the rate of detection events and thereby the overall intensity of the breakdown flash. The exit of the beam splitter was connected to a spectrometer (see Chap. 3.1.2). We used a 900 nm long pass filter (blocking region marked as grey area) in front of the spectrometer to filter out any laser light. In accord with previous reports [195,196] we find the wavelength of the flash broadly distributed in the detection range with a small local maximum around 980 nm. Surprisingly, the intensity of the breakdown flash was five times higher for the PQ APDs compared to the PE APDs as illustrated in Fig. 5.5(b).

Knowing its origin, we now took several measures against APD cross talk. As a measure of cross talk, we quantified the share of falsified correlation events in all correlation events. In a photon correlation measurement of a pulsed laser beam we compared the rate of falsified correlation events  $n_{\text{false}}$  (blue area in Fig. 5.5(c)) with the rate of correct correlation events at  $\tau = 0$  termed as  $n_{\text{correct}}$  (orange area). We did this for various laser intensities. As a measure for the laser intensity we took the count rate  $r_{\text{laser}}$  of APD 1 (not the correlation rate between both) and kept this

## 5. Photon emission statistics

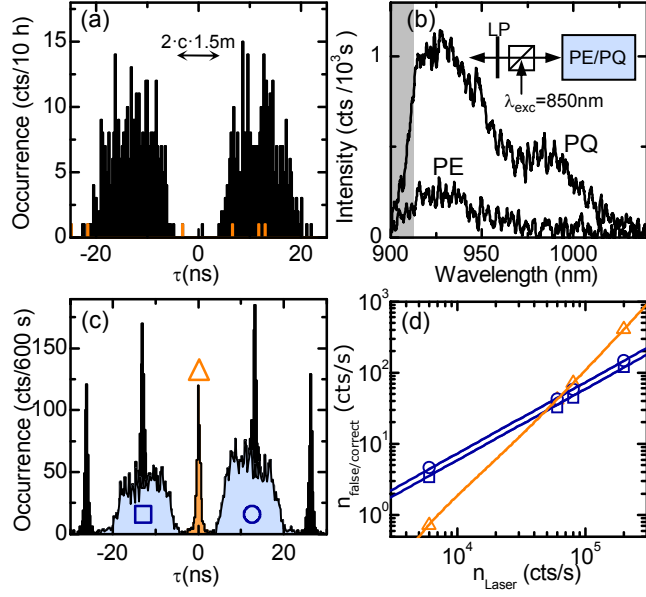


Figure 5.5.: **Cross talk between avalanche photo-detectors** (a) recorded in a correlation measurement in complete darkness (black histogram). The correlation events are triggered by photon or thermal noise and vanish when the fiber coupler FC1 was covered (orange histogram). (b) Spectrum of the breakdown flash from Perkin Elmer (PE) and PicoQuant (PQ) APDs recorded by a setup shown in the inset. A faint laser beam triggered more counting events and thus increased the flash intensity. (c) Photon correlation measurement of a laser beam with  $n_{\text{laser}} = 6,000 \text{ cts s}^{-1}$ . The number of correct (falsified) correlation events is shaded orange (blue). (d) Rates for falsified and correct correlation events as a function of the laser intensity showing linear and quadratic dependence, respectively.

rate small enough that saturation effects due to the APD dead time were negligible. A correlation event is a two-photon process because each APD is triggered by one photon. As expected for such a process we found a quadratic dependence of  $n_{\text{correct}}$  on  $r_{\text{laser}}$  (Fig. 5.5(d)). The detection efficiency given by  $n_{\text{correct}}/r_{\text{laser}}^2$ . In contrast, a single photon is sufficient to trigger a falsified correlation event so we find  $n_{\text{correct}}$  as a linear function of  $r_{\text{laser}}$ . The cross talk rate is then  $n_{\text{correct}}/r_{\text{laser}}$ .

All taken measures are a trade-off between cross talk rate and detection efficiency. Tab. 5.1 summarizes our progress. For a HBT setup using two PQ APDs we reduced the cross talk rate  $h$  by a factor of two. Here, the laser spot illuminated the entire optically active area instead of being focussed on it. As the entire laser spot still fitten onto the active area, the detection efficiency was unaffected.

If we further used the PE APDs instead of the PQ APDs, we found again a

### 5.3. Freely suspended carbon nanotubes

APD type	layout	detection efficiency	cross talk
		$n_{\text{correct}}/n_{\text{laser}}^2$ (in $10^{-8}$ s/cts)	$n_{\text{false}}/n_{\text{laser}}$ (in $10^{-4}$ )
PicoQuant (PQ)	spot focused	1.026	10.4
	spot maximized	1.024	6.6
Perkin Elmer (PE)	spot maximized	1.14	2.8
	multi-mode fiber	0.57	0.01

Table 5.1.: **Detection efficiency and cross talk** for different layouts of the HBT box. For the free space setup configuration the detection efficiency is constant regardless of the APD type. Expanding the spot size and using a multi-mode fiber for spatial filtering reduces the cross talk by a factor of 1000. In return, attenuated transmission through the fiber reduces the detection efficiency by 0.5.

considerably reduced cross talk. This confirms our findings from the breakdown flash spectra of each APD model (Fig 5.5(b)). PQ APDs exhibit generally an increased breakdown flash intensity. In both measurements we consistently identified that the breakdown flash intensity of PQ APDs exceeded those of the PE APDs by a factor of five.

One of the PE APDs featured already a fiber connector that could be only used with an additional focussing lens in a free space setup. In a more elegant layout we coupled one arm of the HBT setup in a multi-mode fiber (core diameter 62.5  $\mu\text{m}$ ), which provided for ideal imaging on the active area. In addition, the fiber acts as a spatial filter and suppressed overwhelmingly the cross talk rate by a factor of 280. In return, the transmission loss due to coupling in a fiber was almost 30 percent, which reduced the detection efficiency by roughly 50 percent. For all correlation measurements presented in this thesis, we employed this layout with a multi-mode fiber.

### 5.3. Freely suspended carbon nanotubes

The previous chapters presented indication that many detrimental spectroscopic features of CNTs arise from the interaction with the environment. Spectral wandering was assigned to interaction with close charge fluctuators (see Chap. 4.3) and also localization potentials and excitation spectra were identified as presumably sensitive to close charge impurities (see Chap. 4.7). In a second approach for studying the localization of excitons we focus on the isolation of individual CNTs from their environment. With except of their suspension points, freely suspended CNTs are not in contact with any dielectric material as illustrated in Fig. 5.6(c). Such samples

## 5. Photon emission statistics

could not be manufactured from spin-coating of a commercial CoMoCat solution. Rather, we grew CNTs directly over the trenches of a perforated substrate using a chemical-vapor-deposition (CVD) process. A detailed study considering growth of CVD CNTs was presented in the diploma thesis of M. Hofmann [91].

In the following, we discuss the optical properties of individual as-grown suspended CVD CNTs at cryogenic temperature ( $T = 4.2$  K). These results were also published in Ref. [127]. We give a brief overview on the preparation of as-grown suspended CVD CNTs. Then, their optical properties are compared to sc encapsulated CoMoCat CNT dispersed on a Si-SiO<sub>2</sub> substrate. In particular, we discuss experiments that consider exciton lifetime, photon anti-bunching and fast intermittency processes. The two sample layout are illustrated in Fig. 5.7, which also presents complementary images from both layouts. We identified locally confined PL emission from sc encapsulated CoMoCat CNT dispersed on a Si-SiO<sub>2</sub> substrate (left panels) and from as-grown suspended CVD CNTs (right panels). In addition, we will discuss a third layout that features CVD CNTs grown on a SiO<sub>2</sub> substrate that is not depicted here.

### 5.3.1. As-grown suspended CNTs

CNT material, which will be termed as CVD CNTs in the following, was synthesized by chemical-vapor-deposition (CVD) in a standard CVD furnace. The growth was assisted by a bimetallic iron-ruthenium (FeRu) catalyst. The catalyst particles were deposited on carrier substrates from a FeRu suspension either by spin or by drop coating. For synthesis of CNTs the samples were heated to 850°C in an Ar/H<sub>2</sub> (95%-5%) gas mixture and then kept in a constant flow of 1 slm methane and 0.75 slm hydrogen for 10 minutes before allowing to cool down in a hydrogen and Ar/H<sub>2</sub> gas flow. The growth procedure was optimized to yield a CNT density below 1 μm<sup>2</sup> and narrow-diameter nanotubes with a mean diameter below 1 nm. Diameter distribu-

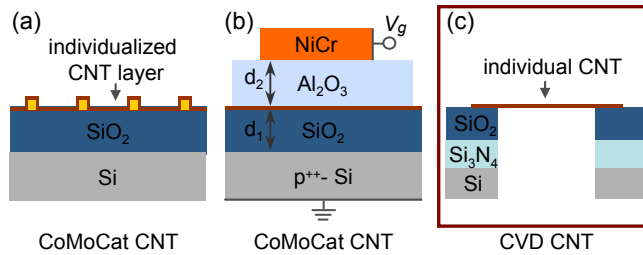


Figure 5.6.: **Sample layouts III:** CoMoCat CNTs on a silicon oxide surface, which features a metallic grid (a). CoMoCat CNTs embedded in an electric gate device (b). CVD CNT freely suspended over a crater (c).

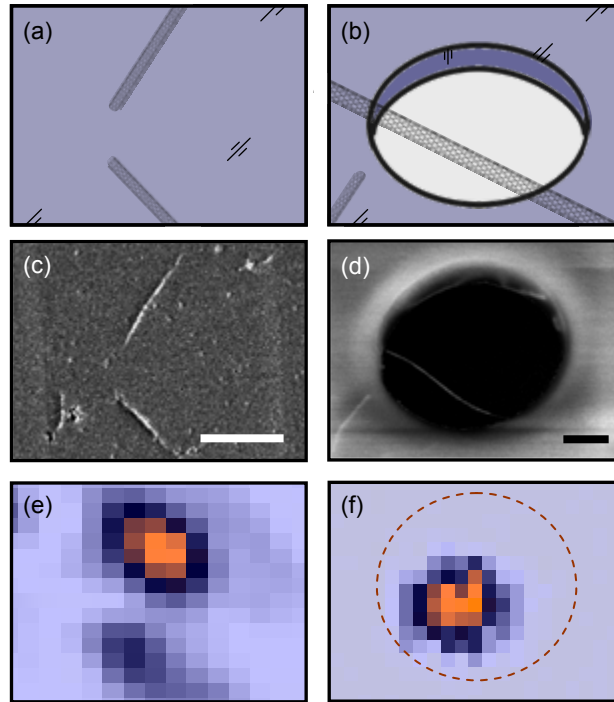


Figure 5.7.: **CoMoCat CNTs on substrate (left panels) and as-grown suspended CVD CNTs (right panels):** (a-b) Schematic illustration. (c-d) SEM image of a sample section. The scale bar measures 1  $\mu\text{m}$ . (e-f) Complementary micro PL maps of the same sections revealed spatially confined PL emission.

tions were obtained by tapping-mode atomic force microscopy on samples with CVD CNTs fully supported by a Si-SiO<sub>2</sub> substrate. Such samples with as-grown CVD CNTs in contact with SiO<sub>2</sub> were used as reference material for density and diameter distributions as well as in cryogenic spectroscopy. Suspended CNTs were synthesized on commercial grids typically used in transmission electron microscopy (TEM). The specific grid used in the experiments was perforated with holes of 2  $\mu\text{m}$  diameter and a pitch of 4  $\mu\text{m}$  and coated with  $\sim 100$  nm of SiO<sub>2</sub> by plasma enhanced CVD. The grids provided for suspension of nanotubes in the region where the hole-perforated Si<sub>3</sub>N<sub>4</sub> membrane was not supported by the underlying Si frame; this region was located in the center of the TEM grid. However, the Si carrier frame supported the SiO<sub>2</sub>-Si<sub>3</sub>N<sub>4</sub> membrane at its edges. With scanning electron microscopy (SEM) we identified CNTs suspended over the full diameter of the crater as well as CNTs that were suspended only near the walls of the crater. Also the latter exhibited partly suspended segments at the perimeter of the crater.

### 5.3.2. Methods

PL spectra of individual CNTs were already discussed in the previous chapters. For recording of photon emission statistics we used the HBT interferometer without any spectral filtering. The correlation box allowed to correlate two detection events separated within 65536 time bins. Due to this fixed number of bins the resolution  $\delta\tau_{\text{res}}$ , which equals the width of each bin, determined the total range of interest  $\tau_{\text{max}}$ . Therefore, we used a low resolution  $\delta\tau_{\text{res}} = 256 - 512$  ps in order to extend the range of interest to longer timescales. In fs-pulsed mode the excitation laser was operated with a repetition rate of  $f_{\text{laser}} = 76.0$  MHz. We controlled the time-averaged laser power via the power stabilization (bandwidth  $<10$  kHz) presented in Chap. 3.1.2. However, the maximum power deposited within one fs-laser pulse exceeded the time-averaged intensity by at least one order of magnitude. In order to prevent CNTs from bleaching, we reduced the time-averaged intensity by at least a factor of 3 before switching the laser from cw to fs-pulsed mode. For a significant determination of photon emission statistics we integrated between 2 to 10 h. As discussed in Chap. 5.2.3 signatures of cross-talk were highly suppressed in all correlation histograms.

Stable PL emission from CVD CNTs routinely allowed for recording of two-photon-correlations in pulsed *and* continuous excitation. In contrast, CoMoCat CNTs showed blinking on all time scales and often inhibited long-lasting recording as required for significant statistics of two-photon-correlations. Because of the increased signal-to-noise ratio, we employed only pulsed excitation to obtain photon emission statistics of CoMoCat CNTs.

With minor modifications on the HBT setup, we determined the photoluminescence lifetime of individual CNTs by correlating the signal of a single APD with the trigger output of the TiSa laser. However, the short lifetime of CoMoCat CNTs hindered the use of APD photon counters because their time resolution was beyond typical PL lifetimes of 20-80 ps. To estimate the lifetime of the CoMoCat reference material we used a streak camera<sup>14</sup>, which featured a resolution below 5 ps.

### 5.3.3. Spectral properties

Compared to the PL spectra of CoMoCat CNTs, the narrow line width is the first striking difference in the PL of individual CVD CNTs as illustrated in Fig. 5.8. Such narrow optical line widths are unusual for CNTs, even at cryogenic temperatures

---

<sup>14</sup>C5680 by Hamamatsu

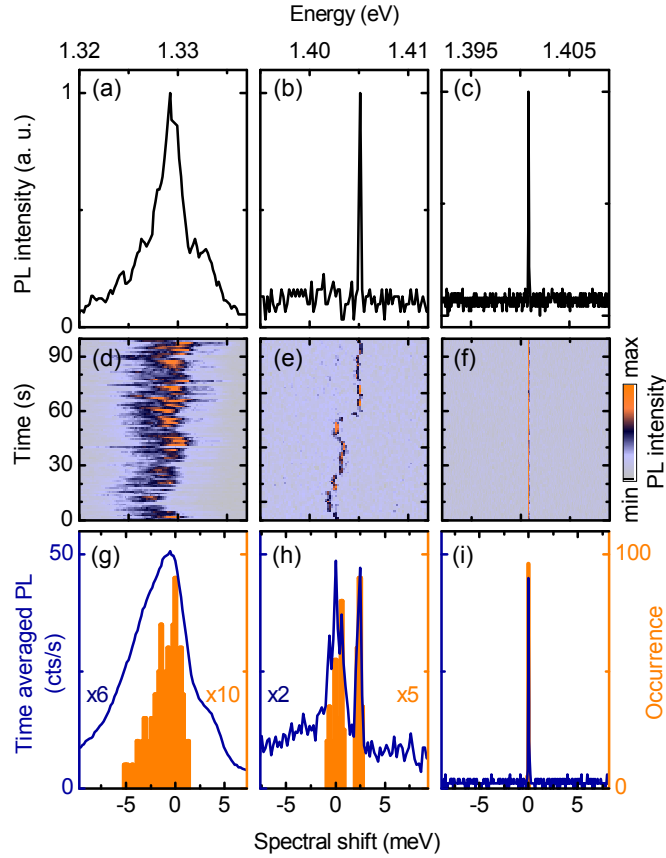


Figure 5.8.: **Spectral properties of suspended CVD CNTs** (right column) in comparison with CVD CNTs on a  $\text{SiO}_2$  substrate (middle column) and CoMoCat CNTs on a  $\text{SiO}_2$  substrate (left column): (a-c) Spectra recorded with an integration time of 1 s. (d-f) PL traces featuring spectral jumps and wandering. (g-i) PL energy histograms (in orange) and spectra recorded with 100 s integration (blue traces). (Adapted from Ref. [127])

[60, 76, 197]. For reference we studied as-grown CVD CNTs in contact with  $\text{SiO}_2$  as well as commercial CoMoCat CNTs dispersed on  $\text{SiO}_2$  (discussed in Chap. 3). Under similar experimental conditions, CoMoCat CNTs typically exhibited asymmetric PL profiles [59, 76, 197] with line widths of a few meV, one order of magnitude broader than our CVD-grown nanotubes in 1 s integration time.

On longer experimental timescales, the line width of the time-averaged PL broadened even further for suspended CNTs as illustrated the spectra of Fig. 5.8(g,h). However, suspended CVD CNTs showed no change in the emission profile, irrespective of the integration time. The effective integration time of Fig. 5.8(i) was 100 s, but same hold true for up to several days of observation. The PL time traces in Fig. 5.8(d-

## 5. Photon emission statistics

f) reveal that spectral wandering was responsible for the broadening of the optical line width on a meV energy scale, in accord with previous reports [76, 134, 197]. At the same time, it also accounted for the apparent fine structure [60, 134] and, to some extent, for the asymmetry in the spectral profile as illustrated in the histograms of Fig. 5.8(g-i). For small integration times CVD CNTs fully supported by a Si-SiO<sub>2</sub> substrate featured narrow emission line as exemplified in Fig. 5.8(b). However, in the course of integration these CNTs developed an asymmetric peak accompanied by a satellite as shown in Fig. 5.8(h), which corresponds to time-averaging of the PL trace depicted in Fig. 5.8(e). For suspended CNTs, such detrimental features as spectral wandering were not observed.

### 5.3.4. Photoluminescence lifetime

In contrast to previous reports we found decay times on the scale of nanoseconds for all suspended CNTs. This is one order of magnitude longer than for the CoMoCat reference material as illustrated by red versus black circles in Fig. 5.9(b). A PL decay trace for a single suspended CVD CNT with a monoexponential decay time of 3.35 ns is shown in Fig. 5.9(a). Previous room-temperature experiments determined both monoexponential and biexponential decays depending on material quality, with photoluminescence decay times of the order of tens of picoseconds [198]. Similar results were obtained at low temperatures [122]. The discrepancy between the 10-100 ps PL lifetimes observed experimentally and the radiative exciton lifetimes of 1-10 ns predicted by theory [33, 64, 65] is attributed to rapid non-radiative decay of mobile excitons encountering quenching sites (Auger processes) [61].

The long PL lifetimes in our suspended CVD CNTs indicate that excitons were protected by localization from exploring quenching sites. PL lifetimes on the scale of nanoseconds are in agreement with the radiative lifetimes estimated for excitons with coherence lengths in the range between the exciton Bohr radius of 1.2 nm in narrow-diameter CNTs [34] and the optical wavelength, as depicted by solid lines in Fig. 5.9(b). We estimate the intrinsic radiative lifetime  $\tau$  of CNT excitons as [33, 65]

$$\frac{1}{\tau} = \frac{\sqrt{\epsilon} e^2 E_{11}^2 f}{2\pi\epsilon_0 m_0 \hbar^2 c^3}, \quad (5.26)$$

using the free electron mass  $m_0$  and  $\epsilon = 1.846$  for the surrounding vacuum.  $f$  denotes the oscillator strength per carbon atom and is given by  $0.014 \text{ eV}^{-1} E_{11} d_t \sigma_c / A$  where  $A$  is the area per carbon atom  $A = \frac{3\sqrt{3}}{4} a_{cc}^2$  and  $\sigma_c$  the confinement length in units of the exciton Bohr radius  $\alpha_B$  [34].

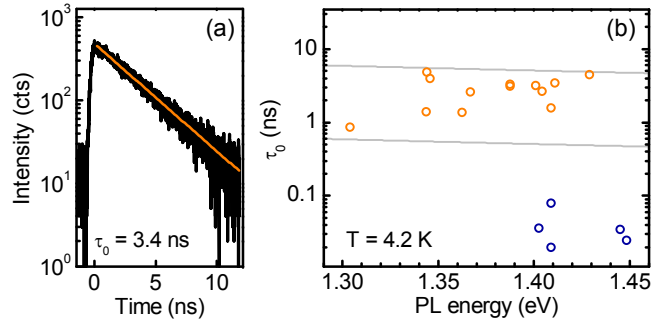


Figure 5.9.: **Exciton lifetime in suspended CVD CNTs:** (a) The PL intensity of suspended CVD CNTs as a function of time (black solid line) showed an mono-exponential decay (here exciton lifetime  $\tau_0 = 3.4$  ns, fit illustrated as orange solid line). (b) These exciton lifetimes (orange circles) exceed those typically observed in CoMoCat CNTs (blue circles) by at least one order of magnitude and agree with the estimation of the intrinsic exciton lifetime, which is illustrated by the grey solid lines. (Adapted from Ref. [127])

Moreover, localization is also responsible for narrow emission profiles by inhibiting diffusive exploration of inhomogeneities along the tube axis that would give rise to line broadening via dephasing. Taking the resolution limit of our spectrometer as a conservative value for the total line width, we arrive at 15 ps for the lower bound to the exciton coherence time in CNTs at 4.2 K. Further support for exciton localization is given by the now following discussion of the photon emission statistics. Like reported on CNTs at low temperatures [76,77], also the PL from freely suspended CVD CNTs featured non-classical photon emission.

### 5.3.5. Photon emission statistics

Fig. 5.10 depicts spectra and photon emission statistics of both a CoMoCat CNT on substrate (upper panels) and a suspended CVD CNT (lower panels). It exemplifies broad and asymmetric PL emission profiles of CoMoCat CNTs contrasting the narrow emission lines of freely suspended CVD CNTs. The photon emission statistics of both CNTs featured non-classical light emission, i.e. photon anti-bunching as proven by the missing central peak at  $\tau = 0$ . In addition, the CoMoCat CNTs showed significant signatures of photon bunching due to fast intermittency.

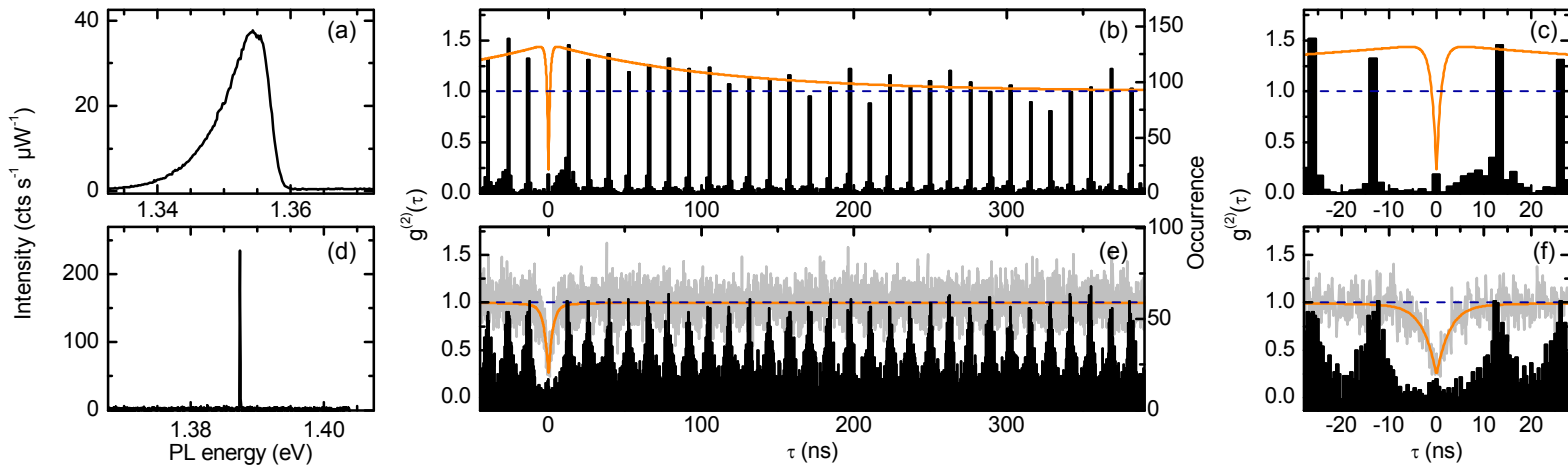


Figure 5.10.: **Spectra and photon emission statistics of CoMoCat CNTs (upper panels) and as-grown suspended CVD CNTs (lower panels):** (a) Spectrum of a CoMoCat CNT recorded with continuous excitation featuring a single asymmetric emission line with a line width of 5.1 meV. (b) Photon statistics of the same tube recorded in 10 hours with pulsed excitation (black solid line) that reveals signatures of photon anti-bunching (missing peak at  $\tau = 0$ ) and photon bunching (exponential decay). The orange solid line displays a fit according to Eq. (5.22) with  $\eta = 0.87$ ,  $\tau_{\text{on}} = 343$  ns and  $\tau_{\text{off}} = 160$  ns. (c) Zoom in to  $\tau = 0$ . (d) Spectrum of a suspended CVD CNT featuring a single narrow emission line below the spectrometer resolution limit of 40  $\mu\text{eV}$ . (e) Photon statistics of the same CNT recorded in 10 hours with pulsed excitation (black solid line) and continuous excitation (grey solid line), respectively. Both histograms show photon anti-bunching without any signatures of photon-bunching for  $\tau > \tau_0$ . The orange solid line displays a fit according to Eq. (5.22) with  $\eta = 0.89$  and  $\tau_0 = 3.3$  ns but diverging values for  $\tau_{\text{on}} \rightarrow \infty$  and  $\tau_{\text{off}} \rightarrow 0$ . (f) Zoom in to  $\tau = 0$ .

We used a standard fitting routine to normalize the histograms (as discussed in Chap. 5.2.1) and to fit Eq. (5.22), which is depicted as orange solid lines in Figs. 5.10(b,d). This gave the characteristic blinking times  $\tau_{\text{on/off}}$ , the anti-bunching contrast  $\eta$  and in case of CVD CNTs the PL lifetime  $\tau_0$  (see Eq. 5.23). For the fitting of pulsed histograms from CoMoCat CNTs we set  $\tau_0 = 1$  ns. For the CVD grown suspended CNTs we were also able to record significant photon emission statistics in continuous excitation (grey solid line in Fig. 5.10). For the CNT depicted here we found  $\tau_0 \approx 3.3$  ns and confirmed directly the extremely long lifetime of excitons in this material.

### Intermittency

All CoMoCat CNTs featured photon-bunching superimposed on signatures for single photon emission. In the picture of a blinking single-photon emitter, which switches between a dark and an emitting state, we identified characteristic times  $\tau_{\text{on}}(\tau_{\text{off}})$  in a range of 70-310 ns (50-680 ns). Similar results were previously reported for CNTs embedded in PMMA<sup>15</sup> [77]. Fig. 5.11(b) depicts the characteristic time in the "on"-state  $\tau_{\text{on}}$  as a function of the characteristic time in the "off"-state  $\tau_{\text{off}}$ . In agreement with reports on blinking CNTs [77] as well as for self-assembled quantum dots [89],  $\tau_{\text{on}}$  and  $\tau_{\text{off}}$  differed not more than by a factor of 2, which is indicated by the blue shaded area in Fig. 5.11(a).

Photon-bunching signatures on a time scale of a few 100 ns were interpreted as a new aspect to intermittency [77]. These occur in addition to the general charging induced power-law blinking, we discussed in Chap. 4.3, and to intermittency caused by the activation of recombination centers [199].

In contrast, the photon emission statistics of as-grown suspended CVD CNTs did not exhibit such signatures of bunched photons. We found best conformance with our theoretical model given in Eq. (5.22) for diverging values of  $\tau_{\text{on}} \rightarrow \infty$  and  $\tau_{\text{off}} \rightarrow 0$ . This supports our findings that suspended CVD CNT featured blinking-free PL emission signal even on the shortest timescales. Due to isolation from external fluctuations and to ineffective occupation of the lower energetic dark state, as-grown suspended CVD CNTs were intrinsically bright.

### Photon anti-bunching

For all investigated CNTs (regardless if CoMoCat or CVD) we identified evidence for photon anti-bunching. Fig. 5.11(b) summarizes for all CoMoCat CNTs inves-

---

<sup>15</sup>poly (methyl methacrylate)

## 5. Photon emission statistics

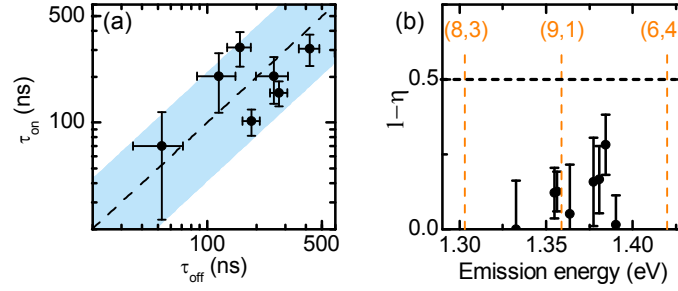


Figure 5.11.: **Time-resolved properties of CoMoCat CNTs:** (a) Without exception the photon emission statistics of CoMoCat CNTs featured photon bunching, which is associated to PL intermittency. Depicted are characteristic times "on" state  $\tau_{\text{on}}$  as a function of  $\tau_{\text{off}}$ , which indicate that both differ only by a factor of 2 (equivalent to the blue shaded area). (b) Anti-bunching contrast  $1-\eta$  for all recorded CoMoCat CNTs was below the threshold of 0.5 indicating single-photon emission.

tigated their anti-bunching contrast  $\eta$  as a function of the respective PL energy. All values were well below the threshold for unambiguous single-photon emission of  $\eta = 0.5$ . This non-classical photon emission of CNTs at cryogenic temperature has been reported previously [76, 77] and equals the photon emission statistics of quantum-dots. However, its physical origin is still arguable. Two possible mechanisms are discussed [76]:

First, exciton-exciton annihilation is highly efficient in CNTs [200]. Further, the diffusion length of CNT excitons has been reported with more than 610 nm [67] at room temperature and is prospected to increase considerably at cryogenic temperature [111]. After excitation of an exciton ensemble, highly mobile excitons would recombine non-radiatively, so that a CNT could end up at most with a single exciton only. Exciton-exciton annihilation is typically responsible for saturation effects in the emission of mobile CNT excitons [201]. However, also at high excitation intensities photon anti-bunching was observed in CoMoCat (see Ref. [76]) and CVD CNTs (see Fig. 5.12). As the rate of exciton-exciton annihilation is only reasonably higher than the PL rate, efficient exciton-exciton annihilation of delocalized CNTs cannot explain photon anti-bunching in even saturated PL signals.

A second possible mechanism is based on the formation of localization sites (CNT quantum dots). Although experimental indication for the existence of biexcitonic states in CNTs were reported [202], no direct PL emission from the biexciton could be observed [203]. This is furthermore surprising, since the biexciton recombination rate has been identified as efficient as the exciton-exciton annihilation rate. However, all experimental evidence indicate that the biexcitonic state in CNTs is

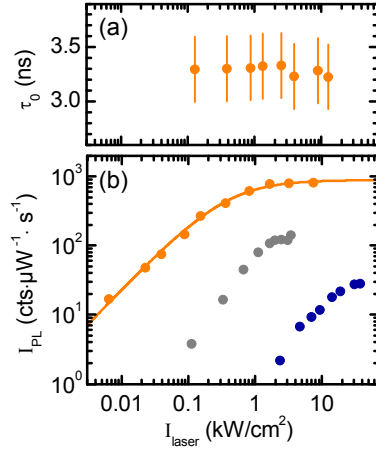


Figure 5.12.: **Photoluminescence saturation:** (a) Photoluminescence lifetime  $\tau_0$  of freely suspended CVD CNTs as a function of the laser intensity. As  $\tau_0$  is invariant we can rule out exciton-exciton annihilation. (b) Photoluminescence intensity as a function of the laser intensity for freely suspended CVD CNTs (orange), substrate supported CVD CNTs (grey) and substrate supported CoMoCat CNTs (blue). The orange solid line depicts the saturation response of a three-level system, which we discussed in [127].

intrinsically dark. If the PL emission from individual CNTs originates from single localized emission sites, like it has been extensively reported [58, 63, 125, 204], only the recombination of single excitons gives rise to PL emission. In consequence, an individual CNT quantum dot features non-classical light emission, i.e. the photon anti-bunching. Although the formation of several localization sites along short individual CNT has been imaged in near-field microscopy [58], we could not identify any signatures of two independent single-photon emitters, which would result in an decreased contrast of photon anti-bunching ( $0.5 < \eta < 1$ ).

In as-grown suspended CVD CNTs the PL intensity saturated for excitation intensities above  $5 \text{ kW cm}^{-2}$  as illustrated in Fig. 5.12. However, the mono-exponential PL lifetime remained constant without signatures of an emerging Auger-mediated rapid secondary decay, even for the highest laser powers. At the same time, we can rule out multi-exciton emission as the photon correlation shows pronounced anti-bunching both under continuous-wave and pulsed excitation. Instead, the saturation behavior is consistent with the response of a three-level system, which is discussed in Ref. [127] and indicated by the solid line in Fig. 5.12(b).

These findings imply the successful suppression of non-radiative photoluminescence quenching [61] and emission intermittence [77]. Further, they indicate ineffective shelving into lowest-lying long-lived dark states [64, 65], which renders localized

## 5. Photon emission statistics

excitons in suspended CNTs intrinsically bright. Compared in Fig. 5.12(b) to reference CoMoCat and CVD CNTs on substrate, the saturated PL intensities is orders of magnitude higher in case of the freely suspended material. In addition to the missing signatures of photon bunching associated with PL intermittence, this is strong indication for a significant increase in the quantum yield of localized excitons in suspended CNTs.

### Conclusion

In summary, we have presented studies of as-grown suspended CVD CNTs and their optical properties in comparison with our reference material of substrate supported CoMoCat CNTs. As-grown suspended CVD CNTs featured narrow emission profiles with stable PL energy. By analyzing photon emission statistics, we revealed their non-classical photon emission, which agree with our findings on the reference material and with Ref. [76, 77]. However, the PL emission of as-grown suspended CVD CNTs did not exhibit any indication for PL intermittency. In the reference material intermittency was apparent even on short timescales of 100 ns and resulted in a photon-bunching signature in the photon emission statistics. Furthermore, non-radiative decay of excitons was significantly inhibited in as-grown suspended CVD CNTs, which featured PL lifetimes close to the intrinsic exciton lifetime of  $\sim 10$  ns. Both findings qualify excitons in as-grown suspended CVD CNTs as intrinsically bright and came along with a significantly increased quantum yield.

Our results establish bright, long-lived and coherent quantum dot excitons as a new regime of CNT optics. Although the underlying microscopic origin is currently unknown, exciton localization emerged naturally in our as-grown suspended CVD CNTs. Analogous to color defects in bulk crystalline solids with discrete optical spectra, luminescent structural defects may constitute a class of quantum dots in semiconducting CNTs. Another candidate for accidental exciton trap formation would be a proximal charge impurity [62]. Such charge impurities were already identified in Chap. 4 as dominating for the optical properties of individual CNTs. In future application, such quantum dots could be intentionally induced in individual CNTs. Indication for the controlled variation of an electrostatically defined CNT quantum dot were already discussed in Chap. 4. However, such electrostatic traps could also be defined by close gates inducing inhomogeneous electric fields [179, 205]. Since similar was already achieved for layers of graphene Furthermore, also chemically functionalized CNTs could presumably feature the formation of topologically defined CNT quantum dots [206].

## Summary and perspectives

In the framework of this work semiconducting single-walled carbon nanotubes (CNTs) were investigated by means of optical spectroscopy down to cryogenic temperatures. The photoluminescence (PL) signal of individual CNTs was resolved temporally in correlation measurements or spectrally in non-resonant photoluminescence spectroscopy and photoluminescence excitation spectroscopy. An extensive setup was successfully established including a electronically controlled, stabilized laser setup, a Hanbury-Brown-and-Twiss interferometer and a confocal microscopy that operated at cryogenic temperature. Three different sample configurations were used to perform optical studies of individual CNTs at various temperatures (Chap. 3), on application of external electric fields (Chap. 4), and isolated from the environment (Chap. 5).

The optical spectroscopy of individual CNTs required distinct preparation of samples. These samples should feature CNTs with an appropriate diameter distribution - in order to record the PL emission with silicon based detectors - and an appropriate CNT surface density - in order to investigate single CNTs within the diffraction limited laser spot. The first point was accomplished by use of a commercially available CoMoCat CNTs comprising an ensemble of semiconducting CNTs with a sharp distribution of small diameter. Spin-coating of this solution on a substrate created a layer of individualized CNTs given an appropriate surface density, which was controlled via various process parameters. Employing substrates with a grid of lithographically defined metallic markers, we imaged such layers efficiently by complementary imaging techniques, viz. atomic force microscopy, scanning electron microscopy and confocal photoluminescence microscopy.

In addition to developing a systematic sample fabrication and characterization routine, experiments were performed to investigate PL spectra of individual CNTs at various temperatures. At cryogenic temperatures these spectra routinely exhibited an asymmetric emission profile, which became symmetric for higher temperatures. Further, we could identify a generally reduced PL energy at low temperatures. Both effects can be understood in terms of exciton localization. Due to low activation energy at cryogenic temperatures, exciton diffusion is highly constricted since exci-

## 5. Photon emission statistics

tons localize in presumably impurity induced trapping potentials. However, these traps become insignificant at higher temperatures as the excitons delocalize. Thus, a localized exciton features a reduced energy, which shifts the PL to the red for low temperature. Earlier work has attributed asymmetric line shape to arise from interaction of localized excitons with phonons. In our experiments we identified that the asymmetry was correlated with the localization potential, which suggested a common physical origin of both effects, i.e. the localization of excitons in CNT quantum dots.

In analogy to many nano-emitters like quantum dots or single molecules, the PL intensity of individual CNTs on substrate featured intermittency on time-scales from 100 ns up to minutes with a general power-law blinking statistics. Further, we analyzed traces of PL spectra with respect to spectral wandering. This probabilistic study revealed that the PL energy was statistically dependent on its past. Our findings indicate that spectral wandering arises from interaction with a few charge fluctuators located in the ambient dielectric medium rather than from interaction with a bath of fluctuators as it would be expected for excitons which diffuse freely along the mesoscopic length of a CNT. These spectral properties were insensitive to embedding CNTs in a metal-oxide-semiconductor (MOS) capacitor.

Designed for the implementation in cryogenic spectroscopy, a MOS capacitor device was realized to apply an electric field perpendicular to the CNT axis by means of a gate voltage. As a function of the applied field we observed quadratic red shifts of the PL energy, which arise from the transverse polarization of excitons. However, this effect was dominant only in CNTs exhibiting a single emission line (type A).

In contrast, type B CNTs featured a broken symmetry, which became apparent in PL spectra comprising satellite peaks. These satellite peaks could originate from mixing of bright (singlet) and dark (triplet) exciton states, presumably due to defect induced spin-orbit coupling. In response to the electric field type B CNTs showed a linear energy shift of singlet and triplet exciton lines, which exceeded aforementioned quadratic shifts of transverse polarization by far. This linear shift was interpreted in terms of a permanent dipole moment of localized excitons.

Using photoluminescence excitation spectroscopy, we found that excitation spectra of localized excitons featured resonances at phonon sidebands due to efficient exciton-phonon coupling, but also resonances at the harmonics of their fundamental trapping potential. In a CNT quantum dot, these resonances could be varied via the gate voltage of the MOS capacitor device, which indicates a controlled manipulation of the trapping potential for localized excitons. By tuning the trapping

potential systematically we observed efficient pumping of PL whenever the harmonics of the trapping energy were in resonance with the energy of a phonon (i.e. the radial breathing mode). This indicates that relaxation of excited "hot" excitons was mediated by coupling to phonons. Keyworded with "phonon bottleneck", the central role of exciton-phonon coupling for relaxation of "hot" exciton was reported earlier for semiconductor compound quantum dots.

Furthermore, a subset of type A CNTs featured the emergence of a satellite peak in response to the electric field. The energy splitting to the bright exciton agreed with previous experimental and theoretical reports on the emission from charged excitons (trions). In our experiments, trions were presumably created by doping of individual CNTs by means of the applied gate voltage. The emergence of trion emission quenched the emission from the bright exciton. It was reversible and could be robustly tuned via the applied gate voltage.

Further experiments considered as-grown suspended CNTs, which were isolated from the environment and were grown by chemical-vapor-deposition. Their optical properties were compared to those of substrate supported CoMoCat CNTs. In addition to PL spectroscopy these studies included also photon-counting and correlation measurements, which targeted on exciton lifetime and photon emission statistics of individual CNTs. Here, we employed a Hanbury-Brown and Twiss interferometer designed for featuring high detection efficiency with low cross-talk between the single-photon detectors. To the spectral properties, the broad asymmetric emission profile of substrate supported CNTs were contrasted by narrow emission lines of as-grown suspended CNTs, which were below the resolution of the spectrometer. PL emission from substrate suspended CNTs featured intermittency on a time scale of  $\sim 100$  ns. This intermittency was presumably driven by shelving to the dark exciton state or external fluctuations. Both were ineffective for as-grown suspended CVD CNTs featuring blinking-free PL emission even on the shortest timescales. However, signatures of photon anti-bunching were dominant in the photon emission statistics of both species though the exciton lifetime in as-grown suspended CNTs exceeded typical lifetimes in substrate deposited CNTs by one order of magnitude and were close to the intrinsic limit of  $\sim 10$  ns. Even for saturated PL emission the exciton lifetime was further constant in as-grown suspended CNTs. This was indicative for the effective suppression of any Auger-mediated secondary decay, which inhibited non-radiative PL quenching. Thus, non-classical light emission from as-grown suspended CNTs could be assigned to the formation of CNT quantum dots highly isolated from their environment. In summary, as-grown suspended CNTs feature narrow emission

## 5. Photon emission statistics

profiles, constantly bright PL emission, long exciton lifetime and a significantly increased quantum yield, which establishes bright, long-lived and coherent quantum dot excitons as a new regime of CNT optics.

In conclusion of our findings, the optical properties of individual CNTs were sensitive to intrinsic and extrinsic inhomogeneities that inhibited the free diffusion of excitons along the one-dimensional lattice. At cryogenic temperatures excitons localized in CNT quantum dots, which featured in analogy to their semiconductor compound equivalent non-classical photon emission, spectral wandering driven by a few charge fluctuators, and signatures of harmonic excitation resonances. Moreover, we found indication for manipulative variation of the localization potential for excitons. Further, CNT quantum dots in as-grown suspended CNTs feature long exciton lifetimes, narrow emission lines and a significantly increased quantum yield.

Such freely suspended CNTs could find versatile application in future experiments. Their high quantum yield could facilitate the construction of novel CNT lasers operating in the near infrared [207]. Also quantum dots in freely suspended CNTs could be manipulated specifically varying their localization potential by means of inhomogeneous electric fields of close electric gates [179,205]. Since as-grown suspended CNTs featured non-classical light emission even at high temperatures, they could find application in single photon sources and detectors [208]. In contrast to semiconductor compound quantum dots, emission and absorption of light in CNT quantum dots is intrinsically sensitive to the polarization (antenna effect), which could be a fruitful feature for manufacturing CNT based single-photon interfaces. Since these could operate at a tailored wavelength and at room temperature, such devices could implement quantum information processing into existing commercial glass-fiber-based telecommunication networks [209].

Also the workability of CNTs outclass semiconductor compound quantum dots as CNTs can be positioned by means of AFM tips [210,211]. This could be utilized, when individual CNTs are positioned in an optical cavity [212]. A task that has been achieved only hardly on semiconductor compound quantum dots [213,214]. Such experiments could also benefit from the well-defined phonon mode spectrum of individual CNTs. It would allow for optical cooling of mechanical modes [215]. Given effective coupling of electric and mechanical states - as it was realized in other quantum optical systems [216,217] - CNT quantum dots could open the door for carbon based quantum simulation and information processing.

# Appendix



# A. Notation and physical constants

## A.1. Physical and material constants

Symbol	Quantity	Value
$a_{cc}$	Carbon-carbon bond length	$1.42 \cdot 10^{-10}$ m
$c$	Speed of light	$2.998 \cdot 10^8$ m s <sup>-1</sup>
$E_g$	Band gap for Si	1.1 eV
$\epsilon_0$	Permittivity of free space	$8.859 \cdot 10^{-14}$ F cm <sup>-1</sup>
$\epsilon_{SiO_2}$	Dielectric constant of silicon oxide	3.9
$\epsilon_{Al_2O_3}$	Dielectric constant of aluminium oxide	9.1
$\hbar$	Reduced Planck constant	$6.582 \cdot 10^{-16}$ eV s
$k_B$	Boltzmann constant	$8.617 \cdot 10^{-5}$ eV K <sup>-1</sup>
$n_i^0$	Intrinsic carrier concentration for Si at 300 K	$1.45 \cdot 10^{10}$ cm <sup>-3</sup>
$q$	Elementary charge	$1.602 \cdot 10^{-19}$ C

## A.2. Symbols and abbreviations

Symbol	Quantity	Page
<b>A, B, E</b>	Irreducible line group representation	13
$\alpha_B$	Exciton Bohr radius	19
$\vec{a}_1, \vec{a}_2$	Basis vectors of direct graphene lattice	7
$\vec{b}_1, \vec{b}_2$	Basis vectors of indirect graphene lattice	9
$C$	Total capacitance of the MOS structure	53
$C_0$	Capacitance of the oxide layer	53
$C_{\min}$	Minimum capacitance of the MOS structure	56
$C_s$	Space charge capacitance	53
$\vec{C}_h, C_h$	Chiral vector, length of chiral vector	8
$\mathcal{C}$	Degree of correlation	61
$\Gamma, \Gamma_{\text{asy}}$	Symmetric and asymmetric line width	44
$\gamma_i$	Relaxation rate	24
$d_n$	Greatest common divisor of $n$ and $m$	11
$d_R$	Greatest common divisor of $2n + m$ and $2m + n$	8
$d_t$	Tube diameter	9
$\Delta$	Bin width	61
$\Delta_D$	Energy splitting between bright and dark exciton	25
$\Delta_K$	Energy splitting between bright and k-momentum exciton	26
$\Delta_{ST}$	Energy splitting between bright and triplet exciton	26
$\Delta_{\pm}$	Energy splitting between bright and charged exciton	27
$\delta_L$	Laser detuning	78
$\delta V$	Modulation amplitude voltage	56
$\delta(x)$	Dirac delta function	88
$\mathcal{D}(i)$	Irreducible representation in line group of $i$	13
$E_B$	Exciton binding energy	19
$E_{BGR}$	Energy shift due to band gap renormalization	19
$E_{PL}$	Photoluminescence energy	19
$\epsilon_{\text{med/vac}}$	Dielectric constant of CNT in medium/vacuum	18
$f$	Oscillator strength per carbon atom	106
$f_{\text{laser}}$	Repetition frequency of pulsed laser	96
$f_{\text{mod}}$	Modulation frequency	56
$F$	Strength of homogenous electric field	67
$\mathcal{F}_{\zeta}$	Exciton envelope function	22

Symbol	Quantity	Page
$f$	Force (electrostatic)	69
$\phi_s$	Surface potential	53
$\phi_{MS}$	Metal semiconductor work function difference	55
$g^{(2)}(\tau)$	Second-order correlation function	87
$\eta$	Contrast of photon anti-bunching	94
$I$	Intensity	86
$k_{\perp}, k_{\parallel}$	Vector components in the indirect CNT lattice	10
$\vec{K}_1, \vec{K}_2$	Basis vectors of the indirect CNT lattice	10
$L_D$	Debye length	54
$\lambda_{\text{exc}}$	Wavelength of excitation laser beam	33
$m, n$	Chiral indices	8
$m_0$	Free mass of the electron	106
$m^*$	Reduced exciton mass	19
$\mu, k$	(Quantized) wave vector components	10
$N$	Number of hexagons per CNT unit cell	9
$\mathcal{N}$	Number of independent photon emitters	91
$N_A$	Dopant concentration	53
$n(E)$	Density of states	16
$n$	Number of photons	86
$p$	Pressure (electrostatic)	69
$\Pi$	Parity under rotation of $180^\circ$	13
$r$	Photon counting rate	96
$S^\pm$	Binding energy of excess charge in singlet state	27
$s$	Total exciton spin	26
$\sigma$	Standard deviation	61
$\sigma_c$	Coherence length in units of $\alpha_B$	106
$\varsigma$	Energy level in hydrogen model	19
$T$	Temperature	31
$T_{\text{eff}}$	Effective temperature	59
$T^\pm$	Binding energy of excess charge in triplet state	27
$\vec{T},  \vec{T} $	Translation vector, length of translation vector	8
$t$	Time	88
$\tau$	Time delay	86
$\tau_0$	Exciton life-time	24
$\tau_{\text{ON/OFF}}$	Characteristic blinking times	90

A. Notation and physical constants

Symbol	Quantity	Page
$\theta$	Chiral angle	9
$Q_{\text{IT}}$	Surface density of interface trap states	55
$Q_s$	Net total charge density within the semiconductor	54
$Q_{\text{tot}}$	Total surface density of impurities	55
$Q_{\text{OT}}$	Surface density of oxide trap states	55
$V_g$	Gate voltage	55
$x_d$	Width of depletion region	54
$X$	Emission line of the bright exciton	24
$X^{\text{D}}$	Emission line of the dark exciton	25
$X^{\text{K}}$	Emission line of the k-momentum exciton	26
$X^{\text{T}}$	Emission line of the triplet exciton	26
$X^{\pm}$	Emission line of the charged exciton	27
$\chi_i$	Power-law exponent	62
$\xi$	Chiral variable	19
$\zeta$	Angle between linear polarization and CNT axis	41

## B. Exchange and trion binding energy

Chirality			Exchange energy	Trion binding energy			
$n$	$m$	$d_t$	$\Delta_{ST}$	$T^-$	$T^+$	$S^-$	$S^+$
		nm	meV	meV	meV	meV	meV
5	3	0.548	-	2.9	10.4	171.7	174.0
5	4	0.612	211.2	3.3	8.0	159.8	161.7
6	1	0.513	-	4.7	13.2	-	-
6	2	0.565	202.8	3.0	8.1	167.7	170.3
6	4	0.683	184.9	3.4	7.5	147.7	148.5
6	5	0.747	144.0	3.0	7.6	139.4	140.8
7	0	0.548	187.7	3.8	8.3	184.3	186.7
7	2	0.641	222.9	4.0	9.1	161.5	163.6
7	3	0.696	146.3	2.9	6.4	138.5	139.8
7	5	0.817	127.9	3.1	5.9	122.7	124.0
7	6	0.882	104.3	2.8	5.1	111.8	113.0
8	0	0.626	238.0	4.3	10.2	168.4	170.9
8	1	0.669	139.6	2.8	6.4	141.7	143.1
8	3	0.771	150.7	3.4	6.9	132.7	134.2
8	4	0.829	107.6	2.7	5.3	117.8	119.0
8	6	0.952	93.1	2.8	4.9	105.1	106.1
8	7	1.018	68.0	2.4	4.3	97.6	97.9
9	1	0.747	164.2	3.7	6.2	132.0	133.3
9	2	0.795	107.4	2.6	5.3	120.4	121.5
9	4	0.903	84.1	3.0	4.5	112.6	114.0
9	5	0.962	82.9	2.5	4.4	101.6	101.4
9	7	1.088	71.4	2.5	4.1	91.8	92.7
9	8	1.153	61.4	2.4	3.7	84.0	84.2
10	0	0.783	106.5	2.7	5.6	123.5	125.0
10	2	0.872	118.8	3.3	6.0	118.2	119.4
10	3	0.923	83.6	2.5	4.5	104.7	105.7

B. Exchange and trion binding energy

Chirality			Exchange energy	Trion binding energy			
$n$	$m$	$d_t$	$\Delta_{ST}$	$T^-$	$T^+$	$S^-$	$S^+$
		nm	meV	meV	meV	meV	meV
10	5	1.036	80.7	2.7	4.6	97.8	97.8
10	6	1.096	65.4	2.4	3.8	89.4	90.4
10	8	1.223	-	2.3	3.6	84.7	81.6
10	9	1.289	-	2.2	3.3	77.9	77.5
11	0	0.861	122.7	3.4	6.5	121.8	122.8
11	1	0.903	107.6	2.5	5.5	107.6	107.4
11	3	1.000	89.0	2.9	4.9	102.3	102.3
11	4	1.053	66.9	2.4	3.9	92.1	92.7
11	6	1.169	-	2.5	3.9	86.4	86.5
11	7	1.230	56.1	2.5	3.4	80.5	80.0
11	9	1.358	-	2.1	3.4	75.2	75.0
11	10	1.424	-	2.0	2.9	69.8	69.0
12	1	0.981	93.3	3.0	5.2	105.1	105.0
12	2	1.027	67.8	2.3	3.9	94.0	94.7
12	4	1.129	68.6	2.6	4.2	90.2	90.2
12	5	1.185	62.8	2.2	3.4	82.1	83.3
12	7	1.303	-	2.3	3.4	77.8	77.5
12	8	1.365	-	2.0	3.1	72.6	73.3
12	10	1.494	-	2.0	2.7	67.2	65.3
12	11	1.560	-	1.9	2.7	64.0	63.6

All values valid for  $\epsilon = 1.846$ .

NOTE: The values were gained from [55] and [81] by image processing techniques and rescaled to vacuum environment ( $\epsilon = 1.846$ ). As all there reported plots show the exchange interaction (trion binding energy) as a function of the tube diameter, the values between chiralities with similar or the same diameter could be interchanged within image processing. The missing values are not reported in the original publications.

## C. Protocol for fabrication of layers with individualized carbon nanotubes

### Sample cleaning

- To protect the wafer surfaces from mechanical damages (like scratches) it was covered with a protective varnish before it was cut into sample pieces of  $7 \times 7 \text{ mm}^2$  size.
- In order to clean the surface of the smaller sample pieces, they were rinsed with acetone and isopropanol to remove the varnish coating. Then the sample was placed in an isopropanol bath and ultra-sonicated for 20 minutes at maximum power. Finally, a stream of nitrogen gas dried the sample.
- An oxygen plasma (for 3 minutes) was used to remove any varnish leftovers and to make the surface hydrophobic. The hydrophobic nature of the surface was advantageous for the successive spin-coating of CNTs.

### Dilution of CNT solution

- The as-purchased CNT solution was diluted with a 5-10 mM aqueous solution of sodium cholate (sc). Thereby the mixing ratio determined substantially the density of CNT in the later formed CNT layer. Employing a systematic analysis based on complementary imaging techniques (see Chap. 3.3) we find a mixing ratio of 1 part as-purchased CNT solution to 18 parts sc solution results in a surface density of  $\sim 1 \text{ CNT per } \mu\text{m}^2$ .

### Spin-coating of CNTs

- A few droplets of the CNT solution were dropped on the cleaned sample surface to cover the entire sample and to form a drop of approximately 1 mm in height.

### *C. Protocol for fabrication of layers with individualized carbon nanotubes*

Due to the hydrophobic nature of the cleaned surface the drop did not flow over the sample edges during the following waiting time of 12 minutes.

- Later, the drop was spun off the surface using a commercial spin coater device. The spin-coating procedure consisted of two steps. A first acceleration step with 800 rotations per minute lasted for 3 seconds. The second step lasted at least 15 seconds with 3500 rotations per second. During this step we were able to observe the gradually shrinking thickness of the solution film on the surface. Due to thin film interference the surface changed its color along the rainbow spectrum several times. This was a helpful indication for a gradually shrinking solution film thickness resulting in a largely uniform layer of individualized CNTs. In contrast, a too high spin acceleration would spin off the entire solution drop without depositing an uniform CNT layer. After the spin-coating procedure possible tiny droplets in the corner of the sample surface were removed in a stream of nitrogen.

## D. Model for excitation of localized excitons

On the basis of our experimental findings presented in Chap. 4.7 we now modeled the PL intensity as a function of the applied voltage  $V_g$  and the laser detuning  $\delta_L$  since both parameters were independently controllable in our experiments. The PLE spectra of localized excitons were dominated by Lorentzian shaped resonances at multiples of a localization energy  $\Delta_a$ . The PL intensity  $I$  is then given by

$$I(\delta_L, \Delta_a) = I_0 \sum_{n=0}^{\infty} \frac{2}{\pi} \frac{\Gamma_a^2}{\Gamma_a^2 + 4(\delta_L - n \cdot \Delta_a)^2} . \quad (\text{D.1})$$

Due to a phonon bottleneck, higher excited exciton states relax efficiently when the harmonic trapping fits to the energy of the RBM mode  $\hbar\omega_{\text{RBM}}$ . In Fig. 4.21(b) our experimental data shows that  $\Gamma_a$  follows a Gaussian distribution that peaks at  $\Gamma_a^{\text{max}} = 41.7 \text{ meV} \approx \hbar\omega_{\text{RBM}}$ . When  $\Gamma_a$  is varied accordingly, we can plot  $I(\delta_L, \Delta_a)$  as a false color shown in Figure D.1(a). It features intensity resonances, where ever the harmonics of the trapping potential are multiples of the RBM phonon energy.

However, this simple simulation needs several expansions to mimic the experimental situation. We incorporate two attenuating effects on the PL intensity by adding factors to  $I(\delta_L, \Delta_a)$  in Eq. (D.1): the chromatic aberration of the used microscope and the sensitivity of the PL intensity on the localization potential.

The first factor is just of technical nature: An empirical factor  $\exp(-|\delta_L|/43 \text{ meV})$  takes account for the chromatic aberration of our setup. However, this factor becomes irrelevant if we consider experiments, which use a constant laser detuning as it was the case for the voltage sweep depicted in Fig. D.1(d).

In contrast, the second effect reflects directly the physical properties of localized excitons. As we will show below it is reasonable to introduce a quenching factor  $\cosh(\kappa\Delta_a)$  that accounts for the low PL intensity of weakly localized excitons.

Finally, we replace  $\Delta_a$  by  $V_g$  since only the gate voltage is experimentally controllable. To this end, we break down the macroscopic polarization of oxide charges  $Q_{\text{OT}}$  within our device to a microscopic level of a single oxide charge. Located in the

### D. Model for excitation of localized excitons

vicinity of a CNT such oxide charge state could provide for an inhomogenous electric field that is capable to create a sufficient localization potential for excitons [62,179]. As illustrated by the solid line in Fig. D.1(c), a Langevin function reproduces the experimentally confirmed interdependence between  $\Delta_a$  and  $V_g$ . This function is well known to describe other macroscopic polarization phenomena [97] and reads as

$$\Delta_a = \Delta_a^0 + b \left[ \coth(\xi V_g) - \frac{1}{\xi V_g} \right]. \quad (\text{D.2})$$

When we included these aspects to Eq. (D.1), the simulation reproduced the experimental findings of a voltage sweep as depicted by the solid line in Fig. D.1(d)<sup>1</sup>. This voltage sweep exhibited two local maxima in PL emission around  $V_g = -15$  V and 25 V, respectively. At these maxima,  $V_g$  mediated the localization in a man-

<sup>1</sup>This is the exactly same sweep which was also depicted in Fig. 4.12

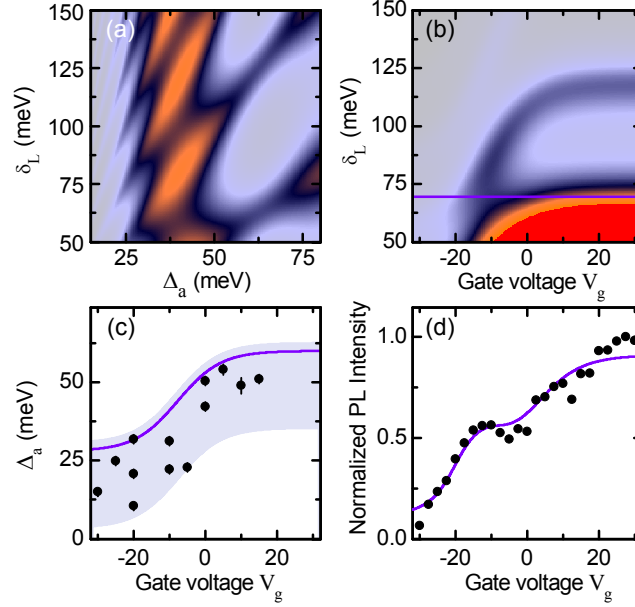


Figure D.1.: **Simulation of excitation spectra as a function of exciton localization potential:** (a) In false color plot: PL intensity given by the considered simple localization model as a function of localization potential  $\Delta_a$  and laser detuning  $\delta_L$  as given by Eq. (D.1). (b) For an expanded simulation the PL intensity plotted as a function of  $V_g$  and  $\delta_L$ , which were both controlled in the experiment. (c)  $\Delta_a$  as a function of the gate voltage  $V_g$ . Experimental data are depicted as filled circles. The purple solid line depicts the here considered switching behavior of Eq. (D.2). (d) PL intensity as a function of gate voltage  $V_g$ . The simulation of PL quenching (purple solid line) agrees with the experimental data points (filled circles).

ner such that a harmonic of  $\Delta_a$  was in resonance with the constant laser detuning  $\delta_L = 69.6$  meV. Hence, we tuned the coefficients in Eq. (D.2) so that they reproduced these resonance condition best. Fig. D.1(c) displays the most promising relation between  $\Delta_a$  and  $V_g$  as a solid purple line<sup>2</sup> that lies within the limits of typical fluctuations in  $\Delta_a$  (blue shaded area). We used a standard fitting routine and found for  $\kappa = 0.071$  meV<sup>-1</sup> the best agreement with our experimental data. Fig. D.1(b) summarizes the complete excitation map showing the PL intensity for any combination of  $\delta_L$  and  $V_g$ . The voltage sweep experiment considered here is marked as a purple solid line.

The simulation of such voltage sweeps is highly suitable to gain closer insight into the localization process because of two reasons. Firstly, the PL energy and the laser detuning  $\delta_L$  are both kept constant, so that the chromatic aberration of the microscope setup becomes irrelevant. And secondly, within the simulation the adjustment of the switching behavior sets only the general resonance conditions whereas the quenching coefficient  $\kappa$  alone reproduces the impact of a varied localization potential  $\Delta_a$  on the PL intensity  $I$ .

Experimental evidence suggests that the electric field of a charge impurity provides for the localization of excitons. Naumov et al. reported on the PL of (non-localized) excitons in an electric field *parallel* to the CNT axis [218]. Within their experiments, the PL intensity of a CNT was quenched as a function of a linear electric field  $F_{\parallel}$  as the electric force reduced the exciton binding energy and separated electron and hole. The PL intensity was found to scale with  $1/\cosh(kF_{\parallel})$  where the quenching parameter  $k$  was a function of the exciton binding energy and accordingly of the CNT chirality. It directly reflected the longitudinal polarizability of excitons in CNTs.

In contrast the (electric) localization potential was always resulting in an attractive force on the exciton. On the basis of Naumov's results, we assumed that the PL intensity increases with  $\cosh(\kappa\Delta_a)$  for a stiffer exciton localization. We brought our results in agreement with Naumov et al. by the following, simple calculation. The energy of a charge  $q$  in a homogenous electric field  $F_{\parallel}$  at position  $x$  is given by  $q \cdot F_{\parallel} \cdot x$ . To reduce the PL intensity significantly, the overlap between the wave functions of electron and hole must be reduced on a scale of the exciton Bohr radius  $\alpha_B$ , which is  $\sim 1.25$  nm for the investigated (8,3) CNT [34]. Hence, we can state for the localization energy

$$\Delta_a = q \cdot F_{\parallel} \cdot \sigma . \quad (\text{D.3})$$

---

<sup>2</sup>  $\Delta_a^0 = 43.8\text{meV}$        $\xi = 0.22 \text{ V}^{-1}$   
 $b = 18.8 \text{ meV}$        $V_0 = -7.8 \text{ V}$

#### D. Model for excitation of localized excitons

By comparing directly with Naumov et al. we obtained

$$\begin{aligned}k F_{\parallel} &= \kappa \Delta_a = \kappa \cdot q \cdot F_{\parallel} \cdot \sigma \\k &= \kappa \cdot q \cdot \sigma = 89 \text{ nmV}^{-1} .\end{aligned}\tag{D.4}$$

This value reproduced a quenching coefficient of  $68 \text{ nmV}^{-1}$  reported for a CNT of the same chirality [218].

In summary, variation of the localization potential establishes a new experimental method, which is capable for investigating excitons localized in CNT quantum dots. As this method employs a constant excitation wavelength, it overcomes any drawbacks with regard to chromaticity of the optical setup that impairs the usability of well-established PLE spectroscopy. A simple simulation on the basis of a harmonic localization potential reproduced the quenching of PL as a function of the applied gate voltage  $V_g$ . Within this simulation we evaluated a quenching coefficient for weakly localized excitons, which agrees with previous reports on the decomposition of (non-localized) excitons in longitudinal electric fields.

# List of Figures

0.1. A metal-oxide-semiconductor capacitor for spectroscopy of individual carbon nanotubes . . . . .	III
2.1. Construction of a carbon nanotube from a layer of graphene . . . . .	8
2.2. Reciprocal lattice of three different carbon nanotubes . . . . .	11
2.3. Symmetry for chiral, zig-zag and armchair carbon nanotubes . . . . .	12
2.4. Electronic properties of graphene . . . . .	13
2.5. Density of states and Kataura plot . . . . .	17
2.6. Theoretical values for binding energy and exciton energy splitting . .	20
2.7. Electron and exciton states in chiral CNTs . . . . .	21
2.8. Energy splittings to the bright exciton . . . . .	28
3.1. Confocal microscope setup . . . . .	31
3.2. Laser beam line . . . . .	33
3.3. Performance characteristics of the stabilized laser setup . . . . .	34
3.4. Sample layouts I . . . . .	35
3.5. Complementary imaging . . . . .	38
3.6. Photoluminescence of a single carbon nanotube . . . . .	40
3.7. Spectra of individual CNTs at various temperatures . . . . .	43
4.1. Sample layouts II . . . . .	48
4.2. Fabrication of a semi-transparent top gate . . . . .	50
4.3. Ohmic contacts . . . . .	51
4.4. Charge density $Q_s$ and depletion width $x_d$ . . . . .	53
4.5. CV characteristics of the MOS capacitor device . . . . .	56
4.6. Estimation of the oxide charge density . . . . .	58
4.7. Spectra and time traces for CNTs on the MOS capacitor samples . .	60
4.8. Jitter correlation in PL time traces . . . . .	61
4.9. Intermittency and spectral drifting . . . . .	63
4.10. Example spectra for type A and type B CNTs . . . . .	64
4.11. Energy splittings in two-peaked emission spectra . . . . .	65

*List of Figures*

4.12. Polarizability and reversible PL quenching . . . . .	68
4.13. Transverse polarizability of CNTs . . . . .	69
4.14. Permanent dipole moment of an individual CNT - part I . . . . .	71
4.15. Permanent dipole moment of an individual CNT - part II . . . . .	72
4.16. State mixing and permanent dipole moment . . . . .	73
4.17. Voltage-induced trion generation in a single carbon nanotube . . . . .	75
4.18. Complete hierarchy of low-energetic PL emission . . . . .	77
4.19. Photoluminescence excitation spectra revealing exciton localization . . . . .	79
4.20. Variation of the exciton localization by the electric field . . . . .	82
4.21. Phonon bottleneck . . . . .	83
5.1. Blinking . . . . .	88
5.2. Expected photon statistics . . . . .	93
5.3. Normalized correlation histogram of an intense pulse light source . . . . .	95
5.4. Schematic setup of the intensity interferometer . . . . .	98
5.5. Cross talk between avalanche photo-detectors . . . . .	100
5.6. Sample layouts III . . . . .	102
5.7. CoMoCat CNTs on substrate and as-grown suspended CVD CNTs . . . . .	103
5.8. Spectral properties of suspended CVD CNTs . . . . .	105
5.9. Exciton lifetime in suspended CVD CNTs . . . . .	107
5.10. Spectra and photon emission statistics of CoMoCat CNTs and as-grown suspended CVD CNTs . . . . .	108
5.11. Time-resolved properties of CoMoCat CNTs . . . . .	110
5.12. Photoluminescence saturation . . . . .	111
D.1. Simulation of excitation spectra as a function of exciton localization potential . . . . .	128

## List of Tables

2.1. Exciton states in chiral carbon nanotubes . . . . .	22
5.1. Detection efficiency and cross talk . . . . .	101



## Bibliography

- [1] V. Radushkevich and V. M. Lukyanovich, “О Структуре Углерда Образующегося При Термическм Разлжении Окиси Углерда На Железном Кнтакте,” *Журнал Физическй Химии (Soviet Journal of Physical Chemistry)*, vol. 26, pp. 88–95, 1952.
- [2] S. Iijima, “Helical microtubules of graphitic carbon,” *Nature*, vol. 354, pp. 56–58, Nov. 1991.
- [3] M. Dresselhaus, G. Dresselhaus, and R. Saito, “Physics of carbon nanotubes,” *Carbon*, vol. 33, no. 7, pp. 883–891, 1995.
- [4] J. L. Bahr and J. M. Tour, “Covalent chemistry of single-wall carbon nanotubes,” *J. Mater. Chem.*, vol. 12, no. 7, pp. 1952–1958, 2002.
- [5] E. T. Thostenson, Z. Ren, and T.-W. Chou, “Advances in the science and technology of carbon nanotubes and their composites: a review,” *Composites Science and Technology*, vol. 61, pp. 1899–1912, Oct. 2001.
- [6] A. Bachtold, P. Hadley, T. Nakanishi, and C. Dekker, “Logic circuits with carbon nanotube transistors,” *Science*, vol. 294, no. 5545, pp. 1317–1320, 2001.
- [7] K. Balasubramanian and M. Burghard, “Biosensors based on carbon nanotubes,” *Analytical and Bioanalytical Chemistry*, vol. 385, no. 3, pp. 452–468, 2006.
- [8] T. A. Hilder and J. M. Hill, “Carbon nanotubes as drug delivery nanocapsules,” *Current Applied Physics*, vol. 8, pp. 258–261, May 2008.
- [9] S. Madani, N. Naderi, O. Dissanayake, A. Tan, and A. Seifalian, “A new era of cancer treatment: carbon nanotubes as drug delivery tools,” *International Journal of Nanomedicine*, vol. 6, pp. 2963–2979, 2011.
- [10] A. Jorio, G. Dresselhaus, and M. S. Dresselhaus, *Carbon Nanotubes: Advanced Topics in the Synthesis, Structure, Properties and Applications*. Springer Verlag, Berlin, 1 ed., 2007.

## Bibliography

- [11] B. Yakobson and P. Avouris, "Mechanical properties of carbon nanotubes," in *Topics in Applied Physics* (M. Dresselhaus, G. Dresselhaus, and P. Avouris, eds.), vol. 80, pp. 287–327–, Springer Berlin Heidelberg, 2001.
- [12] B. Demczyk, Y. Wang, J. Cumings, M. Hetman, W. Han, A. Zettl, and R. Ritchie, "Direct mechanical measurement of the tensile strength and elastic modulus of multiwalled carbon nanotubes," *Materials Science and Engineering: A*, vol. 334, pp. 173–178, Sept. 2002.
- [13] M.-F. Yu, O. Lourie, M. J. Dyer, K. Moloni, T. F. Kelly, and R. S. Ruoff, "Strength and breaking mechanism of multiwalled carbon nanotubes under tensile load," *Science*, vol. 287, no. 5453, pp. 637–640, 2000.
- [14] S. R. Bakshi, D. Lahiri, and A. Agarwal, "Carbon nanotube reinforced metal matrix composites - a review," *International Materials Reviews*, vol. 55, no. 1, pp. 41–64, 2010.
- [15] P. Harris, "Carbon nanotube composites," *International Materials Reviews*, vol. 49, no. 1, pp. 31–43, 2004.
- [16] N.N., "Production and applications of carbon nanotubes, carbon nanofibers, fullerenes, graphene and nanodiamonds: A global technology survey and market analysis, report code et113," tech. rep., Innovative Research and Production Inc., Feb 2011.
- [17] T. W. Odom, J.-L. Huang, P. Kim, and C. M. Lieber, "Atomic structure and electronic properties of single-walled carbon nanotubes," *Nature*, vol. 391, pp. 62–64, Jan. 1998.
- [18] J. W. G. Wildoer, L. C. Venema, A. G. Rinzler, R. E. Smalley, and C. Dekker, "Electronic structure of atomically resolved carbon nanotubes," *Nature*, vol. 391, pp. 59–62, Jan. 1998.
- [19] H. Kataura, Y. Kumazawa, Y. Maniwa, I. Umezu, S. Suzuki, Y. Ohtsuka, and Y. Achiba, "Optical properties of single-wall carbon nanotubes," *Synthetic Metals*, vol. 103, pp. 2555–2558, June 1999.
- [20] X. Zhao, Y. Liu, S. Inoue, T. Suzuki, R. O. Jones, and Y. Ando, "Smallest carbon nanotube is 3 ångstrom in diameter," *Phys. Rev. Lett.*, vol. 92, pp. 125502–, Mar. 2004.

- [21] X. Wang, Q. Li, J. Xie, Z. Jin, J. Wang, Y. Li, K. Jiang, and S. Fan, "Fabrication of ultralong and electrically uniform single-walled carbon nanotubes on clean substrates," *Nano Lett.*, vol. 9, pp. 3137–3141, Aug. 2009.
- [22] J. Hu, T. W. Odom, and C. M. Lieber, "Chemistry and physics in one dimension: Synthesis and properties of nanowires and nanotubes," *Acc. Chem. Res.*, vol. 32, pp. 435–445, Feb. 1999.
- [23] J. Voit, "One-dimensional fermi liquids," *Reports on Progress in Physics*, vol. 58, no. 9, p. 977, 1995.
- [24] M. J. O'Connell, S. M. Bachilo, C. B. Huffman, V. C. Moore, M. S. Strano, E. H. Haroz, K. L. Rialon, P. J. Boul, W. H. Noon, C. Kittrell, J. Ma, R. H. Hauge, R. B. Weisman, and R. E. Smalley, "Band gap fluorescence from individual single-walled carbon nanotubes," *Science*, vol. 297, no. 5581, pp. 593–596, 2002.
- [25] S. M. Bachilo, M. S. Strano, C. Kittrell, R. H. Hauge, R. E. Smalley, and R. B. Weisman, "Structure-assigned optical spectra of single-walled carbon nanotubes," *Science*, vol. 298, no. 5602, pp. 2361–2366, 2002.
- [26] A. Hartschuh, H. N. Pedrosa, L. Novotny, and T. D. Krauss, "Simultaneous fluorescence and raman scattering from single carbon nanotubes," *Science*, vol. 301, no. 5638, pp. 1354–1356, 2003.
- [27] J. Lefebvre, J. M. Fraser, P. Finnie, and Y. Homma, "Photoluminescence from an individual single-walled carbon nanotube," *Phys. Rev. B*, vol. 69, pp. 075403–, Feb. 2004.
- [28] A. Kongkanand, R. Martinez Dominguez, and P. V. Kamat, "Single wall carbon nanotube scaffolds for photoelectrochemical solar cells. capture and transport of photogenerated electrons," *Nano Lett.*, vol. 7, pp. 676–680, Feb. 2007.
- [29] P. Avouris, M. Freitag, and V. Perebeinos, "Carbon-nanotube photonics and optoelectronics," *Nature Photonics*, vol. 2, pp. 341–350, June 2008.
- [30] T. Ando, "Excitons in carbon nanotubes," *Journal of the Physical Society of Japan*, vol. 66, no. 4, pp. 1066–1073, 1997.
- [31] C. D. Spataru, S. Ismail-Beigi, L. X. Benedict, and S. G. Louie, "Excitonic effects and optical spectra of single-walled carbon nanotubes," *Phys. Rev. Lett.*, vol. 92, pp. 077402–, Feb. 2004.

## Bibliography

- [32] E. Chang, G. Bussi, A. Ruini, and E. Molinari, “Excitons in carbon nanotubes: An *Ab Initio* symmetry-based approach,” *Phys. Rev. Lett.*, vol. 92, p. 196401, May 2004.
- [33] V. Perebeinos, J. Tersoff, and P. Avouris, “Scaling of excitons in carbon nanotubes,” *Phys. Rev. Lett.*, vol. 92, pp. 257402–, June 2004.
- [34] R. B. Capaz, C. D. Spataru, S. Ismail-Beigi, and S. G. Louie, “Diameter and chirality dependence of exciton properties in carbon nanotubes,” *Phys. Rev. B*, vol. 74, p. 121401, Sep 2006.
- [35] G. Dukovic, F. Wang, D. Song, M. Y. Sfeir, T. F. Heinz, and L. E. Brus, “Structural dependence of excitonic optical transitions and band-gap energies in carbon nanotubes,” *Nano Letters*, vol. 5, no. 11, pp. 2314–2318, 2005.
- [36] J. Maultzsch, R. Pomraenke, S. Reich, E. Chang, D. Prezzi, A. Ruini, E. Molinari, M. S. Strano, C. Thomsen, and C. Lienau, “Exciton binding energies in carbon nanotubes from two-photon photoluminescence,” *Phys. Rev. B*, vol. 72, pp. 241402–, Dec. 2005.
- [37] F. Wang, G. Dukovic, L. E. Brus, and T. F. Heinz, “The optical resonances in carbon nanotubes arise from excitons,” *Science*, vol. 308, no. 5723, pp. 838–841, 2005.
- [38] E. B. Barros, R. B. Capaz, A. Jorio, G. G. Samsonidze, A. G. S. Filho, S. Ismail-Beigi, C. D. Spataru, S. G. Louie, G. Dresselhaus, and M. S. Dresselhaus, “Selection rules for one- and two-photon absorption by excitons in carbon nanotubes,” *Phys. Rev. B*, vol. 73, pp. 241406–4, June 2006.
- [39] I. B. Mortimer and R. J. Nicholas, “Role of bright and dark excitons in the temperature-dependent photoluminescence of carbon nanotubes,” *Phys. Rev. Lett.*, vol. 98, p. 027404, Jan 2007.
- [40] J. Shaver, J. Kono, O. Portugall, V. Krstic, G. L. J. A. Rikken, Y. Miyauchi, S. Maruyama, and V. Perebeinos, “Magnetic brightening of carbon nanotube photoluminescence through symmetry breaking,” *Nano Letters*, vol. 7, pp. 1851–1855, July 2007.
- [41] A. Srivastava, H. Htoon, V. I. Klimov, and J. Kono, “Direct observation of dark excitons in individual carbon nanotubes: Inhomogeneity in the exchange splitting,” *Phys. Rev. Lett.*, vol. 101, p. 087402, Aug 2008.

- [42] O. N. Torrens, M. Zheng, and J. M. Kikkawa, “Energy of k-momentum dark excitons in carbon nanotubes by optical spectroscopy,” *Phys. Rev. Lett.*, vol. 101, p. 157401, Oct 2008.
- [43] R. Matsunaga, K. Matsuda, and Y. Kanemitsu, “Evidence for dark excitons in a single carbon nanotube due to the aharonov-bohm effect,” *Phys. Rev. Lett.*, vol. 101, p. 147404, Oct 2008.
- [44] H. Harutyunyan, T. Gokus, A. A. Green, M. C. Hersam, M. Allegrini, and A. Hartschuh, “Defect-induced photoluminescence from dark excitonic states in individual single-walled carbon nanotubes,” *Nano Lett.*, vol. 9, pp. 2010–2014, Mar. 2009.
- [45] R. Matsunaga, K. Matsuda, and Y. Kanemitsu, “Origin of low-energy photoluminescence peaks in single carbon nanotubes: K-momentum dark excitons and triplet dark excitons,” *Phys. Rev. B*, vol. 81, pp. 033401–, Jan. 2010.
- [46] A. D. Mohite, T. S. Santos, J. S. Moodera, and B. W. Alphenaar, “Observation of the triplet exciton in eus-coated single-walled nanotubes,” *Nat Nano*, vol. 4, pp. 425–429, July 2009.
- [47] R. Matsunaga, K. Matsuda, and Y. Kanemitsu, “Observation of charged excitons in hole-doped carbon nanotubes using photoluminescence and absorption spectroscopy,” *Phys. Rev. Lett.*, vol. 106, pp. 037404–, Jan. 2011.
- [48] S. Ghosh, S. M. Bachilo, R. A. Simonette, K. M. Beckingham, and R. B. Weisman, “Oxygen doping modifies near-infrared band gaps in fluorescent single-walled carbon nanotubes,” *Science*, vol. 330, no. 6011, pp. 1656–1659, 2010.
- [49] S. M. Santos, B. Yuma, S. Berciaud, J. Shaver, M. Gallart, P. Gilliot, L. Cognet, and B. Lounis, “All-optical trion generation in single-walled carbon nanotubes,” *Phys. Rev. Lett.*, vol. 107, pp. 187401–, Oct. 2011.
- [50] J. S. Park, Y. Hirana, S. Mouri, Y. Miyauchi, N. Nakashima, and K. Matsuda, “Observation of negative and positive triions in the electrochemically carrier-doped single-walled carbon nanotubes,” *J. Am. Chem. Soc.*, vol. 134, pp. 14461–14466, Aug. 2012.
- [51] Y. Miyauchi, M. Iwamura, S. Mouri, T. Kawazoe, M. Ohtsu, and K. Matsuda, “Brightening of excitons in carbon nanotubes on dimensionality modification,” *Nat Photon*, vol. 7, pp. 715–719, Sept. 2013.

## Bibliography

- [52] Y. Kanemitsu, “Excitons in semiconducting carbon nanotubes: diameter-dependent photoluminescence spectra,” *Phys. Chem. Chem. Phys.*, vol. 13, no. 33, pp. 14879–14888, 2011.
- [53] E. B. Barros, A. Jorio, G. G. Samsonidze, R. B. Capaz, A. G. Souza Filho, J. Mendes Filho, G. Dresselhaus, and M. S. Dresselhaus, “Review on the symmetry-related properties of carbon nanotubes,” *Physics Reports*, vol. 431, pp. 261–302, Sept. 2006.
- [54] R. B. Capaz, C. D. Spataru, P. Tangney, M. L. Cohen, and S. G. Louie, “Temperature dependence of the band gap of semiconducting carbon nanotubes,” *Phys. Rev. Lett.*, vol. 94, pp. 036801–, Jan. 2005.
- [55] R. B. Capaz, C. D. Spataru, S. Ismail-Beigi, and S. G. Louie, “Excitons in carbon nanotubes: Diameter and chirality trends,” *phys. stat. sol. (b)*, vol. 244, no. 11, pp. 4016–4020, 2007.
- [56] T. F. Rønnow, T. G. Pedersen, and H. D. Cornean, “Correlation and dimensional effects of trions in carbon nanotubes,” *Phys. Rev. B*, vol. 81, pp. 205446–, May 2010.
- [57] T. F. Rønnow, T. G. Pedersen, and H. D. Cornean, “Dimensional and correlation effects of charged excitons in low-dimensional semiconductors,” *Journal of Physics A: Mathematical and Theoretical*, vol. 43, no. 47, p. 474031, 2010.
- [58] A. Hartschuh, H. Qian, A. J. Meixner, N. Anderson, and L. Novotny, “Nanoscale optical imaging of excitons in single-walled carbon nanotubes,” *Nano Letters*, vol. 5, pp. 2310–2313, Nov. 2005.
- [59] C. Galland, A. Hoge, H. E. Tureci, and A. Imamoglu, “Non-markovian decoherence of localized nanotube excitons by acoustic phonons,” *Physical Review Letters*, vol. 101h, no. 6, p. 067402, 2008.
- [60] J. Lefebvre, P. Finnie, and Y. Homma, “Temperature-dependent photoluminescence from single-walled carbon nanotubes,” *Phys. Rev. B*, vol. 70, pp. 045419–, July 2004.
- [61] C. Georgi, M. Böhmler, H. Qian, L. Novotny, and A. Hartschuh, “Probing exciton propagation and quenching in carbon nanotubes with near-field optical microscopy,” *phys. stat. sol. (b)*, vol. 246, no. 11-12, pp. 2683–2688, 2009.

- [62] B. O. Tayo and S. V. Rotkin, “Charge impurity as a localization center for singlet excitons in single-wall nanotubes,” *Phys. Rev. B*, vol. 86, pp. 125431–, Sept. 2012.
- [63] J. J. Crochet, J. G. Duque, J. H. Werner, and S. K. Doorn, “Photoluminescence imaging of electronic-impurity-induced exciton quenching in single-walled carbon nanotubes,” *Nature Nanotechnology*, vol. advance online publication, pp. –, Jan. 2012.
- [64] C. D. Spataru, S. Ismail-Beigi, R. B. Capaz, and S. G. Louie, “Theory and ab initio calculation of radiative lifetime of excitons in semiconducting carbon nanotubes,” *Phys. Rev. Lett.*, vol. 95, pp. 247402–, Dec. 2005.
- [65] V. Perebeinos, J. Tersoff, and P. Avouris, “Radiative lifetime of excitons in carbon nanotubes,” *Nano Lett.*, vol. 5, pp. 2495–2499, Nov. 2005.
- [66] J. Xie, T. Inaba, R. Sugiyama, and Y. Homma, “Intrinsic diffusion length of excitons in long single-walled carbon nanotubes from photoluminescence spectra,” *Phys. Rev. B*, vol. 85, pp. 085434–, Feb. 2012.
- [67] S. Moritsubo, T. Murai, T. Shimada, Y. Murakami, S. Chiashi, S. Maruyama, and Y. K. Kato, “Exciton diffusion in air-suspended single-walled carbon nanotubes,” *Phys. Rev. Lett.*, vol. 104, pp. 247402–, June 2010.
- [68] L. Luer, S. Hoseinkhani, D. Polli, J. Crochet, T. Hertel, and G. Lanzani, “Size and mobility of excitons in (6, 5) carbon nanotubes,” *Nat Phys*, vol. 5, pp. 54–58, Jan. 2009.
- [69] F. Wang, G. Dukovic, E. Knoesel, L. E. Brus, and T. F. Heinz, “Observation of rapid auger recombination in optically excited semiconducting carbon nanotubes,” *Phys. Rev. B*, vol. 70, pp. 241403–, Dec. 2004.
- [70] Y.-Z. Ma, M. W. Graham, G. R. Fleming, A. A. Green, and M. C. Hersam, “Ultrafast exciton dephasing in semiconducting single-walled carbon nanotubes,” *Phys. Rev. Lett.*, vol. 101, pp. 217402–, Nov. 2008.
- [71] J. Lefebvre, D. G. Austing, J. Bond, and P. Finnie, “Photoluminescence imaging of suspended single-walled carbon nanotubes,” *Nano Letters*, vol. 6, pp. 1603–1608, Aug. 2006.

## Bibliography

- [72] G. Dukovic, B. E. White, Z. Zhou, F. Wang, S. Jockusch, M. L. Steigerwald, T. F. Heinz, R. A. Friesner, N. J. Turro, and L. E. Brus, “Reversible surface oxidation and efficient luminescence quenching in semiconductor single-wall carbon nanotubes,” *J. Am. Chem. Soc.*, vol. 126, pp. 15269–15276, Oct. 2004.
- [73] L. Cognet, D. A. Tsyboulski, J.-D. R. Rocha, C. D. Doyle, J. M. Tour, and R. B. Weisman, “Stepwise quenching of exciton fluorescence in carbon nanotubes by single-molecule reactions,” *Science*, vol. 316, no. 5830, pp. 1465–1468, 2007.
- [74] B. F. Habenicht and O. V. Prezhdo, “Nonradiative quenching of fluorescence in a semiconducting carbon nanotube: A time-domain ab-initio study,” *Phys. Rev. Lett.*, vol. 100, pp. 197402–, May 2008.
- [75] P. L. McEuen, M. Bockrath, D. H. Cobden, Y.-G. Yoon, and S. G. Louie, “Disorder, pseudospins, and backscattering in carbon nanotubes,” *Phys. Rev. Lett.*, vol. 83, pp. 5098–, Dec. 1999.
- [76] A. Högele, C. Galland, M. Winger, and A. Imamoglu, “Photon antibunching in the photoluminescence spectra of a single carbon nanotube,” *Phys. Rev. Lett.*, vol. 100, pp. 217401–4, May 2008.
- [77] W. Walden-Newman, I. Sarpkaya, and S. Strauf, “Quantum light signatures and nanosecond spectral diffusion from cavity-embedded carbon nanotubes,” *Nano Lett.*, vol. 12, pp. 1934–1941, Mar. 2012.
- [78] A. H. Castro Neto and F. Guinea, “Impurity-induced spin-orbit coupling in graphene,” *Phys. Rev. Lett.*, vol. 103, pp. 026804–, July 2009.
- [79] S. Konabe and K. Watanabe, “Mechanism for optical activation of dark spin-triplet excitons in hydrogenated single-walled carbon nanotubes,” *Phys. Rev. B*, vol. 83, pp. 045407–, Jan. 2011.
- [80] V. Perebeinos, J. Tersoff, and P. Avouris, “Effect of exciton-phonon coupling in the calculated optical absorption of carbon nanotubes,” *Phys. Rev. Lett.*, vol. 94, pp. 027402–, Jan. 2005.
- [81] T. F. Rønnow, T. G. Pedersen, and H. D. Cornean, “Stability of singlet and triplet trions in carbon nanotubes,” *Physics Letters A*, vol. 373, pp. 1478–1481, Apr. 2009.

- [82] I. V. Bondarev, L. M. Woods, and K. Tatur, “Strong exciton-plasmon coupling in semiconducting carbon nanotubes,” *Phys. Rev. B*, vol. 80, pp. 085407–, Aug. 2009.
- [83] H. Htoon, M. J. O’Connell, S. K. Doorn, and V. I. Klimov, “Single carbon nanotubes probed by photoluminescence excitation spectroscopy: The role of phonon-assisted transitions,” *Phys. Rev. Lett.*, vol. 94, pp. 127403–, Apr. 2005.
- [84] S. Lebedkin, F. Hennrich, O. Kiowski, and M. M. Kappes, “Photophysics of carbon nanotubes in organic polymer-toluene dispersions: Emission and excitation satellites and relaxation pathways,” *Phys. Rev. B*, vol. 77, pp. 165429–, Apr. 2008.
- [85] F. Plentz, H. B. Ribeiro, A. Jorio, M. S. Strano, and M. A. Pimenta, “Direct experimental evidence of exciton-phonon bound states in carbon nanotubes,” *Phys. Rev. Lett.*, vol. 95, pp. 247401–, Dec. 2005.
- [86] S. Chou, H. Ribeiro, E. Barros, A. Santos, D. Nezich, G. Samsonidze, C. Fantini, M. Pimenta, A. Jorio, F. P. Filho, M. Dresselhaus, G. Dresselhaus, R. Saito, M. Zheng, G. Onoa, E. Semke, A. Swan, and B. Goldberg, “Optical characterization of dna-wrapped carbon nanotube hybrids,” *Chemical Physics Letters*, vol. 397, pp. 296–301, 2004.
- [87] O. Kiowski, K. Arnold, S. Lebedkin, F. Hennrich, and M. M. Kappes, “Direct observation of deep excitonic states in the photoluminescence spectra of single-walled carbon nanotubes,” *Phys. Rev. Lett.*, vol. 99, pp. 237402–, Dec. 2007.
- [88] R. B. Weisman and S. M. Bachilo, “Dependence of optical transition energies on structure for single-walled carbon nanotubes in aqueous suspension: An empirical kataura plot,” *Nano Letters*, vol. 3, pp. 1235–1238, Sept. 2003.
- [89] C. Santori, M. Pelton, G. Solomon, Y. Dale, and Y. Yamamoto, “Triggered single photons from a quantum dot,” *Phys. Rev. Lett.*, vol. 86, pp. 1502–1505, Feb. 2001.
- [90] R. Saito, G. Dresselhaus, and M. Dresselhaus, *Physical Properties of Carbon Nanotubes*. Imperial College Press, 1998.
- [91] M. Hofmann, “Wachstum und Charakterisierung von Kohlenstoff-Nanoröhren,” Master’s thesis, Fakultät für Physik an der Ludwig-Maximilians-Universität München, 2010.

## Bibliography

- [92] M. Damnjanovic, I. Milosevic, T. Vukovic, and R. Sredanovic, “Full symmetry, optical activity, and potentials of single-wall and multiwall nanotubes,” *Phys. Rev. B*, vol. 60, pp. 2728–2739, July 1999.
- [93] H. Haken and H. C. Wolf, *Molekülphysik und Quantenchemie: Einführung in die experimentellen und theoretischen Grundlagen*, vol. 5. Springer-Verlag Berlin Heidelberg, 2006.
- [94] S. Reich, J. Maultzsch, C. Thomsen, and P. Ordejon, “Tight-binding description of graphene,” *Phys. Rev. B*, vol. 66, pp. 035412–, July 2002.
- [95] M. S. Dresselhaus, G. Dresselhaus, and P. Avouris, eds., *Carbon Nanotubes: Synthesis, Structure, Properties, and Applications*. Springer, 2001.
- [96] J. W. Mintmire and C. T. White, “Universal density of states for carbon nanotubes,” *Phys. Rev. Lett.*, vol. 81, pp. 2506–2509, Sept. 1998.
- [97] N. W. Ashcroft and D. N. Mermin, *Solid State Physics*. Toronto: Oldenbourg Verlag, 1 ed., Jan. 2001.
- [98] S. Maruyama. [www.photon.t.u-tokyo.ac.jp/maruyama/kataura/kataura.html](http://www.photon.t.u-tokyo.ac.jp/maruyama/kataura/kataura.html).
- [99] H. Ajiki and T. Ando, “Aharonov-bohm effect in carbon nanotubes,” *Physica B: Condensed Matter*, vol. 201, pp. 349–352, July 1994.
- [100] Y. Miyauchi, M. Oba, and S. Maruyama, “Cross-polarized optical absorption of single-walled nanotubes by polarized photoluminescence excitation spectroscopy,” *Phys. Rev. B*, vol. 74, pp. 205440–, Nov. 2006.
- [101] A. G. Walsh, A. Nickolas Vamivakas, Y. Yin, S. B. Cronin, M. Selim Ünlü, B. B. Goldberg, and A. K. Swan, “Scaling of exciton binding energy with external dielectric function in carbon nanotubes,” *Physica E: Low-dimensional Systems and Nanostructures*, vol. 40, pp. 2375–2379, May 2008.
- [102] C. L. Kane and E. J. Mele, “Electron interactions and scaling relations for optical excitations in carbon nanotubes,” *Phys. Rev. Lett.*, vol. 93, pp. 197402–, Nov. 2004.
- [103] R. J. Elliott, “Intensity of optical absorption by excitons,” *Phys. Rev.*, vol. 108, pp. 1384–1389, Dec. 1957.

- [104] V. C. Moore, M. S. Strano, E. H. Haroz, R. H. Hauge, R. E. Smalley, J. Schmidt, and Y. Talmon, "Individually suspended single-walled carbon nanotubes in various surfactants," *Nano Lett.*, vol. 3, pp. 1379–1382, Sept. 2003.
- [105] T. Hertel, A. Hagen, V. Talalaev, K. Arnold, F. Hennrich, M. Kappes, S. Rosenthal, J. McBride, H. Ulbricht, and E. Flahaut, "Spectroscopy of single- and double-wall carbon nanotubes in different environments," *Nano Lett.*, vol. 5, pp. 511–514, Feb. 2005.
- [106] Y. Ohno, S. Iwasaki, Y. Murakami, S. Kishimoto, S. Maruyama, and T. Mizutani, "Excitonic transition energies in single-walled carbon nanotubes: Dependence on environmental dielectric constant," *phys. stat. sol. (b)*, vol. 244, no. 11, pp. 4002–4005, 2007.
- [107] T. Ando, "Environment effects on excitons in semiconducting carbon nanotubes," *Journal of the Physical Society of Japan*, vol. 79, no. 2, p. 024706, 2010.
- [108] R. Loudon, "One-dimensional hydrogen atom," *Am. J. Phys.*, vol. 27, pp. 649–655, Dec. 1959.
- [109] C. Manzoni, A. Gambetta, E. Menna, M. Meneghetti, G. Lanzani, and G. Cerullo, "Intersubband exciton relaxation dynamics in single-walled carbon nanotubes," *Phys. Rev. Lett.*, vol. 94, pp. 207401–, May 2005.
- [110] T. Ando, "Effects of valley mixing and exchange on excitons in carbon nanotubes with aharonov - bohm flux," *Journal of the Physical Society of Japan*, vol. 75, p. 024707, 2006.
- [111] A. Srivastava and J. Kono, "Diffusion-limited exciton-exciton annihilation in single-walled carbon nanotubes: A time-dependent analysis," *Phys. Rev. B*, vol. 79, pp. 205407–, May 2009.
- [112] K. Nagatsu, S. Chiashi, S. Konabe, and Y. Homma, "Brightening of triplet dark excitons by atomic hydrogen adsorption in single-walled carbon nanotubes observed by photoluminescence spectroscopy," *Phys. Rev. Lett.*, vol. 105, pp. 157403–, Oct. 2010.
- [113] B. Kitiyanan, W. Alvarez, J. Harwell, and D. Resasco, "Controlled production of single-wall carbon nanotubes by catalytic decomposition of co on bimetallic co-mo catalysts," *Chemical Physics Letters*, vol. 317, pp. 497–503, Feb. 2000.

## Bibliography

- [114] S. M. Bachilo, L. Balzano, J. E. Herrera, F. Pompeo, D. E. Resasco, and R. B. Weisman, "Narrow (n,m)-distribution of single-walled carbon nanotubes grown using a solid supported catalyst," *Journal of the American Chemical Society*, vol. 125, pp. 11186–11187, Sept. 2003.
- [115] A. Högele, S. Seidl, M. Kroner, K. Karrai, C. Schulhauser, O. Sqalli, J. Scrimgeour, and R. J. Warburton, "Fiber-based confocal microscope for cryogenic spectroscopy," *Rev. Sci. Instrum.*, vol. 79, pp. 023709–7, Feb. 2008.
- [116] A. Högele, *Laser spectroscopy of single charge-tunable quantum dots*. PhD thesis, Ludwig-Maximilians-Universität München, 2005.
- [117] W. Schinner, "Spektroskopie von Kohlenstoffnanoröhren im elektrostatischen Feld," Master's thesis, Fakultät für Physik an der Ludwig-Maximilians-Universität München, 2011.
- [118] E. A. Donley, T. P. Heavner, F. Levi, M. O. Tataw, and S. R. Jefferts, "Double-pass acousto-optic modulator system," *Rev. Sci. Instrum.*, vol. 76, pp. 063112–6, June 2005.
- [119] *Datasheet for BPW 34 Silizium-PIN-Fotodiode*.
- [120] C. Meyer, O. Sqalli, H. Lorenz, and K. Karrai, "Slip-stick step-scanner for scanning probe microscopy," *Review of Scientific Instruments*, vol. 76, no. 6, p. 063706, 2005.
- [121] K. Yoshikawa, R. Matsunaga, K. Matsuda, and Y. Kanemitsu, "Mechanism of exciton dephasing in a single carbon nanotube studied by photoluminescence spectroscopy," *Applied Physics Letters*, vol. 94, no. 9, p. 093109, 2009.
- [122] A. Hagen, M. Steiner, M. B. Raschke, C. Lienau, T. Hertel, H. Qian, A. J. Meixner, and A. Hartschuh, "Exponential decay lifetimes of excitons in individual single-walled carbon nanotubes," *Phys. Rev. Lett.*, vol. 95, pp. 197401–4, Nov. 2005.
- [123] H. Jin, D. A. Heller, J.-H. Kim, and M. S. Strano, "Stochastic analysis of stepwise fluorescence quenching reactions on single-walled carbon nanotubes: Single molecule sensors," *Nano Lett.*, vol. 8, pp. 4299–4304, Nov. 2008.
- [124] A. J. Siitonen, D. A. Tsyboulski, S. M. Bachilo, and R. B. Weisman, "Surfactant-dependent exciton mobility in single-walled carbon nanotubes

- studied by single-molecule reactions,” *Nano Lett.*, vol. 10, pp. 1595–1599, Apr. 2010.
- [125] C. Georgi, A. A. Green, M. C. Hersam, and A. Hartschuh, “Probing exciton localization in single-walled carbon nanotubes using high-resolution near-field microscopy,” *ACS Nano*, vol. 4, pp. 5914–5920, Oct. 2010.
- [126] H. Hirori, K. Matsuda, Y. Miyauchi, S. Maruyama, and Y. Kanemitsu, “Exciton localization of single-walled carbon nanotubes revealed by femtosecond excitation correlation spectroscopy,” *Phys. Rev. Lett.*, vol. 97, pp. 257401–, Dec. 2006.
- [127] M. S. Hofmann, J. T. Gluckert, J. Noe, C. Bourjau, R. Dehmel, and A. Högele, “Bright, long-lived and coherent excitons in carbon nanotube quantum dots,” *Nat Nano*, vol. 8, pp. 502–505, July 2013.
- [128] D. Karaiskaj and A. Mascarenhas, “Role of electron-phonon interactions and external strain on the electronic properties of semiconducting carbon nanotubes,” *Phys. Rev. B*, vol. 75, pp. 115426–, Mar. 2007.
- [129] J. H. Choi and M. S. Strano, “Solvatochromism in single-walled carbon nanotubes,” *Applied Physics Letters*, vol. 90, no. 22, pp. –, 2007.
- [130] J. Gao, W. Gomulya, and M. Loi, “Effect of medium dielectric constant on the physical properties of single-walled carbon nanotubes,” *Chemical Physics*, vol. 413, pp. 35–38, Feb. 2013.
- [131] L. Yang, M. P. Anantram, J. Han, and J. P. Lu, “Band-gap change of carbon nanotubes: Effect of small uniaxial and torsional strain,” *Phys. Rev. B*, vol. 60, pp. 13874–13878, Nov. 1999.
- [132] K. Arnold, S. Lebedkin, O. Kiowski, F. Hennrich, and M. M. Kappes, “Matrix-imposed stress-induced shifts in the photoluminescence of single-walled carbon nanotubes at low temperatures,” *Nano Letters*, vol. 4, pp. 2349–2354, Dec. 2004.
- [133] O. Kiowski, S. Lebedkin, F. Hennrich, and M. M. Kappes, “Single-walled carbon nanotubes show stable emission and simple photoluminescence spectra with weak excitation sidebands at cryogenic temperatures,” *Phys. Rev. B*, vol. 76, pp. 075422–, Aug. 2007.

## Bibliography

- [134] K. Matsuda, T. Inoue, Y. Murakami, S. Maruyama, and Y. Kanemitsu, "Exciton fine structure in a single carbon nanotube revealed through spectral diffusion," *Phys. Rev. B*, vol. 77, pp. 193405–, May 2008.
- [135] J. A. Fagan, J. R. Simpson, B. J. Landi, L. J. Richter, I. Mandelbaum, V. Bajpai, D. L. Ho, R. Raffaele, A. R. H. Walker, B. J. Bauer, and E. K. Hobbie, "Dielectric response of aligned semiconducting single-wall nanotubes," *Phys. Rev. Lett.*, vol. 98, p. 147402, Apr 2007.
- [136] A. M. White, E. W. Williams, P. Porteous, and C. Hilsum, "Applications of photoluminescence excitation spectroscopy to the study of indium gallium phosphide alloys," *Journal of Physics D: Applied Physics*, vol. 3, no. 9, p. 1322, 1970.
- [137] J. Urayama, T. B. Norris, J. Singh, and P. Bhattacharya, "Observation of phonon bottleneck in quantum dot electronic relaxation," *Phys. Rev. Lett.*, vol. 86, pp. 4930–4933, May 2001.
- [138] S. M. Sze, *Physics of Semiconductor Devices*. John Wiley & Sons, 2nd ed., 1981.
- [139] P. D. Lomer, "The dielectric strength of aluminium oxide films," *Proceedings of the Physical Society. Section B*, vol. 63, no. 10, p. 818, 1950.
- [140] C. K. Williams, R. W. Hamaker, S. G. Ganesan, R. T. Kuehn, K. R. Swartzel, and J. O'Sullivan, "Low temperature diffusion of alkali earth cations in thin, vitreous sio2 films," *Journal of The Electrochemical Society*, vol. 142, no. 1, pp. 303–311, 1995.
- [141] D. Ginley, H. Hosono, and D. Paine, *Handbook of Transparent Conductors*. Springer, 2011.
- [142] G. Eda, Y.-Y. Lin, S. Miller, C.-W. Chen, W.-F. Su, and M. Chhowalla, "Transparent and conducting electrodes for organic electronics from reduced graphene oxide," *Appl. Phys. Lett.*, vol. 92, pp. 233305–3, June 2008.
- [143] I. Ohlídal, E. Schmidt, M. Líbezný, V. Tvarozek, and I. Novotný, "Ellipsometric analysis of thin nict films," *Thin Solid Films*, vol. 169, pp. 213–222, Feb. 1989.
- [144] A. Beer, "Bestimmung der Absorption des rothen Lichts in farbigen Flüssigkeiten," *Annalen der Physik und Chemie*, vol. 86, pp. 78–88, 1852.

- [145] W. Schottky, "Halbleitertheorie der Sperrschicht," vol. 26, no. 52, pp. 843–843–, 1938.
- [146] A. Grove, B. Deal, E. Snow, and C. Sah, "Investigation of thermally oxidised silicon surfaces using metal-oxide-semiconductor structures," *Solid-State Electronics*, vol. 8, pp. 145–163, Feb. 1965.
- [147] R. H. Kingston and S. F. Neustadter, "Calculation of the space charge, electric field, and free carrier concentration at the surface of a semiconductor," *Journal of Applied Physics*, vol. 26, no. 6, pp. 718–720, 1955.
- [148] A. Goetzberger. and J. C. Irvin, "Low-temperature hysteresis effects in metal-oxide-silicon capacitors caused by surface-state trapping," *IEEE Transactions on Electron Devices*, vol. ED15, no. 12, pp. 1009–1014, 1968.
- [149] Z. R. Abrams and Y. Hanein, "Tube-tube and tube-surface interactions in straight suspended carbon nanotube structures," *J. Phys. Chem. B*, vol. 110, pp. 21419–21423, Sept. 2006.
- [150] M. J. Fernee, B. Littleton, T. Plakhotnik, H. Rubinsztein-Dunlop, D. E. Gomez, and P. Mulvaney, "Charge hopping revealed by jitter correlations in the photoluminescence spectra of single CdSe nanocrystals," *Phys. Rev. B*, vol. 81, pp. 155307–, Apr. 2010.
- [151] F. Cichos, C. von Borczyskowski, and M. Orrit, "Power-law intermittency of single emitters," *Current Opinion in Colloid & Interface Science*, vol. 12, pp. 272–284, Dec. 2007.
- [152] M. Kuno, D. P. Fromm, H. F. Hamann, A. Gallagher, and D. J. Nesbitt, "Non-exponential "blinking" kinetics of single CdSe quantum dots: A universal power law behavior," *The Journal of Chemical Physics*, vol. 112, no. 7, pp. 3117–3120, 2000.
- [153] A. Issac, C. von Borczyskowski, and F. Cichos, "Correlation between photoluminescence intermittency of CdSe quantum dots and self-trapped states in dielectric media," *Phys. Rev. B*, vol. 71, pp. 161302–, Apr. 2005.
- [154] Y. Tomio and H. Suzuura, "Impurity-induced valley mixing of excitons in semiconducting carbon nanotubes," *Physica E: Low-dimensional Systems and Nanostructures*, vol. 42, pp. 783–786, Feb. 2010.

## Bibliography

- [155] C. Georgi, N. Hartmann, T. Gokus, A. A. Green, M. C. Hersam, and A. Hartschuh, "Photoinduced luminescence blinking and bleaching in individual single-walled carbon nanotubes," *ChemPhysChem*, vol. 9, pp. 1460–1464, July 2008.
- [156] K. R. Moonosawmy and P. Kruse, "To dope or not to dope: The effect of sonicating single-wall carbon nanotubes in common laboratory solvents on their electronic structure," *J. Am. Chem. Soc.*, vol. 130, pp. 13417–13424, Sept. 2008.
- [157] L. X. Benedict, S. G. Louie, and M. L. Cohen, "Static polarizabilities of single-wall carbon nanotubes," *Phys. Rev. B*, vol. 52, pp. 8541–8549, Sep 1995.
- [158] D. S. Novikov and L. S. Levitov, "Energy anomaly and polarizability of carbon nanotubes," *Phys. Rev. Lett.*, vol. 96, p. 036402, Jan 2006.
- [159] Y. Li, S. V. Rotkin, and U. Ravaioli, "Electronic response and bandstructure modulation of carbon nanotubes in a transverse electrical field," *Nano Letters*, vol. 3, no. 2, pp. 183–187, 2003.
- [160] G. Y. Guo, K. C. Chu, D.-s. Wang, and C.-g. Duan, "Linear and nonlinear optical properties of carbon nanotubes from first-principles calculations," *Phys. Rev. B*, vol. 69, p. 205416, May 2004.
- [161] E. N. Brothers, K. N. Kudin, G. E. Scuseria, and C. W. Bauschlicher, "Transverse polarizabilities of carbon nanotubes: A hartree-fock and density functional study," *Phys. Rev. B*, vol. 72, p. 033402, Jul 2005.
- [162] B. Kozinsky and N. Marzari, "Static dielectric properties of carbon nanotubes from first principles," *Phys. Rev. Lett.*, vol. 96, p. 166801, Apr 2006.
- [163] S. Yasukochi, T. Murai, S. Moritsubo, T. Shimada, S. Chiashi, S. Maruyama, and Y. K. Kato, "Gate-induced blueshift and quenching of photoluminescence in suspended single-walled carbon nanotubes," *Phys. Rev. B*, vol. 84, p. 121409, Sep 2011.
- [164] L.-G. Tien, C.-H. Tsai, F.-Y. Li, and M.-H. Lee, "Band-gap modification of defective carbon nanotubes under a transverse electric field," *Phys. Rev. B*, vol. 72, pp. 245417–, Dec. 2005.
- [165] L. Yu-Pin, T. Li-Gan, T. Chuen-Horng, L. Ming-Hsien, and L. Feng-Yin, "Effect of vacancy defect on electrical properties of chiral single-walled carbon

- nanotube under external electrical field,” *Chin. Phys. B*, vol. 20, p. 017302, 2011.
- [166] C.-W. Chen, M.-H. Lee, and S. J. Clark, “Band gap modification of single-walled carbon nanotube and boron nitride nanotube under a transverse electric field,” *Nanotechnology*, vol. 15, no. 12, p. 1837, 2004.
- [167] K. Watanabe and K. Asano, “Trions in semiconducting single-walled carbon nanotubes,” *Phys. Rev. B*, vol. 85, pp. 035416–, Jan. 2012.
- [168] C. Cohen-Tannoudji, B. Diu, and F. Laloe, *Quantum mechanics*. Wiley, 1977.
- [169] A. Jorio, M. A. Pimenta, A. G. S. Filho, R. Saito, G. Dresselhaus, and M. S. Dresselhaus, “Characterizing carbon nanotube samples with resonance raman scattering,” *New Journal of Physics*, vol. 5, no. 1, p. 139, 2003.
- [170] M. Dresselhaus, G. Dresselhaus, A. Jorio, A. Souza Filho, and R. Saito, “Raman spectroscopy on isolated single wall carbon nanotubes,” *Carbon*, vol. 40, no. 12, pp. 2043–2061, 2002.
- [171] A. Jorio, R. Saito, J. H. Hafner, C. M. Lieber, M. Hunter, T. McClure, G. Dresselhaus, and M. S. Dresselhaus, “Structural ( n, m) determination of isolated single-wall carbon nanotubes by resonant raman scattering,” *Phys. Rev. Lett.*, vol. 86, pp. 1118–1121, Feb. 2001.
- [172] M. Dresselhaus, G. Dresselhaus, R. Saito, and A. Jorio, “Raman spectroscopy of carbon nanotubes,” *Physics Reports*, vol. 409, pp. 47–99, Mar. 2005.
- [173] Y. Kawashima and G. Katagiri, “Observation of the out-of-plane mode in the raman scattering from the graphite edge plane,” *Phys. Rev. B*, vol. 59, pp. 62–64, Jan. 1999.
- [174] V. Griadun, *Doped Carbon Nanotube Properties*. Carbon Nanotubes, 2010.
- [175] A. S. Grady, S. G. Puntambekar, and D. K. Russell, “Vibrational spectra of dimethyl aluminium hydride,” *Spectrochimica Acta Part A: Molecular Spectroscopy*, vol. 47, no. 1, pp. 47–56, 1991.
- [176] D. Gammon, E. S. Snow, B. V. Shanabrook, D. S. Katzer, and D. Park, “Fine structure splitting in the optical spectra of single gas quantum dots,” *Phys. Rev. Lett.*, vol. 76, pp. 3005–3008, Apr. 1996.

## Bibliography

- [177] R. Heitz and M. G. et al., “Multiphonon-relaxation processes in self-organized inas/gaas quantum dots,” *Applied Physics Letters*, vol. 68, no. 3, pp. 361–363, 1996.
- [178] M. S. Dresselhaus, A. Jorio, M. Hofmann, G. Dresselhaus, and R. Saito, “Perspectives on carbon nanotubes and graphene raman spectroscopy,” *Nano Lett.*, vol. 10, pp. 751–758, Jan. 2010.
- [179] I. Wilson-Rae, C. Galland, W. Zwerger, and A. Imamoglu, “Exciton-assisted optomechanics with suspended carbon nanotubes,” *New Journal of Physics*, vol. 14, no. 11, p. 115003, 2012.
- [180] H. Kalt and M. Hetterich, eds., *Optics of semiconductor and their nanostructures*. Springer, 2004.
- [181] B. F. Habenicht, H. Kamisaka, K. Yamashita, and O. V. Prezhdo, “Ab initio study of vibrational dephasing of electronic excitations in semiconducting carbon nanotubes,” *Nano Lett.*, vol. 7, pp. 3260–3265, Oct. 2007.
- [182] A. Demming, “Carbon nanotubes: A quantum light source,” *Nat Photon*, vol. 2, pp. 459–460, Aug. 2008.
- [183] U. Hohenester and G. Goldoni, “A new quasiparticle in carbon nanotubes,” *Physics*, vol. 4, p. 5, Jan 2011.
- [184] J. J. Crochet, J. G. Duque, J. H. Werner, B. Lounis, L. Cognet, and S. K. Doorn, “Disorder limited exciton transport in colloidal single-wall carbon nanotubes,” *Nano Lett.*, vol. 12, pp. 5091–5096, Sept. 2012.
- [185] G. Davies and M. F. Hamer, “Optical studies of the 1.945 ev vibronic band in diamond,” *Proceedings of the Royal Society of London. A. Mathematical and Physical Sciences*, vol. 348, no. 1653, pp. 285–298, 1976.
- [186] R. Loudon, *The quantum theory of light*. Oxford Scientific Publications, 2000.
- [187] M. Fox, *Quantum Optics: An Introduction*. Oxford University Press, 2006.
- [188] R. J. Glauber, “The quantum theory of optical coherence,” *Phys. Rev.*, vol. 130, pp. 2529–2539, June 1963.
- [189] K. Huang, *Statistical Mechanics*. John Wiley & Sons, 1987.

- [190] P. Frantsuzov, M. Kuno, B. Janko, and R. A. Marcus, “Universal emission intermittency in quantum dots, nanorods and nanowires,” *Nat Phys*, vol. 4, pp. 519–522, July 2008.
- [191] R. Hanbury-Brown and R. Q. Twiss, “A test of a new type of stellar interferometer on sirius,” *Nature*, vol. 178, pp. 1046–1048, Nov. 1956.
- [192] H. J. Kimble, M. Dagenais, and L. Mandel, “Photon antibunching in resonance fluorescence,” *Phys. Rev. Lett.*, vol. 39, pp. 691–695, Sept. 1977.
- [193] C. M. Santori, *Generation of nonclassical light using semiconductor quantum dots*. PhD thesis, Department of applied physics of Stanford University, 2003.
- [194] S. Cova, M. Ghioni, A. Lacaita, C. Samori, and F. Zappa, “Avalanche photodiodes and quenching circuits for single-photon detection,” *Appl. Opt.*, vol. 35, pp. 1956–1976, Apr. 1996.
- [195] C. Kurtsiefer, P. Zarda, S. Mayer, and H. Weinfurter, “The breakdown flash of silicon avalanche photodiodes-back door for eavesdropper attacks?,” *Journal of Modern Optics*, vol. 48, no. 13, pp. 2039–2047, 2001.
- [196] T. Huang, J. Shao, X. Wang, L. Xiao, and S. Jia, “Photon emission characteristics of avalanche photodiodes,” *Optical Engineering*, vol. 44, pp. 074001–074001, July 2005.
- [197] H. Htoon, M. J. O’Connell, P. J. Cox, S. K. Doorn, and V. I. Klimov, “Low temperature emission spectra of individual single-walled carbon nanotubes: Multiplicity of subspecies within single-species nanotube ensembles,” *Phys. Rev. Lett.*, vol. 93, pp. 027401–, July 2004.
- [198] T. Gokus, L. Cognet, J. G. Duque, M. Pasquali, A. Hartschuh, and B. Lounis, “Mono- and biexponential luminescence decays of individual single-walled carbon nanotubes,” *J. Phys. Chem. C*, vol. 114, pp. 14025–14028, July 2010.
- [199] C. Galland, Y. Ghosh, A. Steinbruck, M. Sykora, J. A. Hollingsworth, V. I. Klimov, and H. Htoon, “Two types of luminescence blinking revealed by spectroelectrochemistry of single quantum dots,” *Nature*, vol. 479, pp. 203–207, Nov. 2011.
- [200] Y.-Z. Ma, J. Stenger, J. Zimmermann, S. M. Bachilo, R. E. Smalley, R. B. Weisman, and G. R. Fleming, “Ultrafast carrier dynamics in single-walled car-

## Bibliography

- bon nanotubes probed by femtosecond spectroscopy,” *The Journal of Chemical Physics*, vol. 120, no. 7, pp. 3368–3373, 2004.
- [201] Y. Murakami and J. Kono, “Nonlinear photoluminescence excitation spectroscopy of carbon nanotubes: Exploring the upper density limit of one-dimensional excitons,” *Phys. Rev. Lett.*, vol. 102, pp. 037401–, Jan. 2009.
- [202] L. Colombier, J. Selles, E. Rousseau, J. S. Lauret, F. Vialla, C. Voisin, and G. Cassabois, “Detection of a biexciton in semiconducting carbon nanotubes using nonlinear optical spectroscopy,” *Phys. Rev. Lett.*, vol. 109, pp. 197402–, Nov. 2012.
- [203] K. Matsuda, T. Inoue, Y. Murakami, S. Maruyama, and Y. Kanemitsu, “Exciton dephasing and multiexciton recombinations in a single carbon nanotube,” *Phys. Rev. B*, vol. 77, pp. 033406–, Jan. 2008.
- [204] H. Qian, P. T. Araujo, C. Georgi, T. Gokus, N. Hartmann, A. A. Green, A. Jorio, M. C. Hersam, L. Novotny, and A. Hartschuh, “Visualizing the local optical response of semiconducting carbon nanotubes to dna-wrapping,” *Nano Lett.*, vol. 8, pp. 2706–2711, Aug. 2008.
- [205] J. Waissman, M. Honig, S. Pecker, A. Benyamini, A. Hamo, and S. Ilani, “Realization of pristine and locally tunable one-dimensional electron systems in carbon nanotubes,” *Nat Nano*, vol. 8, pp. 569–574, Aug. 2013.
- [206] K. K. Gomes, W. Mar, W. Ko, F. Guinea, and H. C. Manoharan, “Designer dirac fermions and topological phases in molecular graphene,” *Nature*, vol. 483, pp. 306–310, Mar. 2012.
- [207] E. Gaufrès, N. IZard, X. Le Roux, D. Marris-Morini, S. Kazaoui, E. Cassan, and L. Vivien, “Optical gain in carbon nanotubes,” *Applied Physics Letters*, vol. 96, no. 23, pp. –, 2010.
- [208] M. D. Eisaman, J. Fan, A. Migdall, and S. V. Polyakov, “Invited review article: Single-photon sources and detectors,” *Review of Scientific Instruments*, vol. 82, no. 7, p. 071101, 2011.
- [209] P. Ajayan and O. Zhou, “Applications of carbon nanotubes,” in *Topics in Applied Physics* (M. Dresselhaus, G. Dresselhaus, and P. Avouris, eds.), vol. 80, pp. 391–425–, Springer Berlin Heidelberg, 2001.

- [210] T. Hertel, R. Martel, and P. Avouris, “Manipulation of individual carbon nanotubes and their interaction with surfaces,” *J. Phys. Chem. B*, vol. 102, pp. 910–915, Feb. 1998.
- [211] C. C. Wu, C. H. Liu, and Z. Zhong, “One-step direct transfer of pristine single-walled carbon nanotubes for functional nanoelectronics,” *Nano Lett.*, vol. 10, pp. 1032–1036, Jan. 2010.
- [212] D. Legrand, C. Roquelet, G. Lanty, P. Roussignol, X. Lafosse, S. Bouchoule, E. Deleporte, C. Voisin, and J. S. Lauret, “Monolithic microcavity with carbon nanotubes as active material,” *Applied Physics Letters*, vol. 102, no. 15, pp. –, 2013.
- [213] J. P. Reithmaier, G. Sek, A. Loffler, C. Hofmann, S. Kuhn, S. Reitzenstein, L. V. Keldysh, V. D. Kulakovskii, T. L. Reinecke, and A. Forchel, “Strong coupling in a single quantum dot-semiconductor microcavity system,” *Nature*, vol. 432, pp. 197–200, Nov. 2004.
- [214] A. Badolato, K. Hennessy, M. Atature, M. re, J. Dreiser, E. Hu, P. M. Petroff, and A. Imamoglu, A.lu, “Deterministic coupling of single quantum dots to single nanocavity modes,” *Science*, vol. 308, no. 5725, pp. 1158–1161, 2005.
- [215] I. Favero and K. Karrai, “Cavity cooling of a nanomechanical resonator by light scattering,” *New Journal of Physics*, vol. 10, no. 9, p. 095006, 2008.
- [216] A. Friedenauer, H. Schmitz, J. T. Glueckert, D. Porras, and T. Schaetz, “Simulating a quantum magnet with trapped ions,” *Nat Phys*, vol. 4, pp. 757–761, Oct. 2008.
- [217] H. Schmitz, R. Matjeschk, C. Schneider, J. Glueckert, M. Enderlein, T. Huber, and T. Schaetz, “Quantum walk of a trapped ion in phase space,” *Phys. Rev. Lett.*, vol. 103, pp. 090504–, Aug. 2009.
- [218] A. V. Naumov, S. M. Bachilo, D. A. Tsybouski, and R. B. Weisman, “Electric field quenching of carbon nanotube photoluminescence,” *Nano Letters*, vol. 8, pp. 1527–1531, May 2008.



# List of publications

## Spectroscopy of carbon nanotubes

- J. Glückert, M. Hofmann, W. Schinner, and Alexander Högele, "Photoluminescence of Localized Carbon Nanotube Excitons in Transverse Electric Field", *in preparation*
- M. Hofmann<sup>‡</sup>, J. Glückert<sup>‡</sup>, J. Noe, C. Bourjau, R. Dehmel, and A. Högele, "Bright, long-lived and coherent excitons in carbon nanotube quantum dots", *nature Nanotechnology*, vol. 8, pp. 502-505, May 2013

## Quantum simulation in an ion trap

- R. Matjeschk, C. Schneider, M. Enderlein, T. Huber, H. Schmitz, J. Glueckert, and T. Schätz, "Experimental simulation and limitations of quantum walks with trapped ions", *New Journal of Physics*, vol. 14, p. 035012-, Mar 2012
- H. Schmitz, R. Matjeschk, C. Schneider, J. Glueckert, M. Enderlein, T. Huber, and T. Schätz, "Quantum Walk of a Trapped Ion in Phase Space", *Physical Review Letters*, vol. 103, p. 090504-, Aug 2009
- H. Schmitz, A. Friedenauer, C. Schneider, R. Matjeschk, M. Enderlein, T. Huber, J. Glueckert, D. Porras, and T. Schätz, "The arch of simulating quantum spin systems with trapped ions", *Applied Physics B-Lasers and Optics*, vol. 95, pp. 195-203, May 2009
- A. Friedenauer, H. Schmitz, J. Glueckert, D. Porras, and T. Schätz, "Simulating a quantum magnet with trapped ions", *Nature Physics*, vol. 4, pp. 757-761, Oct 2008

---

<sup>‡</sup>These authors contributed equally to this work.



# Danksagung

Zum Abschluss möchte ich all denjenigen danken, die durch ihre großartige Unterstützung die letzten Jahre maßgeblichen Anteil an Entstehen und Gelingen dieser Dissertation hatten. Für mich persönlich ist es gerade die Erfahrung mit diesen Menschen, die diese Arbeit zu einem Erfolg macht.

Zu allererst danke ich meinem Doktorvater Alexander Högele für die Möglichkeit mit ihm die Geheimnisse der Nanoröhren zu erkunden. Vielen Dank für die gute Betreuung, für deine stets offene Tür, die gewährten Freiheiten und deinen konsequenten fachlichen Beistand. Deine herzliche Art Menschen zu führen, dein grenzenloser Optimismus und deine Gelassenheit werden mir immer ein Vorbild bleiben.

Jörg Kotthaus danke ich für den besonderen Geist und die einzigartigen Infrastruktur an seinem Lehrstuhl, die Teilhabe an seinem Erfahrungsschatz und seiner ganz praktischen Hilfe bei den ohmschen Kontakten.

Ich bedanke mich bei Matthias Hofmann für die jahrelange freundschaftliche Zusammenarbeit an der Grasnarbe der Kohlenstoffnanoröhren - Erwin, Itto und wie sie alle hießen. Es hat mir große Freude bereitet mit dir immer so konstruktiv zu arbeiten. Für ihr großes Engagement am Experiment danke ich Wolfgang Schinner, Alexander Kneer und Matthias Hauck. Euer Erfolg war mir immer eine besondere Motivation.

Für die technische und organisatorische Unterstützung am Lehrstuhl bedanke ich mich Martina Jüttner, Bert Lorenz, Reinhold Rath und Anton Heindl. Besonders herauszustellen sind zudem Philipp Altpeter und Stephan Manus für ihre Hilfe im Reinraum und bei der Elektronik.

Georg Schinner danke ich für unsere langjährige Freundschaft, seine stete Hilfsbereitschaft und die wichtigen Ratschläge. Für ihre Unterstützung bei Mathematica und an der Jura gilt mein besonderer Dank Johannes Rieger, Sebastian Stapfner, Thomas Faust, Jens Repp und Quirin Unterreithmeier. Florian Seilmeier, Andre Neumann, Felix Mendoza, Darren Southworth, Matthias Fiebig und Onur Basarir danke ich für das freundschaftliche Arbeitsklima im N303.

Lina, dir danke ich für deine Liebe, deinen Glauben an den Erfolg, deine liebenswerte Fürsorge und für alles, was wir die letzten Jahre erleben durften und bald zu dritt erleben werden. Es bedeutet mir alles.

## *Bibliography*

Meiner Eltern Uschi und Udo, sowie meinen Brüdern Jens und Ulf danke ich für ihren beständigen Rückhalt, ihren Humor und die Grundsteine, die sie mir für meinen Weg mitgegeben haben.

Ich danke Hanna für die raren, aber langen Abende und die klugen Ratschläge für die Welt außerhalb der Physik.

Hannes Lüling und der gesamten Fußballcrew danke ich für eine Gehirnerschütterung, einen gebrochenen Zehen, die Überdehnung diverser Bänder, unzählige blaue Flecken und vor allem unvergesslich schöne Fußballmatches irgendwo zwischen gefühlter Welt- und tatsächlicher Kreisklasse.

Zuletzt gilt mein Dank an meine Kommilitonen, Freunden und Mitbewohnern für die zu seltene Ablenkung, danke Anton, Michi, Louis, Brendan, Florian, Justin, Regina, Max, Tobias und Vroni, Alex, Keppe, Arthur, Christian, Jörg und Resi, Hannes und Matthias, Robert, Lorenz, Julian und Jürgen.

# Notes

